Technical Physics Letters, Vol. 28, No. 7, 2002, pp. 533–535. Translated from Pis'ma v Zhurnal Tekhnicheskoĭ Fiziki, Vol. 28, No. 13, 2002, pp. 1–6.

Distribution of Corrosion Pits on a Metal Surface

V. I. Vettegren, A. Ya. Bashkarev, and G. I. Morozov

Ioffe Physicotechnical Institute, Russian Academy of Sciences, St. Petersburg, 194021 Russia

e-mail: Victor.Vettegren@pop.ioffe.rssi.ru

Received January 22, 2002

Abstract—The distribution of corrosion pits on the surface of stainless steel samples treated in a 3% NaCl solution is studied. It is established that the distributions are thermodynamically optimized and can be described by the Gibbs expression for a canonical distribution of the thermodynamic probability of energy fluctuations. A wide occurrence of the pitting corrosion and the broad scatter of pits with respect to size are explained. © *2002 MAIK "Nauka/Interperiodica".*

Local corrosion (pitting) of metals, whereby the metal degradation rate in certain areas is much higher than that on the surrounding surface, is one of the most widely spread types of corrosive damage [1–3]. It is commonly believed that the pitting corrosion is related to the existence of special local sites in the surface layer of a metal, in which the material is more reactive than that in the surrounding and, hence, is predominantly subject to degradation. The dimensions of local corrosion spots (pits) can vary over two orders in magnitude. However, the primary reasons for a wide occurrence of the pitting corrosion and the broad scatter of pit dimensions still remain unknown.

Below we demonstrate that the pit size distribution on a stainless steel surface can be described by the Gibbs expression for energy fluctuations. We also suggest an explanation for the wide occurrence of the pitting corrosion and the broad variation of the pit size proceeding from the principle of the configurational entropy tending to maximum.

The plates of various doped low-carbon steels (carbon, 0.12%; nickel, 9%; chromium, 8–18%) were rolled to reduce the thickness from 3 mm to ≈200 μm and cut into 20-mm-wide, 100-mm-long strips. In order to relieve internal stresses, the samples were annealed for 3 h at 450°C in air. Then the samples were exposed for several months in a 3% aqueous NaCl solution at various loads and temperatures. After the corrosion test, the average depth and lateral size of pits on the sample surface were determined with the aid of a Neophot 32 microscope (Carl Zeiss Jena, Germany).

The exposure in the corrosive medium resulted in the appearance of corrosion pits on the steel surface (Fig. 1). The pit shape resembles a cone with rough walls and with the vertex inside the sample. The pit depth varies from 2 to ≈70 μm, while lateral dimensions in the surface plane vary from ≈20 to ≈500 μm.

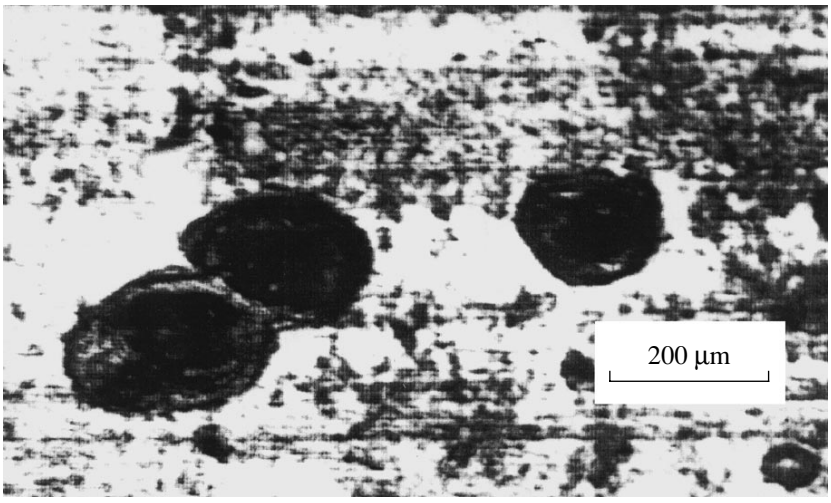

Fig. 1. A microphotograph of corrosion pits on the surface of a low-carbon steel.

1063-7850/02/2807-0533$22.00 © 2002 MAIK "Nauka/Interperiodica"

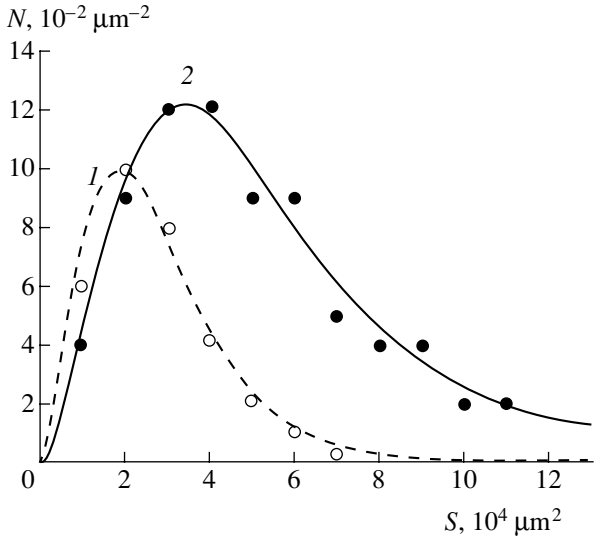

Fig. 2. Corrosion spot size distribution on the surface of a low-carbon steel exposed for 400 h in a corrosive medium (*1*) in the unloaded state and (*2*) under a 13 MPa tensile load. Open and black circles represent the experimental data; dashed and solid curves show the results of approximation using expression (3).

For the quantitative processing of experimental data, the pits were approximated by round cones and characterized by the side surface area S. It was found that the pit size distribution $n(S)$ exhibits a maximum at $S \sim (2\text{–}4) \times 10^4$ μm^2 and is asymmetrically extended toward greater areas (Fig. 2). An increase in the tensile load and the corrosive solution temperature makes the asymmetry more pronounced (Fig. 2).

The experimental pit size distributions were described using an expression proposed by Gibbs [4] for the canonical distribution of the thermodynamic probability of fluctuations in the energy E for a constant volume. In modern notations, this expression can be written as [5]

$$f(E) = \beta\frac{(\beta E)^{m-1}}{\Gamma(m)}\exp(-\beta E), \qquad (1)$$

where m is the number of degrees of freedom, $\beta \equiv 1/k_B T$, and k_B is the Boltzmann constant. The distribution function (1) is thermodynamically optimized, which implies that the configurational entropy of the system is maximum [5]. Taking into account that the energy of defect formation $E = \Delta U_0 S$ is proportional to the side surface area and the defects grow in three directions ($m = 3$), expression (1) can be transformed to

$$n(S) = n_0 S^2 \exp(-\beta S \Delta U_0). \qquad (2)$$

Here, $n(S)$ is the concentration of defects with the side surface area S, ΔU_0 is the defect formation energy per unit surface area, $n_0 \equiv C_a \beta \frac{(\Delta U_0)^2}{2}$, and C_a is the normalization constant. Previously, it was established that this expression describes the experimental size distributions of nanodefects formed on the surface of loaded metal (copper, gold, and molybdenum) foils [6, 7], supermolecular formations on the surface of glassy poly(methyl methacrylate) [8], and species of fungi, yeasts, and bacteria [9]. Based on these results, we conclude that the distributions of these objects with respect to size are thermodynamically optimized, that is, the configurational entropy determining the scatter of object dimensions is maximum.

Thorough investigations [6, 7] showed that more precise description of the experimental distributions of objects with respect to size is provided by the sum of expressions (2):

$$n(S) = \sum_{i=1}^{n} n_{0i} S_i^2 \exp(-\beta S_i \Delta U_{0i}), \qquad (3)$$

where n_{0i} and ΔU_{0i} are the normalization constants and the energies of formation of the ith object. This description implies that the set of nanodefects includes several statistical thermodynamic ensembles possessing various intrinsic energies ΔU_{0i}. An analysis of the distribution of corrosion spots with respect to size showed that these objects can be also described by expression (3) (Fig. 2). Therefore, the corrosion pits also form a set of statistical ensembles.

The equilibrium concentration x_c of pits is determined from the condition that their entropy is maximum and amounts to $x_c \approx e^{-3} = 0.05$, while the ratio of equilibrium concentrations in the neighboring statistical ensembles (in equilibrium) must be ≈1/27 [6]. Experimental values of the total concentration x_c were, as a rule, smaller than 0.05, while their ratios for the neighboring ensembles varied from 0.001 to 25 depending on the metal studied. Despite the absence of numerical equilibrium, the shape of the pit size distribution is adequately described by expression (3) and, hence, is thermodynamically optimized. Thus, even under nonequilibrium conditions, the pitting process is thermodynamically more favorable than the equilibrium corrosion. Probably, this accounts for the fact that this type of corrosion is more frequently encountered. Simultaneously, the tendency of the configurational entropy of the system to maximum accounts for a broad variation of the size of corrosion spots.

It was found that the energies of formation of the corrosion spots and the average pit dimensions in the neighboring ensembles differ by a factor of three. Indeed, for unloaded samples, the energies of formation of the ensembles of corrosion spots coincided for all steels: $\Delta U_{01} \approx 4.3$ kJ/(mol μm^2), $\Delta U_{02} \approx 1.4$ kJ/(mol μm^2), and $\Delta U_{03} \approx 0.05$ kJ/(mol μm^2). The average spot dimen-

sions in these ensembles are $\langle S_1 \rangle \approx 33\ \mu m^2$, $\langle S_2 \rangle \approx 100\ \mu m^2$, and $\langle S_3 \rangle \approx 300\ \mu m^2$, respectively. As can be seen, the energy of formation and the average corrosion spot size in the neighboring ensembles differ by a factor of about three. Previously [6, 7], it was established that the average dimensions and the energies of defect formation in the ensembles of nanodefects on the surface of loaded metal samples also differ by a factor of three.

Under the action of tensile stress, the energy of formation of the corrosion pit tends to decrease. For example, the ΔU_{01} value for a sample loaded to 13 MPa decreased to ≈1.8 kJ/(mol μm^2) (from 4.3 kJ/(mol μm^2) in the unloaded state).

Thus, we have established that the corrosion pits formed on the stainless steel surface form a series of statistical ensembles. The distribution of pits with respect to dimensions is thermodynamically optimized and described by an expression for the canonical distribution of the thermodynamic probability of energy fluctuations.

Acknowledgments. This study was supported by the Ministry of Education of the Russian Federation (project no. E00-4.0-21).

REFERENCES

1. H. H. Ulig and R. W. Revie, *Corrosion and Corrosion Control. An Introduction to Corrosion Science and Engineering* (Wiley, New York, 1985).
2. L. I. Andropov, *Theoretical Electrochemistry* (Vysshaya Shkola, Moscow, 1984).
3. L. Ya. Tsikerman, *Long-Term Forecast for Danger of Ground Corrosion of Metals* (Nedra, Moscow, 1966).
4. J. W. Gibbs, *Elementary Principles in Statistical Mechanics* (Yale Univ. Press, New Haven, 1902).
5. B. L. Lavenda, *Statistical Physics. A Probabilistic Approach* (Wiley, New York, 1991).
6. H. G. Kilian, V. I. Vettegren, and V. N. Svetlov, Fiz. Tverd. Tela (St. Petersburg) **42** (11), 2024 (2000) [Phys. Solid State **42**, 2083 (2000)].
7. H. G. Kilian, V. I. Vettegren, and V. N. Svetlov, Fiz. Tverd. Tela (St. Petersburg) **43** (11), 2107 (2001) [Phys. Solid State **43**, 2199 (2001)].
8. H. G. Kilian, R. Metzler, and B. Zink, J. Chem. Phys. **107** (20), 8697 (1997).
9. H. G. Kilian, V. I. Vettegren, and M. Koepf, Prog. Colloid Polym. Sci. **117**, 172 (2001).

Translated by P. Pozdeev

Technical Physics Letters, Vol. 28, No. 7, 2002, pp. 536–538. Translated from Pis'ma v Zhurnal Tekhnicheskoĭ Fiziki, Vol. 28, No. 13, 2002, pp. 7–14.

The Effect of Asymmetry upon the Fractal Properties of Synchronous Chaos in Coupled Systems with Period Doubling

E. P. Seleznev and A. M. Zakharevich

Saratov Branch, Institute of Radio Engineering and Electronics, Russian Academy of Sciences, Saratov, Russia

e-mail: sbire@sgu.ru

Received January 28, 2002

Abstract—The effect of an asymmetry upon the synchronous chaos in coupled systems with period doubling is studied by numerical methods. The introduction of an asymmetry after the loss of the transverse superstability imparts fractal properties to the synchronous chaotic attractor. On approaching the synchronization boundary (with decreasing coupling), the fractal dimension of the attractor exhibits a nonmonotonic behavior. *© 2002 MAIK "Nauka/Interperiodica".*

Investigation into the chaotic synchronization phenomenon is of significant value for both basic science and applications [1–3]. Of special interest is the study of chaotic synchronization in symmetrically coupled identical subsystems featuring one of the classical scenarios of transition to chaos, for example, via a sequence of period-doubling bifurcations [7–13]. The regime of synchronous chaotic oscillations in such a system corresponds to a situation when the dynamic variables in both subsystems are equal. In this case, there appear two selected directions in the phase space: diagonal (in which the motions are unstable and the corresponding Lyapunov index is positive) and transverse (in which the motions are stable and the corresponding Lyapunov index is negative). The evolution of the system with variation of the nonlinearity parameter is identical to the evolution of an isolated subsystem.

The aim of this study was to determine the effect of an asymmetry (nonidentity of subsystems) on the structure of the synchronous chaotic attractor and on the evolution of this structure on approach to the synchronization boundary. For this purpose, we have numerically studied a system of dissipatively coupled quadratic mappings

$$\begin{cases} x_{n+1} = \lambda - x_n^2 + k(x_n^2 - y_n^2), \\ y_{n+1} = \lambda\delta - y_n^2 - k(x_n^2 - y_n^2), \end{cases} \quad (1)$$

where x_n and y_n are the dynamic variables, $n = 1, 2, \ldots$ is the discrete time, λ is the parameter of nonlinearity, δ is the parameter of asymmetry, and k is the coupling parameter.

For $\delta = 1$, the system is symmetric with respect to the substitution $x_n \longleftrightarrow y_n$. For this case, the system dynamics was studied in sufficient detail [2, 12–15]. For $k > 0$ in the region above the critical level ($\lambda > \lambda_c$, where $\lambda_c = 1.40115518909\ldots$ is the critical value for the isolated subsystems [16]), system (1) exhibits a synchronous chaotic regime with the phase portrait situated on the diagonal of the (x_n, y_n) plane. In this case, behavior of the coupled systems is equivalent to the dynamics of an isolated subsystem. Estimation of the correlation dimension of a chaotic attractor for the critical value of the parameter ($\lambda = \lambda_c$) yields $d_c = 0.54$ (we have calculated a reduced correlation dimension by using 40000 values and 5000 reference points determined to within 10^{-18}), which is close to the Hausdorff dimension of the critical attractor of a quadratic mapping [16, 17]. As the parameter λ grows, the dimension of the synchronous attractor increases and becomes equal to unity. This is related to the fact that the dimension of the chaotic attractor for the quadratic mapping is unity and the synchronous attractor of a coupled system is situated on a straight line—the diagonal $x_n = y_n$ in the phase plane.

When $\delta \neq 1$, the symmetry is broken but the synchronization regime is retained. Figure 1a shows the structure of the plane of parameters (k, λ) for $\delta = 0.97$. Here, nonshaded areas correspond to periodic synchronized cycles, light-gray areas represent synchronous chaotic regimes, dark-gray areas correspond to nonsynchronized regimes, solid lines indicate the period-doubling bifurcations, and figures at the lines indicate the cycle periods. Figure 1b presents the phase portraits of chaotic attractors and shows some fragments in more detail.

Let us consider evolution of the cycle with period 1 when the parameter λ increases at constant values of $k = 0.5$ and $\delta = 0.97$. The growth of λ is accompanied by a sequence of period-doubling bifurcations, which terminates (at $\lambda \approx 1.4229918\ldots$) by the transition to a

1063-7850/02/2807-0536$22.00 © 2002 MAIK "Nauka/Interperiodica"

synchronous chaos (Fig. 1b, fragment 1). For $k = 0.5$, the determinant of the linearization matrix equals zero and, hence, all cycles (both stable and saddle-point) of system (1) are superstable in the transverse direction. In this case, the critical attractor is situated on the straight line and the correlation dimension is estimated at $d_c = 0.5$ (which is close to the correlation dimension of the critical attractor of a one-dimensional quadratic mapping calculated in [16, 17]). As the parameter λ grows further, the connectivity of the synchronous attractor gradually decreases (see Fig. 1b, where fragment 2 shows a simply connected character), while the correlation dimension increases to reach $d_c = 1$. Thus, in the case of an asymmetry introduced in a system with transverse superstability, fractal properties of the synchronous chaos are analogous to those in the symmetric case.

As the coupling parameter decreases, the in-phase stable and saddle-point cycles of system (1) lose superstability in the transverse direction, while the unstable manifolds of their saddle cycles are no longer situated on the same straight line. Figure 1b (fragment 3) illustrates the case of a critical attractor for $k = 0.4$. With increasing λ, each element of the critical attractor evolves in its own direction in the phase space and, as a result, the critical attractor is not situated on a straight line and retains a fractal character (Fig. 1b, fragment 4).

Figure 2a shows dependence of the correlation dimension of synchronous chaos on the coupling parameter for $\lambda = 2$. Figure 2b presents the phase portraits of attractors and shows some fragments in more detail. As the λ value decreases, the dimension grows above unity and the attractor is no longer situated on the diagonal of the phase plane. A greater scale (Fig. 1b, fragment 4) reveals a complex fractal structure representing an infinite system of lines. As the coupling parameter decreases further, the attractor expands in the transverse direction (Fig. 2b, fragment 1) and increases in dimension. The line structure of the synchronous attractor is revealed on a smaller scale. One could reasonably suggest that, on approaching the synchronization boundary, the attractor dimension (as well as the second Lyapunov index) would monotonically grow.

However, when the coupling parameter k approaches 0.25, the synchronous attractor begins to contract in the transverse direction (while the second Lyapunov index keeps growing) and the attractor dimension decreases to become close to unity (although the attractor is still not situated on a straight line) (Fig. 2b, fragment 2). It should be noted that, in the vicinity of the point at $\lambda = 2$ and $k = 0.25$, the system features period-doubling bifurcations of the saddle-point cycles embedded into the synchronous chaotic attractor. Therefore, the contraction may be caused by a change in configuration of the manifolds of unstable cycles. Further decrease in the coupling parameter leads to an increase in the correlation dimension and to the attractor expansion in the transverse direction (Fig. 2b, fragments 3 and 4). On approaching the boundary of the synchronization region, the attractor keeps expanding, while its dimension decreases again.

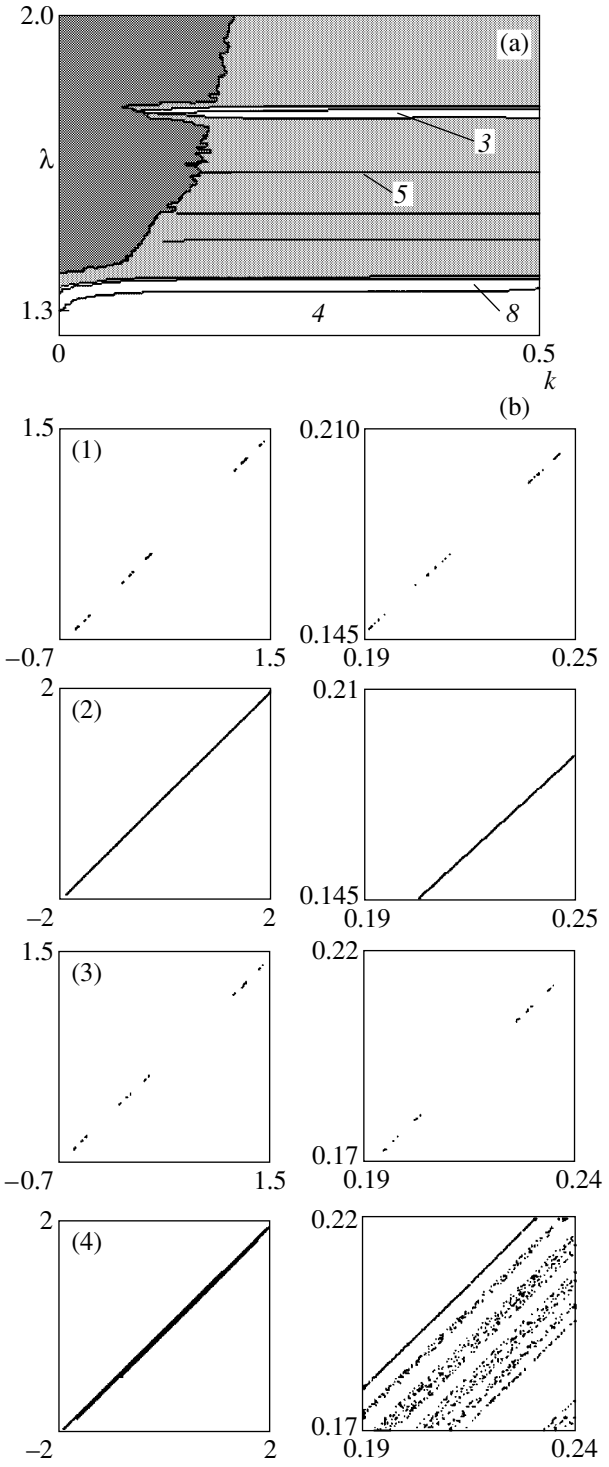

Fig. 1. Diagrams showing (a) the structure of the plane of parameters (k, λ) for $\delta = 0.97$ and (b) the phase portraits and their fragments for (1) $\lambda = 1.4229918\ldots$, $k = 0.5$; (2) $\lambda = 2$, $k = 0.5$; (3) $\lambda = 1.422693\ldots$, $k = 0.4$; and (4) $\lambda = 2$, $k = 0.4$.

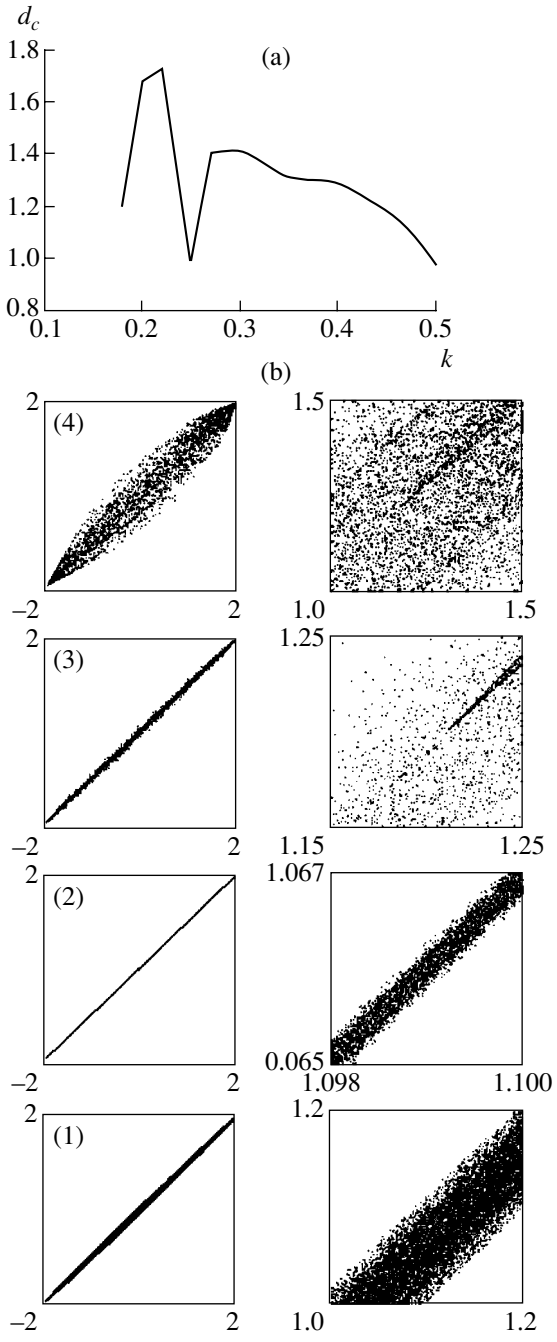

Fig. 2. Diagrams showing (a) the plot of correlation dimension d_c versus parameters k for $\lambda = 2$ and (b) the phase portraits and their fragments for $k = 0.3$ (1), 0.25 (2), 0.24 (3), and 0.225 (4).

Thus, we can draw the following conclusions. The introduction of an asymmetry (nonidentity of subsystems) into symmetrically coupled systems does not influence the dimension of the synchronous chaotic attractor (the attractor dimension characteristics remain the same as those in an isolated subsystem). When the superstability is lost, the attractor dimension begins to increase and exhibits a nonmonotonic behavior on approaching the synchronization boundary.

Acknowledgments. This study was supported by the Russian Foundation for Basic Research (project no. 02-02-17578) and by the US Civilian Research and Development Foundation for Independent States of the Former Soviet Union (CRDF Award No. REC-006).

REFERENCES

1. T. Yamada and H. Fujisaka, Prog. Theor. Phys. **69**, 32 (1983).
2. A. S. Pikovsky, Z. Phys. B **55**, 149 (1984).
3. L. M. Pecora and T. L. Carrol, Phys. Rev. Lett. **64**, 821 (1990).
4. M. Hasler, Philos. Trans. R. Soc. London, Ser. A **353**, 115 (1996).
5. V. S. Afraimovich, V. I. Nekorkin, G. V. Osipov, *et al.*, *Stability, Structures and Chaos in Nonlinear Synchronization Networks* (World Scientific, Singapore, 1994).
6. M. Hasler, in *Proceedings of the International Special Workshop on Nonlinear Dynamics of Electronic Systems, Moscow, 1997*, p. 2.
7. Y. Maistrenko and T. Kapitaniak, Phys. Rev. E **54**, 3285 (1996).
8. K. Pyragas, Phys. Rev. E **54** (5), R4508 (1996).
9. V. Astakhov, A. Shabunin, T. Kapitaniak, *et al.*, Phys. Rev. Lett. **79** (6), 1014 (1997).
10. M. Hasler, Yu. Maistrenko, and O. Popovych, Phys. Rev. E **58** (5), 6843 (1998).
11. D. Postnov, Seung Kee Han, and Hyungtae Kook, Phys. Rev. E **60** (3), 2799 (1999).
12. Yu. L. Maistrenko, V. L. Maistrenko, O. Popovych, *et al.*, Phys. Rev. E **60** (3), 2817 (1999).
13. O. Popovych, Yu. Maistrenko, E. Mosekilde, *et al.*, Phys. Rev. E **63** (3), 036201 (2001).
14. S. P. Kuznetsov, Izv. Vyssh. Uchebn. Zaved., Radiofiz. **28** (8), 991 (1985).
15. V. V. Astakhov, B. P. Bezruchko, E. N. Erastova, *et al.*, Zh. Tekh. Fiz. **60** (10), 19 (1990) [Sov. Phys. Tech. Phys. **35**, 1122 (1990)].
16. T. S. Halsey, M. H. Jensen, L. P. Kadanoff, *et al.*, Phys. Rev. A **33**, 1141 (1986).
17. A. P. Kuznetsov and S. P. Kuznetsov, Izv. Vyssh. Uchebn. Zaved., Prikl. Nelineĭnaya Din. **1** (1–2), 15 (1993).

Translated by P. Pozdeev

Technical Physics Letters, Vol. 28, No. 7, 2002, pp. 539–540. Translated from Pis'ma v Zhurnal Tekhnicheskoĭ Fiziki, Vol. 28, No. 13, 2002, pp. 15–18.

The Optical Elongation of Lightguides in Photopolymerizable Compositions

A. L. Lonin and S. N. Mensov

Nizhni Novgorod State University, Nizhni Novgorod, Russia

e-mail: mensov@rf.unn.runnet.ru

Received November 23, 2001

Abstract—We have studied the possibility of forming a waveguide channel in a transparent weakly absorbing photopolymerizable composition by an optical method based on the self-channeling of a radiation emitted from the edge of an optical fiber. The influence of the directivity pattern of emission from the fiber edge (i.e., of the radiation mode composition) on the channel formation is considered. In the experiment, the length of a multimodal optical fiber with a diameter of 50 μm was increased by up to 1 cm. © *2002 MAIK "Nauka/Interperiodica".*

In creating optical fiber networks, there arises a problem of coupling optical fibers to radiation sources, photodetectors, etc. In order to avoid considerable losses related to violation of the waveguide channel homogeneity at the joint site, it is necessary to ensure precise positional matching of the jointed elements, which requires labor-consuming technologies [1].

An alternative method for creating the coupling elements, eliminating the need in positioning along one (longitudinal) coordinate, is offered by the optical elongation of a fiber in a transparent photopolymerizable composition representing a nonlinear medium with memory. As is known, such compositions exhibit an irreversible light-induced transition from liquid monomer to solid polymer state, which is accompanied by an increase in the refractive index [2]. These media can also feature the phenomenon of waveguide self-formation as a result of the self-channeling of a laser beam [3]. Using this phenomenon induced by radiation at the output of an initial optical fiber, it is possible to elongate the waveguiding channel immediately at the site of jointing to the subsequent elements.

In the experiment, an optical fiber was elongated using the scheme depicted in Fig. 1. The beam of a He–Ne laser *1* (with a wavelength of $\lambda = 0.63$ μm) was focused by lens *3* onto the front edge of an optical fiber *4*, the other end of which was elongated in a cell containing a photopolymerizable composition *5*. The process of a polymer track formation was monitored by a video camera *6*. The track was visualized using IR radiation (not inducing polymerization) from light-emitting diode *7* collimated by lens *8*. The images recorded by camera *6* were processed by a computer *9*. The primary laser beam intensity could be varied by attenuator *2* in the range from 5 to 100 mW/mm^2.

The nonlinear medium *5* represented a photopolymerizable composition based on an OKM-2 compound [2], the refractive index of which is $n_m = 1.46$ in the monomer state and acquires a maximum increment of $\Delta n_{\max} = 5\%$ upon complete polymerization. Variation of the refractive index of the nonlinear medium studied as a function of the exposure can be described by an expression of the type [4]

$$\Delta n(x, z, t) = \Delta n_{\max}\left(1 - \exp\left[-\left(-\frac{H(x, z, t)}{H_0}\right)^{\gamma}\right]\right),$$

where Δn is the current increment of the refractive index, H is the exposure, H_0 is the normalization coefficient determining time scale of the polymerization process, and γ is the parameter of the characteristic contrast.

A special feature of the given composition was the decrease of γ with increasing intensity of the incident radiation [4]. In the range of the laser beam intensity variation (from 10 to 100 mW/mm^2), the value of γ changes from 4 to 1. Another important feature of the system under consideration is that the complex field amplitude distribution at the output of the initial optical fiber has a more complicated structure as compared to that in the Gaussian beam [3] and, hence, exhibits a different character of the diffraction-related divergence. In

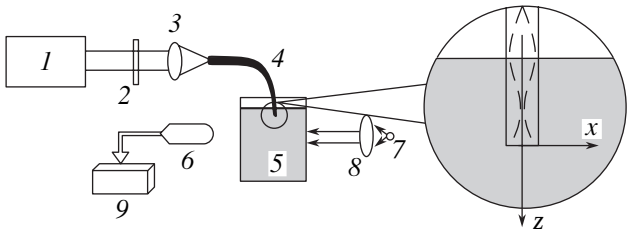

Fig. 1. A schematic diagram of the experimental setup (see the text for explanations).

1063-7850/02/2807-0539$22.00 © 2002 MAIK "Nauka/Interperiodica"

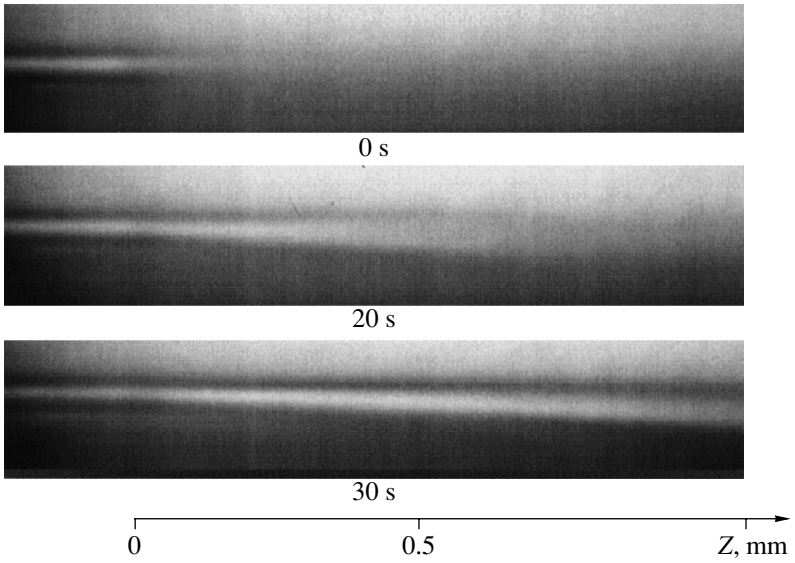

Fig. 2. Photographs illustrating the process of a polymer track formation at the edge of an optical fiber in a photopolymerizing medium.

the case of a single-mode regime, the divergence additionally depends on the position of the output cross section in the initial fiber [1].

In order to study the role of the aforementioned factors, we have experimentally traced the process of lightguide elongation for the optical fibers of various types excited by laser radiation of variable intensity. For comparison, the system was numerically modeled using a method analogous to that described previously [3]. The consideration was restricted to radially symmetric modes. The radiation parameters were taken into account by setting an initial condition for a parabolic equation describing the complex amplitude of the electric field in the photopolymerizable medium. This condition was in the form of a light amplitude distribution in the initial output cross section of the elongated optical fiber (plane x in Fig. 1). It was assumed that this distribution is the same as that in the continuing fiber, which is valid for a weakly guiding fiber [1] with the core and sheath possessing different refractive indices.

The results of investigation of the process of elongation of the waveguiding channel by means of terminal growth show that, for small intensities of the initiating radiation, the polymer track formation proceeds independently of the field distribution at the output of the fiber. In all cases, a channel is formed with a thickness on the order of the initial fiber. There are differences only in the refractive index profiles in the initial portion of the channel formed (i.e., at distances much smaller as compared to the diffraction length ka^2, where k is the wavenumber and a is the fiber diameter). The transverse size of the polymerized track varies along the z axis (Fig. 1). The amplitude of this variation decreases with increasing contrast of the photopolymerizing composition. For radiation of sufficiently large intensity, as well as in the case of lightguide formation by a Gaussian beam [3], the channel shape simply repeats the profile of the intensity distribution in a diverging initial beam.

For illustration, Fig. 2 shows photographs of a polymerized track formed at the edge of a multimodal step-index optical fiber with a core diameter of 50 μm excited by radiation with an intensity of 20 mW/mm^2 (corresponding to $\gamma \approx 2$). The photographs refer to different time instants after the onset of exposure. Variations in the transverse size of the track are small compared to the track width and cannot be distinguished in these photographs.

Acknowledgments. This study was supported by the Russian Foundation for Basic Research, project no. 01-03-33040.

REFERENCES

1. A. W. Snyder and J. D. Love, *Optical Waveguide Theory* (Chapman and Hall, London, 1983; Radio i Svyaz', Moscow, 1987).
2. G. A. Abakumov, S. N. Mensov, A. V. Semenov, *et al.*, Vysokomol. Soedin., Ser. B **42**, 1252 (2000).
3. V. A. Vdovin, A. L. Lonin, and S. N. Mensov, Zh. Tekh. Fiz. **71** (7), 67 (2001) [Tech. Phys. **46**, 853 (2001)].
4. G. A. Abakumov, S. N. Mensov, and A. V. Semenov, Opt. Spektrosk. **86** (6), 1029 (1999) [Opt. Spectrosc. **86**, 927 (1999)].

Translated by P. Pozdeev

Technical Physics Letters, Vol. 28, No. 7, 2002, pp. 541–543. Translated from Pis'ma v Zhurnal Tekhnicheskoĭ Fiziki, Vol. 28, No. 13, 2002, pp. 19–23.

Instability of a Two-Dimensional Film Flow with Inhomogeneous Temperature Field on the Free Surface

O. V. Sharypov and K. A. Medvedko

Institute of Thermal Physics, Siberian Division, Russian Academy of Sciences, Novosibirsk, Russia

e-mail: model@itp.nsc.ru

Received January 29, 2002

Abstract—It is shown that a two-dimensional stationary flow of a thin liquid film with inhomogeneous temperature distribution on the free surface exhibits a local longwave instability. A critical condition for the transition to a regular three-dimensional flow with a "stream" structure is formulated and an expression for the characteristic period is derived. *© 2002 MAIK "Nauka/Interperiodica".*

A local source of heat on the surface of a thin liquid film creates an inhomogeneous temperature field that gives rise to the thermocapillary effect. This effect can significantly influence the heat and mass transfer in the system and has to be taken into account in designing technological equipment for chemical and power plants.

A typical scheme of the problem is depicted in the figure. The x axis is parallel to the substrate and directed along the main flow. The y axis is perpendicular to the substrate and directed upward. In experiment, a local (in the x direction) source of heat may represent either a heater embedded in the substrate [1] or a combustion wave front [2]. At a sufficiently large temperature gradient $|\mathrm{grad}\,T|$ on the liquid surface, the flow acquires a three-dimensional (3D) structure whereby the main part of the liquid is gathered into streams periodic in the z direction. In the 2D flow regime, the film thickness does not remain constant and, for a certain critical value of $|\mathrm{grad}\,T| = |T_x|_{\mathrm{cr}}$, the liquid flow exhibits local arrest on the film surface [3]. Higher values of $|\mathrm{grad}\,T|$ in the 2D model correspond to a flow regime with reverse-flow zones. We believe that this critical condition is related to the loss of stability of the 2D flow structure with respect to small 3D perturbations.

Let us consider the problem of stability of a stationary 2D solution with respect to 3D perturbations monotonic in $|x|$ and periodic in z in the vicinity of the local flow arrest point (i.e., at $x \longrightarrow 0$, $u|_{x\to 0,\, y\to h} \longrightarrow 0$). This condition implies that the values of some thermodynamic and hydrodynamic parameters exhibit extremal behavior:

$$\begin{gathered} T_x|_{x\to 0,\, y\to 0} \longrightarrow (T_x)_{\mathrm{cr}}, \quad T_{xx}|_{x\to 0,\, y\to h} \longrightarrow 0, \quad T_{yy}|_{x\to 0,\, y\to h} \longrightarrow 0, \\ \sigma_{xx}|_{x\to 0} \longrightarrow 0, \quad h_x|_{x\to 0} \longrightarrow 0, \quad u_x|_{x\to 0} \longrightarrow 0, \\ v|_{x\to 0} \longrightarrow 0, \qquad v_x|_{x\to 0} \longrightarrow 0, \qquad v_y|_{x\to 0} \longrightarrow 0. \end{gathered} \tag{1}$$

Here, h is the film thickness, σ is the surface tension, and u and v are the x- and y-components of the velocity, respectively; the subscripts t, x, y, z denote differentiation with respect to the corresponding coordinate. Below, we neglect the heat flux through the free surface, which is expressed as $T_y|_{x\to 0,\, y\to h} \longrightarrow 0$, and ignore the mass and momentum transfer between gas and liquid phases.

With an allowance for the properties (1) of the 2D solution in the region of $x \longrightarrow 0$, the equations of continuity and the Navier–Stokes equations in the linear approximation can be written as

$$\begin{cases} u'_x + v'_y + w'_z = 0; \\ u'_t + uu'_x + v'u_y + p'_x/\rho = \xi(u'_{xx} + u'_{yy} + u'_{zz}); \\ v'_t + uv'_x + p'_y/\rho = \xi(v'_{xx} + v'_{yy} + v'_{zz}); \\ w'_t + uw'_x + p'_z/\rho = \xi(w'_{xx} + w'_{yy} + w'_{zz}), \end{cases} \tag{2}$$

where t is the time, w is the z-component of velocity, p is the pressure, ρ is the density, and ξ = const is the kinematic viscosity; the upper prime sign denotes perturbation of the 2D problem solution. In the linear approximation, the boundary conditions on the perturbed free surface are as follows:

$$\begin{cases} u'_y + h'u_{yy} + v'_x = \sigma'_x(\rho\xi)^{-1}; \quad v' = h'_t; \\ w'_y + v'_z = \sigma'_z(\rho\xi)^{-1}, \quad y = h; \\ p'(\rho\xi)^{-1} + (h'_{xx} + h'_{zz})\sigma(\rho\xi)^{-1} + h'_x u_y = 2v'_y + h'\xi^{-1}|\mathbf{g}|\cos\theta, \quad y = h, \end{cases} \tag{3}$$

where **g** is the acceleration of gravity and θ is the angle of deviation from the horizontal plane. Note that relationships (3) contain perturbed derivatives of the surface tension, which are functions of the temperature: $\partial\sigma'/\partial x_i = (d\sigma/dT)(\partial T'/\partial x_i)_{y=h}$, $d\sigma/dT$ = const. A relationship between T' and perturbations of the hydrodynamic parameters at $y = h$ can be obtained from a linearized equation of heat transfer written for the perturbed free surface.

Considering perturbations with a wavelength much greater than the film thickness, we can ignore the terms related to the conductive heat transfer in the heat transfer equation, provided that $\mathrm{Re}\cdot\mathrm{Pr} \gg 1$, where $\mathrm{Re} = h_\infty^3\xi^{-2}|\mathbf{g}|\sin\theta$ is the Reynolds number, Pr is the Prandtl number, and the subscript ∞ refers to remote points far upstream from the temperature inhomogeneity site. Taking into account conditions (1), we obtain

$$\sigma'_t = -\sigma_x(u' + u_y h'), \quad x \longrightarrow 0, \quad y = h. \tag{4}$$

Equations (2)–(4) contain the 2D flow characteristics, which can be approximately represented as

$$u|_{x\to 0} = f_1(y),\ u_y|_{x\to 0} = f_2(y),\ \sigma|_{x\to 0} = \text{const},$$

$$\sigma_x|_{x\to 0} = (\sigma_x)_{\mathrm{cr}} = \text{const},$$

$$u_y|_{x\to 0,\, y=h} = (\rho\xi)^{-1}(\sigma_x)_{\mathrm{cr}} = \text{const},$$

$$u_{yy}|_{x\to 0,\, y=h} = -\xi^{-1}|\mathbf{g}|\sin\theta = \text{const}.$$

Taking this into account, a solution to problem (2)–(4)

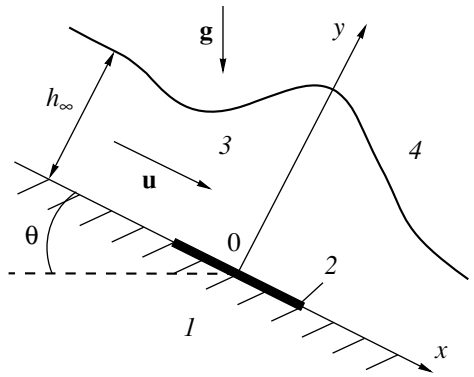

A schematic diagram of the film flow: (*1*) substrate; (*2*) heater; (*3*) liquid; (*4*) gas.

can be written in the following general form:

$$\begin{bmatrix} H'(x, y, z, t) \\ \sigma'(x, z, t) \\ h'(x, z, t) \end{bmatrix} = \sum_{j=1}^{\infty}\sum_{s=1}^{S} \begin{bmatrix} (H'_s(y))_j \\ (\delta\sigma_s)_j \\ (\delta h_s)_j \end{bmatrix} \exp(\lambda_j x + i\kappa_j z + \Omega_j t), \tag{5}$$

where $H' \equiv \{u', v', w', p'\}$; subscript *s* refers to the wave perturbation modes (each representing a superposition of harmonics); $i = \sqrt{-1}$; Ω_j, κ_j, and λ_j are constant decrements and wavenumbers of the perturbations, such that $\mathrm{Im}(\kappa_j) = 0$, $\kappa_j \geq 0$, $\mathrm{Im}(\lambda_j) = 0$, and $(x\lambda_j) \leq 0$. Substituting (5) into (2), we obtain the Orr–Sommerfeld equation

$$V_{\varphi\varphi\varphi\varphi} + 2(\bar\lambda^2 - \bar\kappa^2)V_{\varphi\varphi} + (\bar\lambda^2 - \bar\kappa^2)^2 V - (\bar\Omega + \bar\lambda\bar u)(V_{\varphi\varphi} + (\bar\lambda^2 - \bar\kappa^2)V) = \bar\lambda V\mathrm{Re}, \tag{6}$$

where $V = (v'_s(y))_j$, $\varphi = y h_\infty^{-1}$, $\bar\kappa = \kappa_j h_\infty$, $\bar\lambda = \lambda_j h_\infty$, $\bar\Omega = \Omega_j h_\infty^2\xi^{-1}$, and $\bar u = u h_\infty\xi^{-1}$.

In the case of shortwave perturbations, $\bar\kappa \geq 1$, we can neglect the convective and capillary terms in comparison with the viscosity effects in the initial equations. Then the problem reduces to description of the gravitational–capillary waves with small amplitudes on the surface of the immobile liquid ($\bar\lambda \longrightarrow 0$, $u' \longrightarrow 0$). Taking into account the condition $V = 0$ at $\varphi = 0$ for a thin liquid film ($\bar\gamma_s \ll 1$), we arrive at the well-known relationship [4]

$$\Omega^2 + 4\xi\kappa^2\Omega + \sigma\rho^{-1}\kappa^4 h + \kappa^2 h|\mathbf{g}|\cos\theta \approx 0, \tag{7}$$

which implies that the shortwave perturbations are decaying.

For an analysis of the longwave case, $\bar\kappa \ll 1$, let us consider the solution to Eqs. (2) near the free surface ($|\varphi - 1| \ll 1$). In this region, effects related to the liquid viscosity are least significant. Assuming that we may neglect the viscosity terms for the longwave perturbations in Eqs. (2) and taking into account that $u|_{x\to 0,\, y\to h} \longrightarrow 0$, we can write Eq. (6) in a significantly simpler form: $\bar\Omega V_{\varphi\varphi} + \bar\lambda V\mathrm{Re} = 0$. This reduces the

problem to solving a system of algebraic equations and yields the following expressions:

$$\Omega \approx \pm 9\kappa(\sigma_x)_{cr}^2/(4\rho^2\xi|\mathbf{g}|\sin\theta); \quad \lambda \approx \mp\kappa, \tag{8}$$

which were obtained assuming that $l_\sigma \gg h_\infty$ and $\kappa^2 l_\sigma^2 \gg \cos\theta$ ($l_\sigma^2 = \sigma/(\rho|\mathbf{g}|)$ is the capillary constant). The condition that $x\lambda_j \le 0$ for $x > 0$ implies that the exponent λ is nonpositive ($\lambda \le 0$) and, according to (8), the increment is nonnegative ($\Omega \ge 0$). Therefore, small perturbations tend to grow and the 2D stationary solution proves to be unstable. Note that relationship (8) does not take into account the damping of shortwave perturbations and cannot predict the wavelength Λ_* of the most rapidly growing perturbation.

In order to expand the domain of applicability of Eq. (8), we can introduce a small correction representing result (7) obtained above for the shortwave perturbations with neglect for the viscous dissipation effects:

$$\Omega_j \approx 9\kappa_j(\sigma_x)_{cr}^2(4\rho^2\xi|\mathbf{g}|\sin\theta)^{-1} - 2\kappa_j^3 h(\sigma_x)_{cr}^{-2}\sigma\rho\xi|\mathbf{g}|\sin\theta/9. \tag{9}$$

Using this expression, we can estimate the Λ_* value as

$$\Lambda_* \approx 2\pi l_\sigma(2/3\mathrm{Re}h_\infty/h\sin\theta)^{-1/2}(\sigma_x)_{cr}^{-2} \times (2/3\rho h_\infty|\mathbf{g}|\sin\theta)^2 \approx 5.3\times 10^{-3}\ \mathrm{m}. \tag{10}$$

This estimate refers to a 25% aqueous solution of C_2H_5OH for Re = 2/3, $\theta = \pi/2$, and $T_\infty = 300$ K ($h_\infty \approx 1.26 \times 10^{-4}$ m, $l_\sigma = 1.91 \times 10^{-3}$ m). The estimate obtained within the framework of the linear approximation is close to the experimental data, according to which $\Lambda_* = (6.5\text{–}7.5) \times 10^{-3}$ m [1]. For $(\sigma_x)_{cr} \sim h_\infty\rho|\mathbf{g}|\sin\theta$, formula (10) yields a relation $\Lambda_* \sim (\sin\theta)^{-1/2}$ for a fixed Re value. This behavior was observed experimentally [5].

The above analysis was performed for a critical flow regime, in which a local flow arrest takes place on the film surface. If the critical condition is not satisfied, perturbations are carried with the liquid flow away from a narrow region where they could be enhanced and hence, do not grow to a significant amplitude. Therefore, this condition can serve as a criterion for the transition to a 3D "stream" flow. This criterion indicates the limits for the possibility of ignoring the small-scale 3D structure of a film flow and describing the system using a 2D model.

REFERENCES

1. O. A. Kabov, I. V. Marchuk, and V. M. Chupin, Russ. J. Eng. Thermophys. **6** (2), 105 (1996).
2. A. A. Korzhavin, V. A. Bunev, D. M. Gordienko, *et al.*, Fiz. Goreniya Vzryva **34** (3), 15 (1998).
3. O. V. Sharypov, K. A. Medvedko, and A. V. Fomin, Teplofiz. Aéromekh. **8** (3), 453 (2001).
4. L. D. Landau and E. M. Lifshitz, *Course of Theoretical Physics*, Vol. 6: *Fluid Mechanics* (Nauka, Moscow, 1986; Pergamon, New York, 1987), Parag. 62.
5. O. A. Kabov, J. C. Legros, A. V. Muzykantov, *et al.*, in *Proceedings of APOLLONIA'99: Joint Meeting of the 4th Workshop "Transport Phenomena in Two-Phase Flow" and "EFCE Working Party on Multiphase Fluid Flow," Sozopol, Bulgaria, 1999*, p. 243.

Translated by P. Pozdeev

Technical Physics Letters, Vol. 28, No. 7, 2002, pp. 544–546. Translated from Pis'ma v Zhurnal Tekhnicheskoĭ Fiziki, Vol. 28, No. 13, 2002, pp. 24–29.

On the Possibility of Creating a Superfast-Recovery Silicon Carbide Diode

I. V. Grekhov, P. A. Ivanov, A. O. Konstantinov, and T. P. Samsonova

Ioffe Physicotechnical Institute, Russian Academy of Sciences, St. Petersburg, 194021 Russia

e-mail: Pavel. Ivanov@pop.ioffe.rssi.ru

Received February 14, 2002

Abstract—The possibility of a superfast (<1 ns) termination of the reverse current during the recovery of a 4H-SiC diode with a $p^+p_0n^+$ structure is experimentally demonstrated for the first time. It is shown that the gate recovery process is much like that taking place in inverse-recovery silicon diodes. © *2002 MAIK "Nauka/Interperiodica".*

Having a critical breakdown field strength E_b about ten times as high, and an electron saturation velocity v_s twice as high as the analogous values for silicon, silicon carbide (SiC) is a promising material for high-power electronics. Owing to these properties, SiC-based devices must provide for a 20 times faster operation speed than their silicon counterparts at the same working voltages. In addition, the thermal conductivity of SiC is even higher than that of copper and the limiting operation temperature is three times as high as that for silicon, which is of principal significance for high-power electronic devices.

SiC-based substrates and epitaxial structures of device quality being now readily available, research and development of SiC-based analogs of high-power silicon devices is very intensive and the possibility of creating SiC diodes, transistors, thyristors (including GTOs) has been already demonstrated (see, e.g., [1– 4]). At the same time, despite obvious advantages offered by SiC for high-power pulse electronics as well, no SiC-based analogs of silicon devices for this field have been reported so far.

An example of the simplest high-power pulse device is offered by a silicon fast-recovery drift diode (FRDD) based on a high-voltage (1–2 kV) $p^+p'nn^+$ structure with a deep diffusion *pn* junction. During the forward current pulse, the *p*' and *n* layers are filled with an electron–hole plasma. This is followed by a fast-rise reverse current pulse due to the withdrawal of electrons and holes from the *n* and *p*' layers in which sharp plasma fronts are moving in the opposite directions toward the *p*'*n* junction. If the fronts are colliding at the junction plane, the subsequent current passage is due to the major carriers moving away from the *p*'*n* junction. A space-charge region is rapidly formed at the junction, which results in a sharp voltage drop and terminates the current very sharply—within a few nanoseconds or even fractions of a nanosecond. The current is switched into a parallel load, where a fast-rise voltage pulse is generated. Since the mobility of electrons in silicon is about three times that of holes, the collision of plasma fronts at the *p*'*n* junction is ensured when the total amount of the electron–hole plasma (generated by the forward current pulse) in the *p*' region is three times that in the *n* region. This is usually provided either by applying a very short (0.1–0.5 μs) direct current pulse (FRDD regime, see [4–7] etc.) or by sharply decreasing the carrier injection in the n^+n junction (inverse-recovery diode regime [8, 9]). In the latter variant, the forward current pulse duration is not restricted and the pumping can be effected (in the limiting case) by direct current.

We have studied the possibility of providing for such a superfast recovery process in SiC-based diodes with $p^+n_0n^+$ and $p^+p_0n^+$ structures (Fig. 1a). Mesa-insulated 4H-SiC diode structures with a diameter of 0.5 mm were based on homoepitaxial $p^+/n_0/n^+$ and $p^+/p_0/n^+$ structures grown on *n*-SiC substrates (Cree Inc.) by chemical vapor deposition (CVD) in a SiH_4–C_3H_8–H_2 system. The donor (nitrogen) concentration in a 40-μm-thick n_0 layer was $(3–5) \times 10^{14}$ cm^{-3}, while the acceptor (aluminum) concentration in a 12-μm-thick p_0 layer was about 8×10^{14} cm^{-3}. The concentrations of aluminum and nitrogen in the p^+ and n^+ emitter layers were on the order of 10^{19}–10^{20} cm^{-3}.

Figure 1b shows the electric circuit diagram in which the diodes were connected. The voltage source (V_1 = 200 V) provided for a quasi-dc pumping forward current of I_f = 2 A (corresponding to a current density of ~1 kA/cm^2). The voltage V_2 in the reverse current chain was varied from 275 to 500 V. The leading front of the current pulse was determined by an insulated-gate bipolar field-effect transistor (IGBT) K_2. Figure 2 (curve *1*) shows a typical oscillogram of the recovery process in the $p^+n_0n^+$ structure (V_2 = 350 V), which is essentially analogous to the results reported in [10].

1063-7850/02/2807-0544$22.00 © 2002 MAIK "Nauka/Interperiodica"

This behavior is determined by a highly asymmetric distribution of the electron–hole plasma in the diode n-base during passage of the forward current. As was pointed out in [10], some technological features of the p^+ layer growth result in that the carrier lifetime at the p^+n_0 interface is always much shorter than that in the rest of the base (the corresponding plasma distribution is depicted in Fig. 1a). For this reason, the density of plasma at the blocking p^+n_0 junction decays to zero in the very beginning of the reverse current buildup, a space-charge region appears, and the current switches from growth to decay. However, the decay proceeds slowly because of a large amount of plasma with a high carrier density at the right-hand boundary of the space-charge region, which serves as a source of the hole current through the space-charge region. This "soft recovery" process is well known in high-power silicon-based electronic devices.

It might be expected that the character of the recovery process can be fundamentally modified by changing the type of conductivity in the base region. Since the character of the plasma distribution remains the same (with a maximum at the n^+ layer), the blocking n^+p_0 junction occurs in the region of maximum plasma density. A decay in the density caused by the reverse current passage would first take place at the p^+p_0 junction, where a sharp plasma front (moving toward the n^+p_0 junction) is formed. The current is not broken because the p^+p_0 junction does not block it and the ohmic resistance of the plasma-free base region is comparatively small. Simultaneously, the plasma density at the n^+p_0 junction drops as well. However, both the space-charge region and the plasma front form at this junction only at the very end of the recovery process, when the left-hand front is approaching the junction. This feature of the process, which is of basic importance for the superfast recovery, is determined both by the high initial plasma density at the junction and by the fact that the mobility of electrons in 4H-SiC is 5–8 times that of the holes. Upon the collision of plasma fronts, no plasma is retained and the space-charge region at the n^+p_0 junction expands at maximum possible (saturated) velocity v_s, which accounts for the sharp termination of the current. This scenario of the recovery process is much like that in a silicon inverse-recovery diode [9].

Typical oscillograms illustrating the recovery process in a $p^+p_0n^+$ diode at V_2 = 275 and 500 V are presented in Fig. 2 (curves *2* and *3*, respectively). As can be readily seen, the high reverse conductivity stage (when the plasma expands from the diode base) is followed by very sharp termination of the reverse current, with a current switching time below 1 ns for V_2 = 500 V.

Thus, we have experimentally demonstrated for the first time the possibility of a superfast (<1 ns) termination of the reverse current during recovery of a 4H-SiC diode. This opens good prospects for the development of SiC-based devices for high-power nano- and subnanosecond pulse electronics.

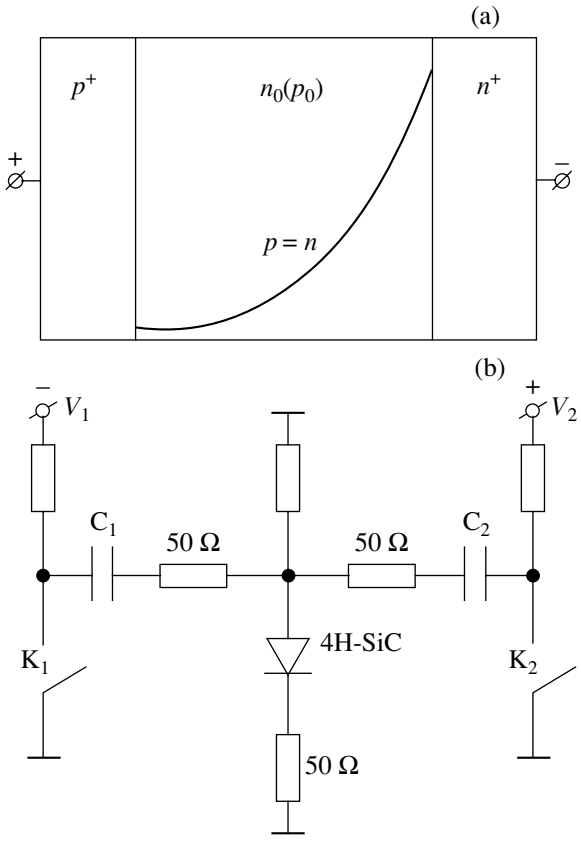

Fig. 1. Schematic diagrams showing (a) the 4H-SiC diode structure and the electron–hole plasma distribution and (b) a circuit used for measuring the diode gate recovery upon current switching from forward to reverse.

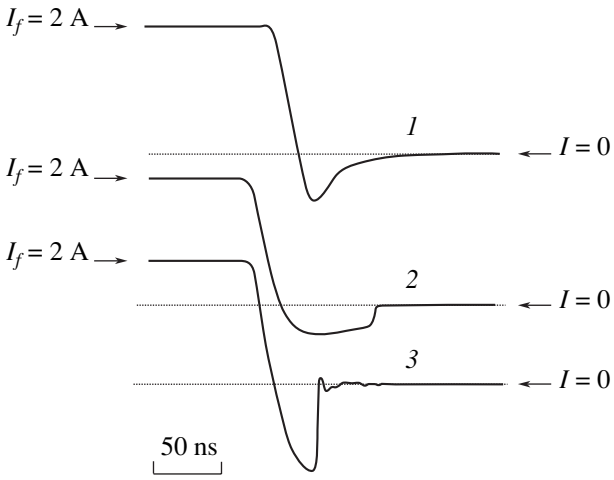

Fig. 2. Oscillograms illustrating the switching process in (*1*) $p^+n_0n^+$ and (*2*, *3*) $p^+p_0n^+$ diodes for V_2 = 350 (*1*), 275 (*2*), and 500 V (*3*).

Acknowledgments. This study was supported by the International Scientific-Technological Center

(EOARD Partnership Project No. 007040) and by the program "Generation of High-Power Electric Energy, Particle, and Electromagnetic Radiation Pulses" of the Presidium of the Russian Academy of Sciences.

REFERENCES

1. O. Kordina, J. P. Bergman, A. Henry, *et al.*, Appl. Phys. Lett. **67**, 1561 (1995).
2. Y. Sugawara, K. Asano, R. Singh, *et al.*, in *Silicon Carbide and Related Materials, 1999*, Ed. by C. H. Carter, R. P. Devaty, and G. S. Rohrer (Trans Tech Publications, Aedermannsdorf, Switzerland, 2000), Mater. Sci. Forum **338**-**342**, 1371 (2000).
3. A. K. Agarwal, S. H. Ryu, R. Singh, *et al.*, in *Silicon Carbide and Related Materials, 1999*, Ed. by C. H. Carter, R. P. Devaty, and G. S. Rohrer (Trans Tech Publications, Aedermannsdorf, Switzerland, 2000), Mater. Sci. Forum **338**-**342**, 1387 (2000).
4. S. H. Ryu, A. K. Agarwal, R. Singh, *et al.*, IEEE Electron Device Lett. **22**, 124 (2001).
5. I. V. Grekhov, V. M. Efanov, A. F. Kardo-Sysoev, *et al.*, Solid-State Electron. **28**, 597 (1985).
6. V. M. Efanov, A. F. Kardo-Sysoev, and I. A. Smirnova, Fiz. Tekh. Poluprovodn. (Leningrad) **21**, 314 (1987) [Sov. Phys. Semicond. **21**, 380 (1987)].
7. I. V. Grekhov, Izv. Akad. Nauk, Ser. Énerg., No. 1, 53 (2000).
8. I. V. Grekhov, V. A. Kozlov, and S. V. Shendereĭ, RF Certificate on Effective Model No. 7784 (1997); Byulleten' X19 (1998).
9. V. B. Voronkov, I. V. Grekhov, S. V. Korotkov, *et al.*, Prib. Tekh. Éksp., No. 2, 1 (2002).
10. M. E. Levinstein, T. T. Mnatsakanov, P. A. Ivanov, *et al.*, IEEE Trans. Electron Devices **48**, 1703 (2001).

Translated by P. Pozdeev

Technical Physics Letters, Vol. 28, No. 7, 2002, pp. 547–549. Translated from Pis'ma v Zhurnal Tekhnicheskoĭ Fiziki, Vol. 28, No. 13, 2002, pp. 30–35.

An Autostochastic System with Parametric Excitation

É. V. Kal'yanov and V. I. Kalinin

Institute of Radio Engineering and Electronics, Russian Academy of Sciences, Moscow, Russia

Received January 18, 2002

Abstract—The parametric excitation of chaotic motions in a dynamic system with a resonator in a delayed feedback chain is numerically analyzed. It is shown that the structure of oscillations can be effectively controlled for a resonator parametrically pumped with both regular and chaotic signals. © *2002 MAIK "Nauka/Interperiodica".*

Distributed systems find wide application in various fields of science and technology [1–6]. Such systems possess complicated dynamics, and it was demonstrated [4–6] that the presence of a delay leads to the instability of motions under conditions of parametric action. In particular, experiments revealed the development of self-modulated oscillations in the strongly nonequilibrium domain during the parametric action upon systems with delay [4–6]. However, no theoretical analysis of this phenomenon has been undertaken so far.

In this study, the phenomenon of parametric excitation of nonlinear oscillations in a dynamic system, including a "pumping" subsystem with complicated behavior and a "pumped" subsystem with delay, is analyzed by numerical methods. The cases of parametric actions using regular and chaotic signals are considered in order to assess the possibility of controlling the structure of nonlinear oscillations in the system. In recent years, problems pertaining to the control of nonlinear system dynamics have drawn the considerable attention of researchers (see, e.g., [7]).

The dynamic system under consideration is described by a set of equations

$$\begin{aligned}
&\frac{d^2x}{dt^2} + 2\delta_0\frac{dx}{dt} + x = f_-(x, y) - Ry,\\
&\frac{dy}{dt} + cy = f_+(x, y),\\
&\frac{d^2z}{dt^2} + \frac{\varphi(x)}{Q}\frac{dz}{dt} + [\varphi(x)]^2 z = \frac{[\varphi(x)]^2}{\sigma}\frac{dF(u)}{dt},\\
&\delta\frac{du}{dt} + u = z(t-\tau),
\end{aligned} \tag{1}$$

where x, y, z, and u are the dynamic variables; $f_\pm(x, y) = \beta \pm xy$ and $F(u) = \sigma Bu\exp(-u^2)$ are nonlinear functions; and δ_0, R, B, c, β, Q, ω_0, δ, σ, and τ are constant parameters. The function $\varphi(x) = \omega_0(1 + \alpha x(t))$ describes the parametric variation of the resonator frequency in the delayed feedback chain of the system.

The first two equations of the dynamic system (1) describe a dissipative subsystem of the Rössler type, which features either a regular behavior (for $\delta_0 = 0.1$, $R = -2.8$, $\beta = 0.2$, $c = 2.6$) or a chaotic behavior (for $\delta_0 = 0.15$, $R = -8.8$, $\beta = 0.4$, $c = 8.5$). The third and fourth equations in (1) determine a nonautonomous subsystem with the argument delayed by the time τ. A resonator in the feedback chain of the latter subsystem is pumped by output oscillations $x(t)$ of the former subsystem.

The phase portraits $(x, \dot{x})$ for both regular (Fig. 1a) and chaotic (Fig. 1b) oscillations in the former subsystem were calculated for the values of the parameters indicated above. In the autonomous regime ($\alpha = 0$), behavior of the nonlinear subsystem with delay is characterized by a simple limiting cycle with $\omega_0 = 6.4$, $Q = 10$, $B = 0.6$, $\delta = 0.1$, and $\tau = 2$ (Fig. 1c).

As a result of the parametric pumping of the resonator by a regular signal with the level $\alpha = 0.18$, the behavior of the nonlinear subsystem with delay changes from the simple limiting cycle to a chaotic attractor (Fig. 1d). Thus, a chaotic regime is stimulated so that the oscillations are controlled, which is manifested by the nonlinear subsystem being forced to perform chaotic rather than regular motions.

When the resonator is parametrically pumped by chaotic oscillations corresponding to an attractor of the Rössler type (Fig. 1b), the subsystem with delay also performs chaotic motions. For $\alpha = 0.006$, the corresponding chaotic attractor has a form similar to that in Fig. 1d. In the case of a chaotic pumping, a lower signal level α is required for stimulating chaotic motions in the system. This is related to the fact that the magnitude of chaotic oscillations in the pumping system (for the indicated parameters) is several times greater than the amplitude of periodic motions.

The difference between the results of chaotic and regular pumping is illustrated by the bifurcation dia-

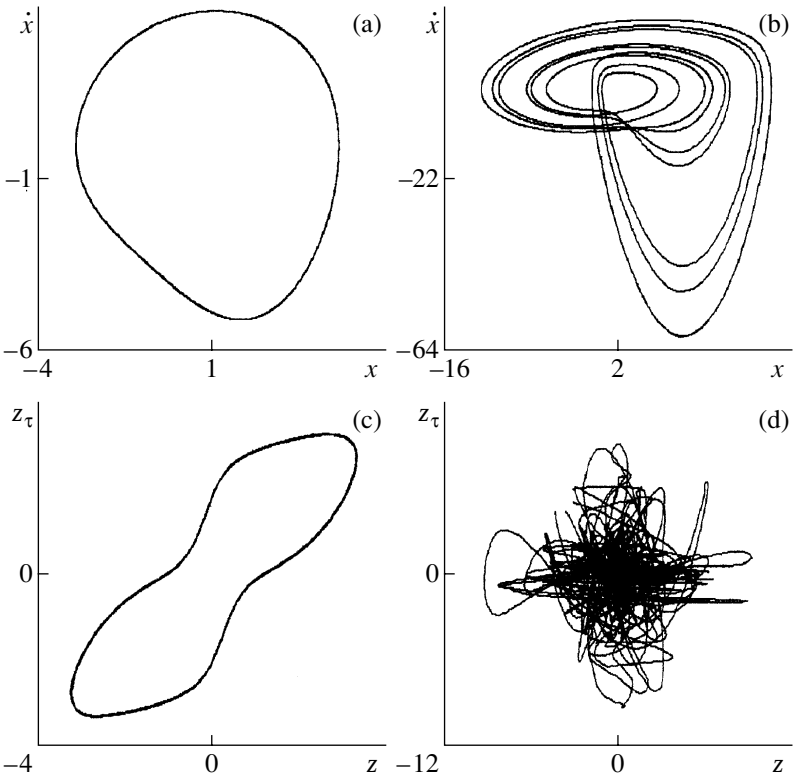

Fig. 1. Attractors corresponding to oscillations of the (a, b) pumping signal (regular and chaotic, respectively) and (c, d) pumped subsystem with delay (c) for autonomous operation and (d) under the action of a regular signal; $z_\tau = z(t - \tau)$.

grams of changes in the maximum values [z] of the oscillation process $z(t)$ depending on the pumping (bifurcation) parameter α (Fig. 2). For a regular pumping, the bifurcation parameter exceeding a critical level ($\alpha = 0.15$) leads to a random scatter of points in the bifurcation diagram (Fig. 2a), which is evidence of the excitation of chaotic oscillations in the system. In the case of a weak regular action ($\alpha < 0.02$), the system performs quasi-periodic motions (Fig. 2b) on the surface of a two-dimensional (2D) invariant torus with two nonmultiple frequencies: the frequency of autooscillations in the subsystem with delay and the frequency of periodic pumping. As the parameter varies in the interval $\alpha \in [0.02; 0.065]$, the subsystem with delay exhibits a periodic self-modulation of the oscillations with nonmultiple frequency. A geometric image of the parametrically excited three-frequency oscillations is a 3D torus in the phase space of the nonlinear subsystem. Figure 2b shows a fragment of the bifurcation diagram from Fig. 2a calculated for the interval $\alpha \in [0; 0.075]$, in which two-frequency motions correspond (for $\alpha < 0.02$) to simply connected cross sections of the 2D torus. Three-frequency motions (for $0.02 < \alpha < 0.065$) correspond to multiply connected cross sections of the 3D torus.

In the case of pumping by the chaotic signal $x(t)$, the diagram of [z] as a function of the bifurcation parameter α is similar to that depicted in Fig. 2a. However, there is a significant distinction: even very weak chaotic pumping ($\alpha < 0.006$) implies chaotization (forced chaotic modulation) of the output oscillations $z(t)$ (Fig. 2c). The simply connected cross sections of the bifurcation diagram exhibit the scatter of random [z] values. As the chaotic pumping level increases in the interval $\alpha \in [0.006; 0.015]$, self-modulation instability develops and a self-modulated oscillation regime is established in the subsystem with delay. The cross sections of the bifurcation diagram become multiply connected and are filled with random points. In the strongly nonequilibrium region ($\alpha > 0.015$), the multiply connected domains break and the bifurcation diagram again displays simply connected cross sections filled with chaotic points.

The mechanism of parametric excitation of the developed chaotic motions is the same for regular and chaotic pumping. In both cases, the external pumping stimulates potential self-modulation modes in the nonlinear subsystem with delay.

The above analysis shows that a parametric action leads to the excitation of chaotic oscillations in the nonlinear subsystem with delay. In the absence of external action, a regular regime is established in an autonomous system with the same parameters. The parametric pumping can be provided by both regular and chaotic

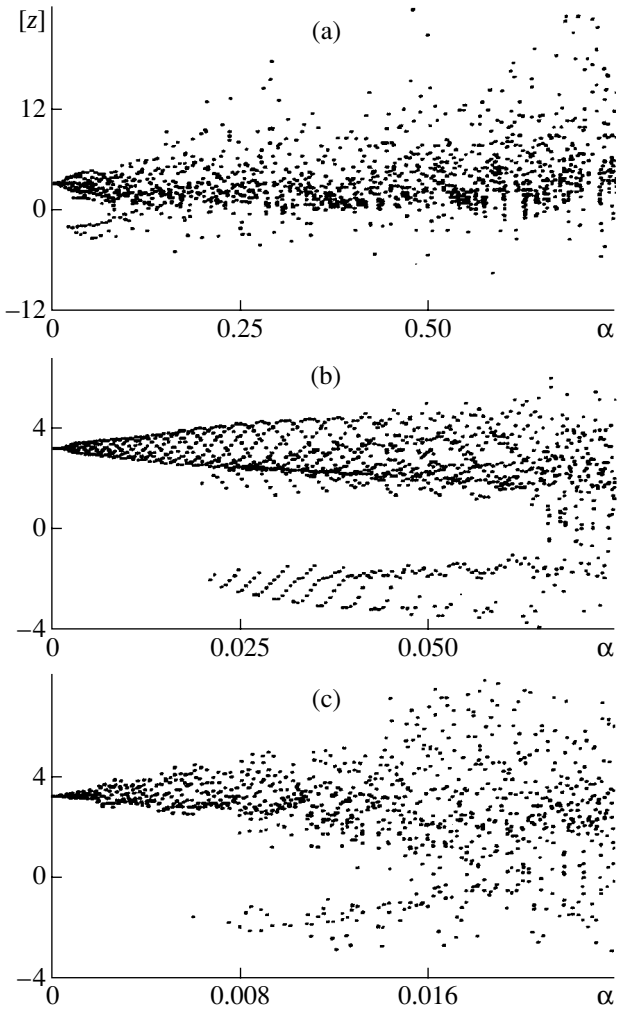

Fig. 2. Bifurcation diagrams of changes in maximum values [z] of the oscillation process $z(t)$ depending on the external action parameter α for (a, b) regular and (c) chaotic pumping.

signals. The effect of parametric action on nonlinear systems with delay can be used as a means of controlling the structure of oscillations by switching from regular to chaotic regime and vice versa.

Acknowledgments. This study was supported by the Russian Foundation for Basic Research (project nos. 01-02-17529 and 01-07-90349).

REFERENCES

1. L. Glass and M. C. Mackey, *From Clocks to Chaos: The Rhythms of Life* (Princeton Univ. Press, Princeton, 1988; Mir, Moscow, 1991).
2. Yu. I. Neimark and P. S. Landa, *Stochastic and Chaotic Oscillations* (Nauka, Moscow, 1987; Kluwer, Dordrecht, 1992).
3. A. S. Dmitriev and V. Ya. Kislov, *Stochastic Oscillations in Radiophysics and Electronics* (Nauka, Moscow, 1989).
4. V. I. Kalinin, N. N. Zalogin, and E. A. Myasin, Pis'ma Zh. Tekh. Fiz. **10** (21), 1311 (1984) [Sov. Tech. Phys. Lett. **10**, 554 (1984)].
5. V. I. Kalinin, N. N. Zalogin, and E. A. Myasin, in *Proceedings of the XVII International School-Workshop "Novel Magnetic Materials for Microelectronics," Moscow, 2000*, p. 336.
6. É. V. Kal'yanov and S. O. Starkov, Pis'ma Zh. Tekh. Fiz. **17** (11), 55 (1991) [Sov. Tech. Phys. Lett. **17**, 410 (1991)].
7. G. Chen, *Controlling Chaos and Bifurcations in Engineering Systems* (CRC Press, Boca Raton, 2000).

Translated by P. Pozdeev

Technical Physics Letters, Vol. 28, No. 7, 2002, pp. 550–551. Translated from Pis'ma v Zhurnal Tekhnicheskoĭ Fiziki, Vol. 28, No. 13, 2002, pp. 36–39.

Matching a Line to an Explosive-Emission Diode in Local Therapy Devices

G. A. Mesyats

Institute of Electrophysics, Ural Division, Russian Academy of Sciences, Yekaterinburg, Russia

e-mail: mesyats@pran.ru

Received January 31, 2002

Abstract—It was previously suggested to use explosive-emission diodes generating X-ray pulses for local therapy purposes. The diode is usually powered by pulses supplied via a thin electrical cable. Effective operation of such a system requires that maximum pulsed energy transmitted via the cable would be absorbed in the diode. Taking into account nonlinearity of the current–voltage characteristic of the diode, it is impossible to ensure the line-to-diode matching in the general case. It is suggested to match the cable to the load by selecting a proper shape of the voltage pulse supplied to the diode. For an explosive-emission diode with flat electrodes, a virtually perfect matching is achieved with triangular voltage pulses. *© 2002 MAIK "Nauka/Interperiodica".*

In 1979, I suggested using miniature explosive-electron-emission diodes for irradiating tumors in cavities or on the surface of the human body [1]. For this purpose, a signal from a nanosecond ($t_p \le 1$ ns) pulse generator with a signal amplitude of 10^5 V or above was supplied via a thin coaxial cable loaded with an explosive-electron-emission diode generating X-rays. The diameter of a cable transmitting extremely short voltage pulses should be on the order of a few millimeters; the X-ray emitting diode is of the same diameter.

Two problems encountered in implementing this idea is to ensure reliable operation of the cable and diode and to provide for effective energy absorption by electrons in the diode. In order to solve these problems, it is necessary to match the diode (possessing a nonlinear resistance) to the wave impedance of the cable. Using the known current–voltage characteristics of the explosive-emission diodes [2], it is possible to select a special shape of the voltage pulse for which the diode resistance would remain constant over the pulse duration. This would eliminate reflected pulses and provide for the most effective pulse energy transfer to the electron beam in the X-ray diode.

In the general case, the current–voltage characteristic of an explosive-emission diode has the form of the Child–Langmuir dynamic characteristic [2]

$$i(t) = AU^{3/2}(t)F\left(\frac{vt}{d}\right), \qquad (1)$$

where $i(t)$ is the electron current; $U(t)$ is the voltage applied to the diode; A and $F\left(\frac{vt}{d}\right)$ are a constant factor and a function depending on the diode geometry, d being the anode–cathode distance in the diode, v the cathode plasma velocity, and t the current time. The values of A and F for diodes of various types were presented elsewhere [2, 3]. According to relationship (1), the current, voltage and, hence, the diode resistance are time-dependent. Therefore, a question arises as to how the diode can be matched to the line by which the voltage $U(t)$ is supplied. In the absence of matching, waves reflected from the diode would appear in the line. Reflected from the output load of the pulse generator, these waves return to the diode and hinder its normal operation. As demonstrated below, the necessary matching for a given diode can be provided by selecting the form of the voltage as a function of time.

Let Z_0 denote the wave impedance of the line and R_d, the diode resistance. Since $R_d = U(t)/i(t)$, relationship (1) yields

$$R_d(t) = \frac{1}{AF\left(\frac{vt}{d}\right)U^{1/2}(t)}. \qquad (2)$$

The condition of the line to diode matching is

$$R_d = Z_0, \qquad (3)$$

from which it follows that the diode resistance R_d must be independent of time. This condition can be satisfied provided that

$$U(t) = \frac{1}{A^2Z_0^2F^2\left(\frac{vt}{d}\right)}. \qquad (4)$$

If the voltage varies with time according to formula (4), the diode and line are perfectly matched, whereby no reflected waves propagate in the line and the diode dissipates all energy transmitted with the voltage pulse.

1063-7850/02/2807-0550$22.00

Consider a diode with an edge-emitting cylindrical cathode of diameter D_1 such that $D_1 \gg d$. For this diode, we have [2, 3]

$$F\left(\frac{vt}{d}\right) = \left(1 - \frac{vt}{d}\right)^{-2}, \quad (5)$$

$$A = \frac{\pi A_0 D_1^2}{4d^2}, \quad (6)$$

where $A_0 = 2.3 \times 10^{-6}$ A^2 V$^{-3/2}$ is a constant in the classical Child–Langmuir formula. In this case, formula (4) can be written as

$$U(t) = \frac{16d^4\left(1 - \frac{vt}{d}\right)^4}{A_0^2\pi^2 D_1^4 Z_0^2}. \quad (7)$$

Let us express the voltage in the form $U(t) = U_0 f(t)$ and restrict consideration to the case of

$$\frac{vt}{d} \ll 1. \quad (8)$$

Then, using the approximation $\left(1 - \frac{vt}{d}\right)^4 \approx \left(1 - \frac{4vt}{d}\right)$, we obtain

$$U_0 f(t) \approx \frac{16d^4}{A_0^2\pi^2 D_1^4 Z_0^2}\left(1 - \frac{4vt}{d}\right). \quad (9)$$

According to relationship (9), the line and diode will be matched for a voltage pulse possessing a triangular shape with the amplitude

$$U_0 = \frac{16d^4}{A_0^2\pi^2 D_1^4 Z_0^2} \quad (10)$$

and the time function

$$f(t) = 1 - \frac{4vt}{d}. \quad (11)$$

For this function, the pulse full width at half-maximum (FWHM) is

$$t_p = \frac{d}{8v}, \quad (12)$$

so that condition (8) is satisfied. The voltage amplitude U_0 is selected taking into account electric strength of the cable by which the pulse is transmitted to the diode, as well as the X-ray and electron beam parameters. For example, for $U_0 = 3 \times 10^4$ V, a cable with the wave impedance $Z_0 = 50\ \Omega$, and the aforementioned value of $A_0 = 2.3 \times 10^{-6}$ A^2 V$^{-3/2}$, formula (10) yields

$$D_1/d = 8. \quad (13)$$

The value of D_1 is determined from the condition that a coaxial diode must possess a wave impedance Z_0 equal to that of the cable:

$$Z_0 = \frac{138}{\sqrt{\varepsilon}}\log\frac{D_2}{D_1}, \quad (14)$$

where ε is the relative permittivity of the diode insulation (for vacuum, $\varepsilon = 1$). For a diode with an external diameter of $D_2 = 2$ mm, relationship (14) yields $D_1 = 0.87$ mm and, according to (13), $d = 0.11$ mm. Then, the optimum pulse duration (FWHM) determined from (12) is ~0.9 ns (for a graphite cathode, $v = 1.5 \times 10^6$ cm/s).

Thus, it has been demonstrated that matching of the line by which the supply voltage pulse is transmitted to an explosive-emission diode can be provided by properly selecting the voltage pulse shape. For a triangular voltage pulse with an amplitude of 30 kV supplied to a coaxial vacuum diode with a wave impedance of 50 Ω, the optimum matching is provided for an interelectrode gap of $d = 0.11$ mm, a cathode diameter of $D_1 = 0.87$ mm, and a pulse width (FWHM) of $t_p = 0.9$ ns.

REFERENCES

1. G. A. Mesyats, in *Proceedings of the 2nd IEEE International Pulsed Power Conference, Lubbock (Texas), 1979*, p. 9.
2. G. A. Mesyats, Zh. Tekh. Fiz. **44** (7), 1521 (1974) [Sov. Phys. Tech. Phys. **19**, 948 (1974)].
3. G. A. Mesyats, *Explosive Electron Emission* (URO-Press, Yekaterinburg, 1998).

Translated by P. Pozdeev

Technical Physics Letters, Vol. 28, No. 7, 2002, pp. 552–553. Translated from Pis'ma v Zhurnal Tekhnicheskoĭ Fiziki, Vol. 28, No. 13, 2002, pp. 40–43.

Optical Confinement of a Laser Radiation in the 3.8–4.2 μm Range in a Composite Material Containing Silver Nanoparticles

I. V. Bagrov, A. P. Zhevlakov, O. P. Mikheeva, A. I. Sidorov, and V. V. Sudarikov

Institute of Laser Physics, St. Petersburg, Russia

Received November 21, 2001

Abstract—The results of experiments on the nonlinear optical confinement of a pulsed 3.8–4.2 μm laser radiation in a composite comprising a silver-halide-based dielectric matrix containing dispersed silver nanoparticles are presented. It is shown that, for a laser pulse duration of 250 ns, the energy threshold for the laser radiation confinement is 5 mJ/cm^2 and the dynamic confinement range exceeds 10. © *2002 MAIK "Nauka/Interperiodica".*

Composite optical materials containing dispersed metal nanoparticles are promising materials for high-speed nonlinear optical devices operating in the visible and near IR (NIR) range [1–3]. The spectral range of device application is determined by the position of a plasmon resonance in the metal of nanoparticles. For example, the plasmon resonance in silver (Ag) corresponds to a wavelength of 0.39 μm, while that in gold (Au) corresponds to 0.52 μm [3, 4]. For metal nanoparticles possessing a complicated structure, the plasmon resonance and the related optical nonlinearity can be shifted toward the NIR range, in particular, to 0.8–1.2 μm for Au particles [4].

Below we present experimental data demonstrating that a composite material containing dispersed silver nanoparticles may exhibit optical nonlinearity in the middle IR range, which leads to confinement of laser radiation.

The initial material for the samples was KRS-13 comprising a mixture of silver chloride and bromide (65% AgBr + 35% AgCl). The composite material was prepared by melting KRS-13 crystals in vacuum with simultaneous irradiation in the visible range. The transmission spectrum of the composite material crystallized upon this treatment exhibits an additional minimum near $\lambda = 3$ μm (Fig. 1) which was absent in the spectrum of the initial material.

Nonlinear properties of the composite were studied using radiation of an electric-discharge DF laser with a pulse duration of 250 ns and a spectrum comprising a series of lines in the region of 3.8–4.2 μm. Figure 2 presents a plot of the output (E_{out}) versus input (E_{in}) radiation energy density for a 1.5-mm-thick composite plate. It can be seen that there are two regions of confinement of the incident radiation. The first region is characterized by a confinement threshold at $E_{in} = 5$ mJ/cm^2, and the second, by $E_{in} = 25$ mJ/cm^2. For $E_{in} < 5$ mJ/cm^2, the E_{out} versus E_{in} plot is linear. The confinement effect is reversible and can be repeatedly reproduced.

Irradiation of the KRS-13 meld leads to the photolysis of AgCl and AgBr molecules with the formation of metal silver particles. In the course of subsequent crystallization, these particles are deposited onto the surface of silver halide grains to form an island film. Calculations performed using the method described in [5] showed that the permittivity of such an island film differs from that of a continuous silver layer; in particular, it exhibits a strong dispersion in the 3-μm spectral range.

The results of an electron-microscopic investigation showed that silver halide grains in a sample upon crystallization possess the shape of elongated ellipsoids

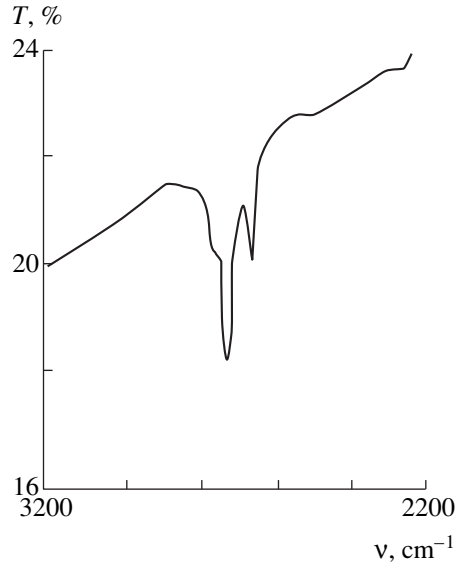

Fig. 1. The optical transmission spectrum of a 1.5-mm-thick composite plate.

1063-7850/02/2807-0552$22.00 © 2002 MAIK "Nauka/Interperiodica"

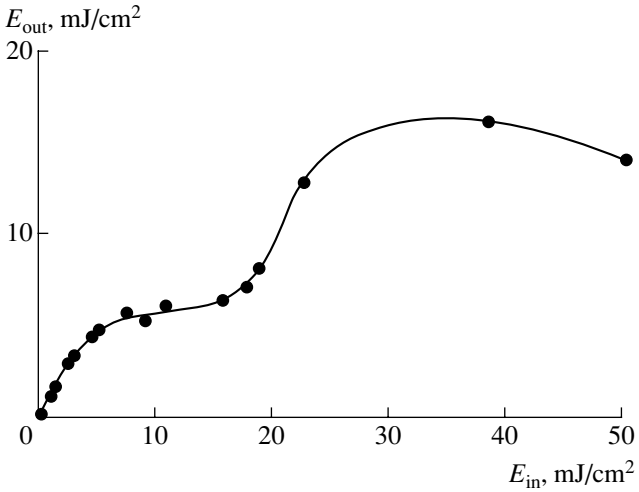

Fig. 2. The plot of output (E_{out}) versus input (E_{in}) radiation energy density for a plate of the composite with silver nanoparticles.

with a size of 150–200 nm. Therefore, the material can be considered as a dielectric medium composed of elliptic particles with a dielectric core and a coat representing a silver island film. Calculation of the optical properties of such a composite in the approximation of coated spherical particles [4, 6] showed the presence of a maximum at $\lambda \approx 3$ μm in the spectral dependence of the light absorption and scattering cross section. In addition, the composite under consideration obeys the condition of the plasmon resonance at the same wavelength [6]. Thus, the appearance of an additional absorption band in the transmission spectrum of the composite (Fig. 1) is related to a shift of the plasmon resonance toward the 3 μm region. The presence of a fine structure in this absorption band can be due to a scatter in the shape and size of the silver nanoparticles.

The phenomenon of confinement in the 3.8–4.2 μm spectral range is related to a shift of the absorption band, related to plasmon resonance, from 3 to 4 μm with a simultaneous increase in the absorption coefficient. The calculation showed that this phenomenon takes place even with a small (<1%) increase in the refractive index of the dielectric component of the composite. As is known, silver halides possess piezo-optical and elasto-optical properties [7]. Therefore, a change in the refractive index can be related to electrostriction [6, 8] under the conditions of a local field amplitude enhancement [6] inside and near the composite grains under plasmon resonance conditions. The second confinement region ($E_{in} > 25$ mJ/cm^2) is due to a change in the permittivity of components of the composite related to thermal effects in the vicinity of metal particles.

Acknowledgments. This study was supported by the International Scientific-Technological Center, project no. 1454.

REFERENCES

1. J. W. Haus, N. Kalyaniwalla, R. Inguwa, *et al.*, J. Opt. Soc. Am. B **6** (4), 797 (1989).
2. J. W. Haus, H. S. Zhou, T. M. Hirasawa, *et al.*, J. Appl. Phys. **73** (3), 1043 (1993).
3. R. D. Averitt, S. L. Westcott, and N. J. Halas, J. Opt. Soc. Am. B **16** (10), 1814 (1999).
4. R. D. Averitt, S. L. Westcott, and N. J. Halas, J. Opt. Soc. Am. B **16** (10), 1824 (1999).
5. T. Yamaguchi, H. Takahashi, and A. Sudoh, J. Opt. Soc. Am. **68** (8), 1039 (1978).
6. A. E. Neeves and M. H. Birnboim, J. Opt. Soc. Am. B **6** (4), 787 (1989).
7. *Acoustical Crystals*, Ed. by M. P. Shaskol'skaya (Nauka, Moscow, 1982).

Translated by P. Pozdeev

Technical Physics Letters, Vol. 28, No. 7, 2002, pp. 554–556. Translated from Pis'ma v Zhurnal Tekhnicheskoĭ Fiziki, Vol. 28, No. 13, 2002, pp. 44–50.

The Formation of InAs Quantum Dots in an Aluminum Oxide Matrix

D. A. Tenne[a], O. R. Bajutova[a]*, A. K. Bakarov[a], A. K. Kalagin[a], A. G. Milekhin[a], A. I. Toropov[a], and D. R. T. Zahn[b]

[a] *Institute of Semiconductor Physics, Siberian Division, Russian Academy of Sciences, Novosibirsk, 630090 Russia*
** e-mail: bajutova@thermo.isp.nsc.ru*
[b] *Institut für Physik, Universität Chemnitz, D-09107 Chemnitz, Germany*
Received February 11, 2002

Abstract—The formation of InAs quantum dots in an aluminum oxide matrix by selective oxidation of AlAs layers in an InAs/AlAs heterostructure is studied. According to the Raman spectroscopy data, the process of selective oxidation leads to stress relaxation in the InAs quantum dots and to the formation of amorphous arsenic at the boundary between oxidized and unoxidized regions. *© 2002 MAIK "Nauka/Interperiodica".*

Selective oxidation of Al(Ga)As layers with a high aluminum content is a promising method for the technology of optoelectronic devices. An important application of this technique is the production of photonic crystals [1]. At present, this method is widely and successfully employed in the fabrication of quantum-dot vertical-cavity lasers. The active region of such lasers represents an AlGaAs matrix with InAs quantum dots (QDs). The ultimate performance characteristics of lasers can be significantly improved by forming a current aperture in the course of selective oxidation (providing for an electrical and optical confinement) and by creating Al_xO_y/GaAs multilayer Bragg mirrors with high reflection coefficients [2–5]. By replacing the AlGaAs matrix with AlAs(Al_2O_3), which possesses a wider bandgap, it is possible to shift the effective lasing range toward the red spectral region.

The process of "lateral" selective oxidation of Al(Ga)As layers in GaAs/Al(Ga)As structures is currently under extensive investigation [6, 7]. It was established that some parameters (oxidation temperature, composition (x) of $Al_xGa_{1-x}As$ layers, layer thickness, mesastructure geometry) influence the kinetics of aluminum oxide formation [8, 9].

Below we report the results of investigation of the selective oxidation of AlAs layers used for the obtaining of structures with vertically aligned InAs quantum dots in an Al_xO_y matrix.

Experiment. The experimental structures were grown by molecular beam epitaxy (MBE) in a Riber 32P system. The sample structures, grown on (001)-oriented GaAs substrates, comprised five layers of self-organized InAs QDs in an AlAs matrix. The total thickness of a deposited InAs layer corresponded to two monolayers (about 0.6 nm), while the AlAs spacer layer was about 12 nm thick. The substrate temperature during the MBE growth of InAs QDs was 440°C. The subsequent 6-nm-thick AlAs overlayer was grown at the same temperature. Then the substrate temperature was increased to 580°C and a 6-nm-thick AlAs layer was grown. The total thickness of the AlAs matrix amounted to 130 nm. After completion of the active region formation, the heterostructure was coated with a 12-nm-thick layer of GaAs. The growth process was monitored by the reflection high-energy electron diffraction (RHEED) technique.

The samples containing InAs QDs were oxidized at 360°C in a horizontal quartz reactor to which the vapor of distilled water (heated to 95°C in a bubbler) was supplied with a carrier gas (N_2). At a nitrogen flow rate of 0.3 l/min, the lateral oxidation front for 30–40 min is 18–22.5 μm.

The samples with QDs before and after oxidation were studied by Raman spectroscopy. The Raman spectra were recorded in a backscattering geometry on a Dilor XY800 spectrometer using nonpolarized radiation of an Ar^+ laser operating at 514.5 nm (2.41 eV). The oxidation front was examined using a microscope capable of focusing the light within a spot size of 1 μm on the sample.

Results and discussion. Figure 1 shows a high-resolution electron-microscopic (HREM) image of a sample cross section. The dark regions correspond to layers with InAs QDs, while the light bands represent AlAs layers. As can be seen, InAs QDs possess a pyramidal shape with a base length on the order of 10 nm and a height of about 2 nm.

Figure 2a presents the plots of oxidation depth versus time for a 120-nm-thick AlAs layer oxidized at various temperatures in the range from 360 to 420°C. The curves are well described within the framework of the oxidation model proposed by Evans [10]. In the initial

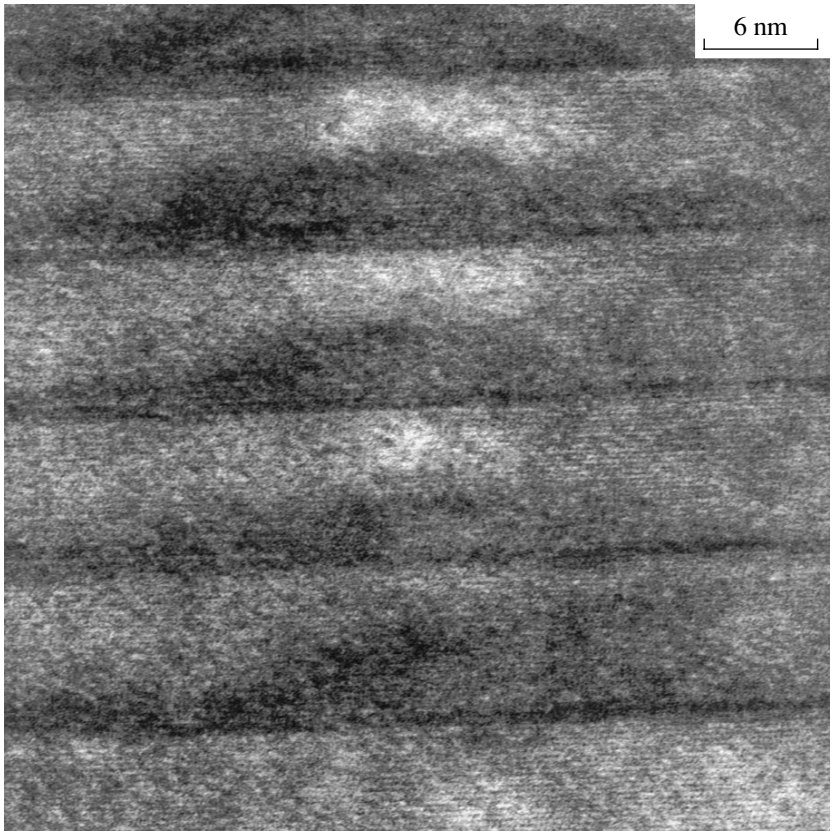

Fig. 1. A HREM micrograph of the sample structure showing dark regions corresponding to InAs QDs. A GaAs substrate is in the bottom part of the image.

stage, the oxidation rate varies linearly with time because the lateral oxidation process is controlled by the oxidation reaction. It is suggested that reagents involved in the oxidation process are supplied via pores in the oxide layer formed at a boundary with the N_2 + H_2O medium. The oxidation process continues as long as the pores can provide for the supply of water and/or oxygen ions to the reaction front. In the course of oxidation, the pores are blocked by the reaction products. This hinders delivery of the reagents, and the reaction gradually slows down (and eventually stops). The oxidation process is described by the following reactions [11]:

$$2AlAs + 6H_2O_{(g)} = Al_2O_3 + As_2O_3 + 6H_2, \quad (1)$$

$$As_2O_3 + 3H_2 = 2As + 3H_2O_{(g)}. \quad (2)$$

As can be seen, the reaction products must include intermediate As_2O_3 and amorphous As, which is confirmed by the Raman spectra. According to the HREM data, the oxidation of AlAs is accompanied by the formation of an amorphous Al_xO_y matrix.

Figure 2b shows plots of the initial oxidation rate and the final oxidation depth versus temperature in Arrhenius coordinates. Using these relationships, (according to [10]) we calculated the activation energy for the oxidation reaction at the AlAs/oxide interface ($E_1 = 1.30 \pm 0.05$ eV) and for the transport of reagents through the oxide layer ($E_2 = 0.94 \pm 0.01$ eV).

Figure 3 shows typical Raman spectra measured in the vicinity of the oxidation front at a 1.5-μm step. As can be seen from these data, the Raman spectrum in the

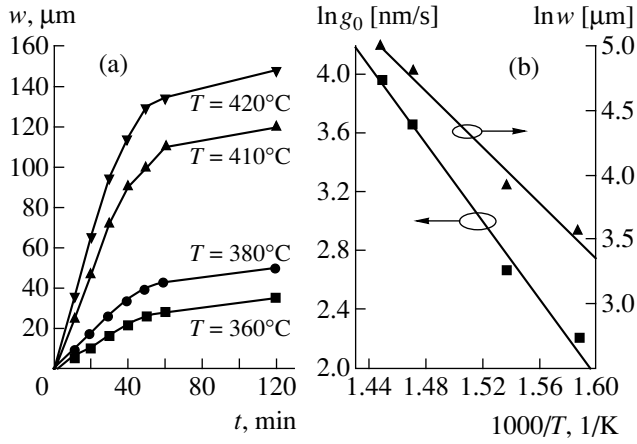

Fig. 2. Plots of (a) the lateral oxidation depth w versus exposure time t for 120-nm-thick AlAs layers oxidized at various temperatures and (b) the initial oxidation rate g_0 and the final oxide thickness w versus temperature T (in the Arrhenius coordinates).

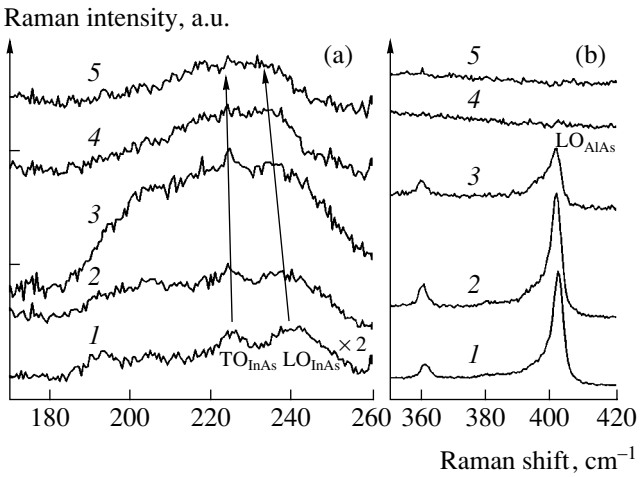

Fig. 3. The Raman spectra of (a) InAs and (b) AlAs measured in the vicinity of the oxidation front at a 1.5-μm step (spectrum *1* corresponds to an unoxidized region). Arrows indicate variation of the optical phonon frequencies in InAs.

unoxidized region (Fig. 3, curve *1*) displays the peaks at 240 and 225 cm^{-1} for InAs (402 and 360 cm^{-1} for AlAs) corresponding to longitudinal (LO) and transverse (TO) optical phonons, respectively. The LO and TO frequencies in the bulk InAs amount to 238.6 and 217 cm^{-1}, respectively. The LO and TO frequencies observed for the structure with QDs exceed the values for the bulk InAs.

There are two factors responsible for the shift of the optical phonon frequencies in InAs QDs: (i) mechanical stresses in the layers with QDs caused by a mismatch of the InAs and AlAs lattices and (ii) localization of the optical phonons. The positions of optical phonons in the Raman spectra indicate that the nanostructures under consideration are pseudomorphous; that is, they contain no dislocations leading to relaxation of the mechanical stresses. This is also confirmed by the HREM data. The stresses lead to high-frequency shift of the optical phonons [12]. Localization of the optical phonons in QDs leads to a low-frequency shift of the LO and TO lines [13].

On approaching the oxidation front (Fig. 3, curves *2* and *3*), the Raman spectrum displays a broad band in the region of 190–250 cm^{-1}, the optical phonon lines in InAs exhibit a low-frequency shift, and those in AlAs decrease in intensity. Upon traversing the oxidation front, the intensity of the band at 190–250 cm^{-1} decreases and the lines of the optical phonons in AlAs disappear (Fig. 3b, curves *4* and *5*). Subsequent motion away from the oxidation front does not change the Raman spectrum. The decrease in intensity of the optical phonons in AlAs is evidence of the oxidation of AlAs layers, while the appearance of a broad band is indicative of the formation of amorphous As clusters [14]. The low-frequency shift of the LO and TO phonons of InAs observed in the experiment is evidence of the relaxation of mechanical stresses in InAs QDs in the oxidized region. It should be noted that the observed Raman spectra contain no lines at 475 cm^{-1}, which is indicative of the absence of amorphous As_2O_3 (a possible intermediate reaction product [10]).

Thus, we obtained InAs QDs in an amorphous aluminum oxide matrix using the method of selective oxidation, showed that the oxidation process leads to the relaxation of stresses in InAs QDs, and revealed the presence of amorphous arsenic at the boundary between oxidized and unoxidized regions.

Acknowledgments. The authors are grateful to S. Schulze for kindly providing HREM micrographs of the sample cross sections.

This study was supported by the Russian Foundation for Basic Research (project no. 02-16969), the Volkswagen Foundation (grant I/76837), and the INTAS Foundation (grant YS 2001/2-12).

REFERENCES

1. J. Sabarinathan, P. Bhattacharua, D. Zhu, *et al.*, Appl. Phys. Lett. **78** (20), 3024 (2001).
2. Z. Zou, D. L. Huffuker, S. Csutak, *et al.*, Appl. Phys. Lett. **75** (1), 22 (1999).
3. J. J. Wierer, P. W. Evans, N. Holonyak, *et al.*, Appl. Phys. Lett. **72** (21), 2742 (1998).
4. V. A. Gaĭsler, A. I. Toropov, A. K. Bakarov, *et al.*, Pis'ma Zh. Tekh. Fiz. **25** (19), 40 (1999) [Tech. Phys. Lett. **25**, 775 (1999)].
5. A. V. Sakharov, I. L. Krestnikov, N. A. Maleev, *et al.*, Fiz. Tekh. Poluprovodn. (St. Petersburg) **35** (7), 889 (2001) [Semiconductors **35**, 854 (2001)].
6. J. P. Landesman, A. Fiore, J. Nagle, *et al.*, Appl. Phys. Lett. **71** (17), 2520 (1997).
7. S. K. Cheong, B. A. Bunker, T. Shibata, *et al.*, Appl. Phys. Lett. **78** (17), 2458 (2001).
8. T. Langenfelder, St. Schroder, and H. Grothe, J. Appl. Phys. **82** (7), 3548 (1997).
9. H. Nickel, J. Appl. Phys. **78** (8), 5201 (1995).
10. U. R. Evans, *The Corrosion and Oxidation of Metals* (Arnold, London, 1961), pp. 819–854.
11. C. I. H. Ashby, J. P. Sullivan, K. D. Choquette, *et al.*, J. Appl. Phys. **82** (6), 3134 (1997).
12. F. Cerdeira, C. J. Buchenauer, F. H. Pollak, *et al.*, Phys. Rev. B **5**, 580 (1972).
13. D. A. Tenne, V. A. Haisler, A. K. Bakarov, *et al.*, Phys. Status Solidi B **224** (1), 25 (2001).
14. G. P. Schwartz, B. E. Schwartz, D. DiStefano, *et al.*, Appl. Phys. Lett. **34**, 205 (1979).

Translated by P. Pozdeev

Technical Physics Letters, Vol. 28, No. 7, 2002, pp. 557–559. Translated from Pis'ma v Zhurnal Tekhnicheskoĭ Fiziki, Vol. 28, No. 13, 2002, pp. 51–56.

Finite-Element Modeling of the Behavior of Strained Porous Ceramics

O. V. Kilina, P. S. Kilin, and S. N. Kul'kov

Institute of Strength Physics and Materials Science, Siberian Division, Russian Academy of Sciences, Tomsk, 634055 Russia

e-mail: kulkov@ispms.tsc.ru

Received January 22, 2002

Abstract—The behavior of strained porous ceramics is studied by methods of finite-element modeling. It is shown that loading of such a structurally inhomogeneous material leads to the formation of localized deformation regions, oriented at 45° relative to the axis of loading, which divide the sample into fragments with an average size equal to the mean distance between pores. The behavior of a sample in the course of loading can be divided into three stages characterized by the (i) absence of local fracture, (ii) accumulation of the volume of fractured material, and (iii) complete fracture. © *2002 MAIK "Nauka/Interperiodica".*

The strength of a material is determined by the mechanism of deformation. An interesting feature in the behavior of strained materials is related to the formation of local plastic deformation regions. Materials possessing an inhomogeneous structure are usually studied in the case of large deformations [1]. Pores are among the possible structural inhomogeneities, the presence of which qualitatively change the mechanism of deformation. The experimental investigation of porous materials encounters certain difficulties. For this reason, it is important to develop methods for modeling the behavior of strained porous ceramics in order to determine the regions of strain localization, stress concentrators, and deformation stages in the course of loading.

We employed the COSMOS program package [2] for numerical modeling of a real porous structure [3], which served as a basis for solving a planar elastic deformation problem. The model region had dimensions of 80×80 μm and a porosity of 10%. The exper-

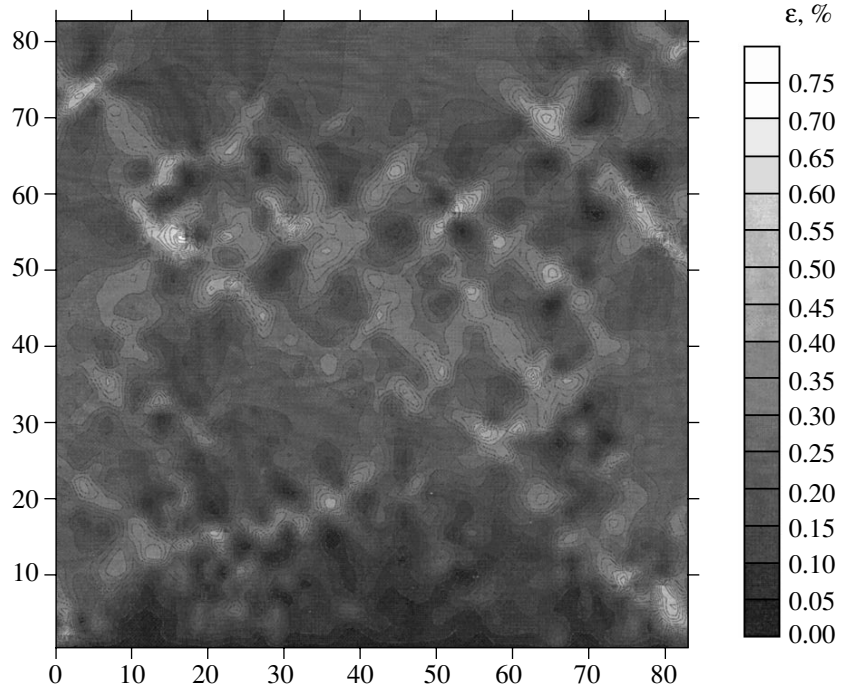

Fig. 1. The distribution of strain ε_x in a porous zirconia sample.

1063-7850/02/2807-0557$22.00 © 2002 MAIK "Nauka/Interperiodica"

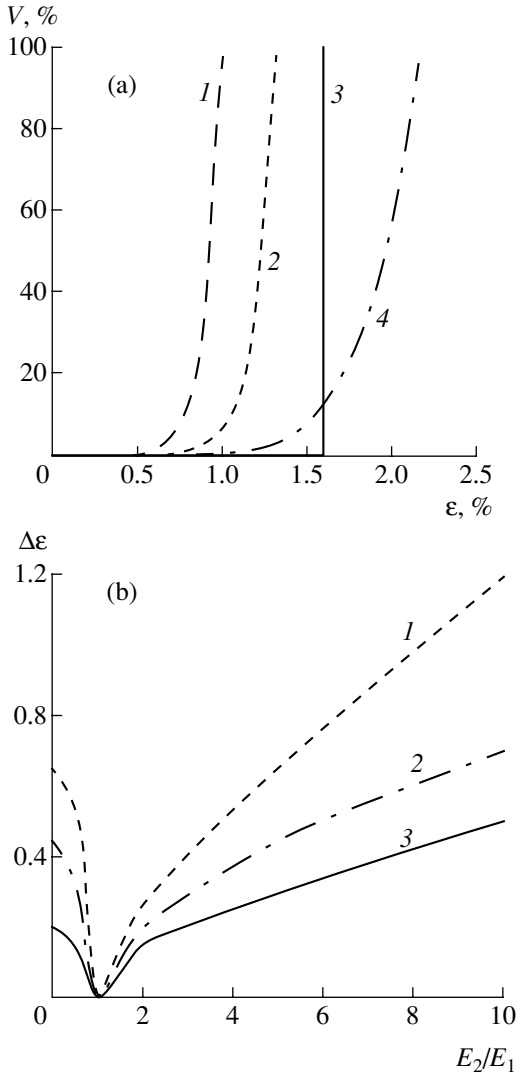

Fig. 2. (a) Plots of the fractured material volume versus total deformation for the (*1*) material with pores, (*2*) material with soft inclusions ($E_i = 0.5E_m$), (*3*) homogeneous material, and (*4*) material with hard inclusions ($E_i = 10E_m$); (b) plots of the (*1*) total deformation, (*2*) nonlinear straining, and (*3*) linear straining versus ratio of Young's moduli of the matrix and inclusion E_m and E_i, respectively.

imentally measured pore size distribution possesses a unimodal character, with an average pore size of 1.9 μm and a variance of $\sigma_d = 1.3$ μm.

The solution domain was composed of discrete triangular finite elements. Compression of the sample was modeled by displacement of the top boundary toward the bottom boundary. The magnitude of displacement was selected such that the arising stresses would exceed the ultimate strength of the material. The bottom boundary is fixed (translations and rotations in all directions are prohibited). The applied load varied with time according to a linear law. The initial parameters (Young's moduli and Poisson's ratios) were taken equal to the experimental values determined for a porous zirconia-based ceramic material [3]. Elements modeling the porous spaces possess zero Young's moduli and Poisson's ratios.

Figure 1 shows the pattern of strain distribution in porous zirconia for a total deformation of 1%. Isolated pores at large distances from each other are characterized by a uniform pattern of isolines. At the pore accumulation sites, the spacing of isolines decreases to reflect the strain localization effect. As can be seen, the regions of localized deformation (light areas) are oriented at 45° relative to the axis of loading and practically divide the sample into separate fragments with an average size close to the experimentally determined mean distance between pores. Indeed, assuming the system connectivity to be zero (isolated pores), the mean distance between pores (16.5 μm according to [4]) coincides with the measured value, thus confirming the adequacy of the model.

The distribution of stresses σ_y coincides with the distribution of elastic strain and exhibits localization at the sites of pore accumulation and along the lines parallel to the axis of loading (i.e., near the free side faces), which can lead to a barrel-like shape of the sample in a real experiment.

Study of the stress intensity distribution in porous zirconia showed evidence of the formation of stress concentrators in the vicinity of pores, which provide for a significant increase in the material strength for compression. Assuming the stress intensity σ_i to be constant, we can estimate the "degree of fracture" of a given material by calculating the volume fracture in which σ_i exceeds the experimentally determined strength level [3]. As can be seen from Fig. 2 (curve *1*) for porous zirconia, all stresses arising in a sample loaded up to 0.4% are below the ultimate strength level and, hence, the sample is not fractured. As the deformation grows further up to 0.85%, some regions in the material (where stresses exceed the ultimate strength) are fractured and the sample exhibits nonlinear accumulation of the fractured material volume. Subsequent accumulation of the microdamage proceeds by a linear law and, at a total deformation of 1%, stresses exceed the ultimate strength in the entire region modeled (which corresponds to complete fracture of the whole sample).

We have used the same scheme of calculations for an analysis of the behavior of a composite material with "soft" or "hard" inclusions instead of pores. The strength of the material of elements replacing pores was described by Young's moduli, the relative values of which with respect to the value for the matrix varied from zero (pores) to 10 (hard inclusions).

The distribution of stresses in a sample representing a matrix with the pores filled with the same material (absolutely compact sample) corresponds to the homogeneous case: up to a deformation of 1.59%, the material is uniformly strained and σ_i values over the entire modeled volume are below the ultimate strength for

compression (Fig. 2, curve *3*). The strain increment exceeds the ultimate strength by as low as 0.01%, whereby the material exhibits virtually instantaneous fracture.

A distribution of the isolines of straining in a material with hard inclusions is more uniform than that in a strained sample of porous zirconia. The isolines form closed circles around the inclusions, duplicating their shapes. No regularities are observed in the distribution of isolines in the regions far from the inclusions. Similar to the case of a porous material, the localization of strain in a filled composite takes place between inclusions and leads to fragmentation of the matrix. In order to calculate the proportion of fractured material, we set a level corresponding to the ultimate strength of a composite determined using the blend rule [5]. Similar to the case of a porous material, curves *2* and *4* can be divided into three regions, corresponding to the absence of fracture and the nonlinear and linear accumulation of the fractured material volume. The length of all three stages decreases in the materials with Young's moduli of the inclusions smaller as compared to the matrix value and increases with the strength of inclusions (Fig. 2b). A minimum value of the stage of accumulation of the fractured material volume is observed for a homogeneous sample.

In the case of loading structurally inhomogeneous materials, the samples contain localized deformation regions dividing the material into fragments with an average size equal to the mean distance between inhomogeneities. There are three stages of straining characterized by the (i) absence of local fracture, (ii) nonlinear accumulation of the volume of fractured material, and (iii) complete fracture.

REFERENCES

1. I. L. Dillamore, J. G. Roberts, and A. C. Bush, Met. Sci. **13** (2), 73 (1979).
2. Cosmos/M, Version 1.75 for Windows NT/95, Platforms 10/96, SN2008788770670.
3. S. P. Buyakova, Han Wei, Li Dunmy, *et al.*, Pis'ma Zh. Tekh. Fiz. **25** (17), 44 (1999) [Tech. Phys. Lett. **25**, 695 (1999)].
4. T. Werlefors and C. Eskilsson, Metallography **12**, 153 (1979).
5. *Physical Metal Science*, Ed. by O. V. Abramov and A. V. Serebryakov (Metallurgiya, Moscow, 1987), Vol. 2, p. 558.

Translated by P. Pozdeev

Technical Physics Letters, Vol. 28, No. 7, 2002, pp. 560–563. Translated from Pis'ma v Zhurnal Tekhnicheskoĭ Fiziki, Vol. 28, No. 13, 2002, pp. 57–66.

Bicoherent Wavelet Analysis of the Structure Formation in an Electron Beam with Virtual Cathode

A. E. Khramov[a,*], A. A. Koronovskiĭ[a], and Yu. I. Levin[b]

[a] *Saratov State University, Saratov, Russia*

[b] *State Scientific Center "College", Saratov, Russia*

* *e-mail: aeh@cas.ssu.runnet.ru*

Received December 10, 2001

Abstract—The supercritical electron beam structure formation in a diode gap with inhomogeneous ion background density are analyzed by the bicoherent wavelet transformation method. By studying the wavelet bicoherency of the spatiotemporal data about oscillations in the system, it is possible to effectively reveal and analyze local spatial structures formed in the electron beam. © *2002 MAIK "Nauka/Interperiodica".*

Study of the complicated chaotic behavior of distributed systems requires using special methods for analysis of the dynamics of coherent structures, since classical linear methods of analysis (for example, spectral) do not provide maximum information about processes taking place in nonlinear systems. Below we consider application of the bicoherent wavelet transformation, a nonlinear method originally proposed in [1], to an analysis of complicated processes in distributed systems.

Developed quite recently, the wavelet analysis offers a powerful method for studying the dynamics of distributed systems and draws increasing attention of researchers [2–4]. Using this method, it is possible to resolve the dynamics on various scale levels representing the structure of signals. The wavelet transform eliminates the need of expanding signals into harmonic series, which is the main disadvantage of the Fourier transformation applied to the analysis of turbulence and chaos because nonlinear equations describing such complicated phenomena in distributed systems possess no intrinsic harmonic modes.

Bisector (bicoherent) representation characterizes phase relationships (phase coupling) between various frequency components of a signal. We can speak of a phase coupling when the analyzed signal simultaneously contains two frequencies, ω_1 and ω_2, the sum (or difference) of which, as well as the sum of the corresponding phases ϕ_1 and ϕ_2, remain constant over a certain period of time. Using bicoherent wavelets, it is possible to reveal the intrinsic structure of spatial and temporal data, determined by the phase coupling, and study the time variation of this structure.

The mutual wavelet bispectrum (wavelet bicoherency) is defined as

$$B_{hg}(f_1, f_2) = \int_T W_h^*(f, \tau) W_g(f_1, \tau) W_g(f_2, \tau) d\tau, \quad (1)$$

where f, f_1, and f_2 are the frequencies obeying a relationship of the type $f = f_1 + f_2$; $h(t)$ and $g(t)$ are the analyzed signals; W_h and W_g are the corresponding wavelet spectra of these signals [2, 4]; T is the time interval for which the mutual wavelet bispectrum is analyzed; and the asterisk denotes a complex conjugate. The wavelet bispectrum is a measure of the phase coupling over the time interval T, which is manifested between components of the wavelet spectrum of the $g(t)$ signal on a time scale of $1/f_1$ and $1/f_2$ and the $h(t)$ signal on a time scale of $1/f$.

An important characteristic of the bicoherent wavelet transformation is the bicoherency sum, defined as

$$B_\Sigma(f) = \sqrt{\frac{1}{N_f}\sum (B_{hg}(f_1, f_2))^2}, \quad (2)$$

where summation is performed over all frequencies f_1 and f_2 obeying the condition $f = f_1 + f_2$; N_f is the number of terms in the sum. Also introduced is the total bicoherency, defined as

$$B = \sqrt{\frac{1}{N}\sum\sum (B_{hg}(f_1, f_2))^2}, \quad (3)$$

where the sum is taken over all analyzed frequencies f_1 and f_2, N being the total number of terms in this sum.

In this study, we apply the bicoherent wavelet transformation to analysis of the formation and interaction of coherent structures in an electron beam with a virtual cathode (VC) in a diode gap with an inhomogeneous ion

1063-7850/02/2807-0560$22.00

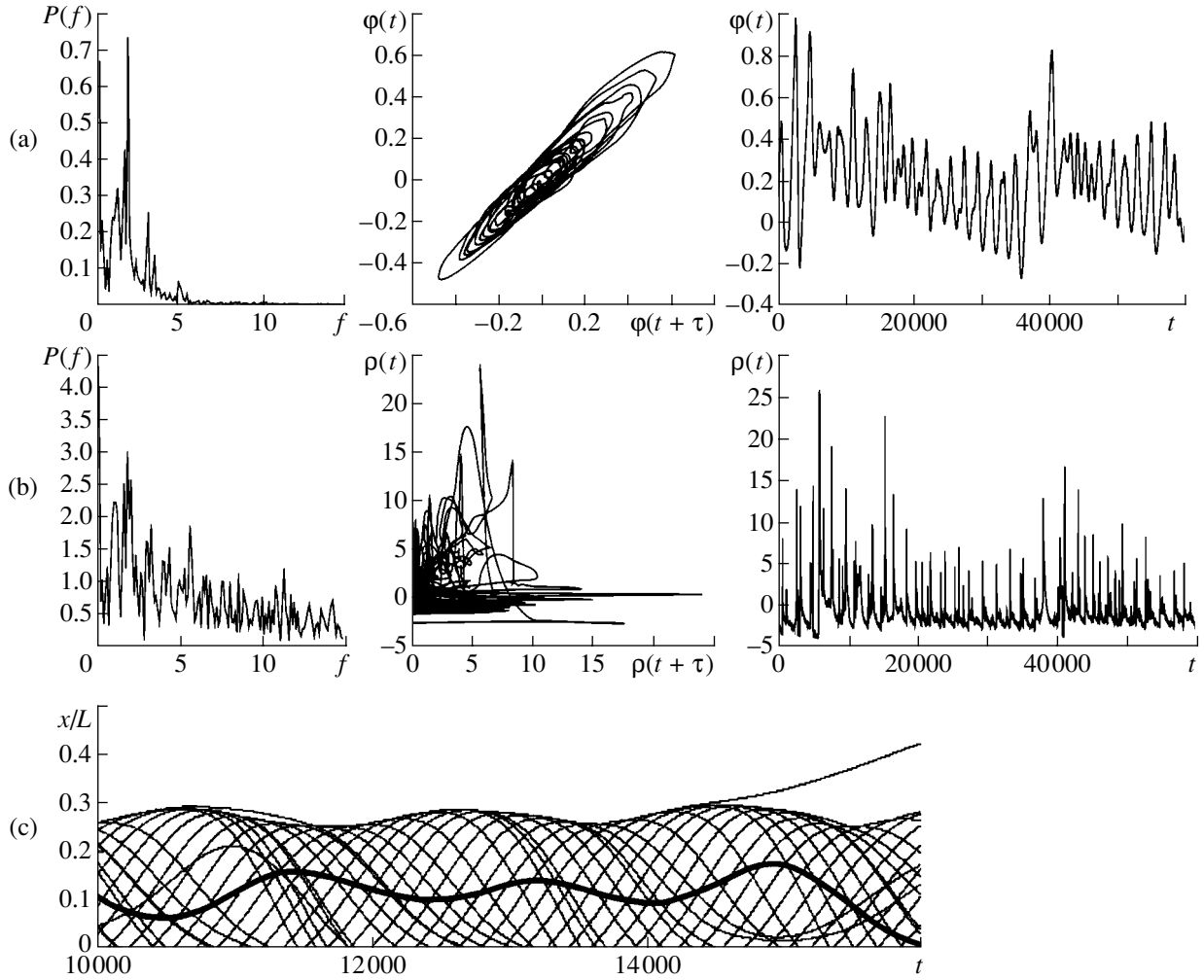

Fig. 1. The power spectra $P(f)$, phase portraits, and time patterns of (a) the electric field potential ϕ and(b) space charge density ρ in the diode gap section with a coordinate of $x = 0.25L$; (c) spatiotemporal pattern of the electron flow dynamics in the case studied (thick solid curve represents the trajectory of a particle trapped in a potential well).

background, which was studied in detail previously [5, 6]. This system offers the simplest model of a vircator with a plasma anode [7], which allows, under certain conditions, the VC generation frequency to be increased [5]. It was demonstrated [6] that the system exhibits a complicated chaotic dynamics of the electron beam.

The system under consideration represents a diode gap with a strongly inhomogeneous distribution of an immobile ion background in a region near the injection plane (anode plasma). The control quantities are the Pierce parameter $\alpha = \omega_p L/v_0$ (proportional to the beam current), the ratio $n = \rho_p/\rho_0$ of the anode plasma density ρ_p to the space charge density ρ_0 of the electron beam, and the coordinates x_{p1} (beginning) and x_{p2} (end) of the anode plasma layer; ω_p is the plasma frequency of the electron beam, L is the length of the interaction space, and v_0 is the unperturbed electron flow velocity. For $\alpha > \alpha_{cr}$, the single-stream state of the beam becomes unstable with respect to small perturbations in the charge density and the system features the VC formation [8]. Nonstationary processes in the system were analyzed by a numerical method of macroparticles [9, 10].

As was demonstrated previously [5, 6], the system under consideration exhibits a large set of dynamic regimes depending on the density n of the near-anode ion background and the beam current parameter α. When the ion density exceeds a certain critical value n_{cr} (depending on the Pierce parameter), the system exhibits a transition from regular and weakly stochastic VC oscillations via intermittency to developed chaotic oscillations with a base frequency significantly higher than that of the VC oscillations at $n < n_{cr}$. For a significantly inhomogeneous ion background with $n > 2.5$–3.5, the system is characterized by irregular oscillations with a continuous spectrum exhibiting no selected frequency components.

Below we consider a system with the following values of the control parameters: $\alpha = 2.125\pi$, $n = 4.0$, $x_{p1} = 0.05$, and $x_{p2} = 0.25$. A system with these charac-

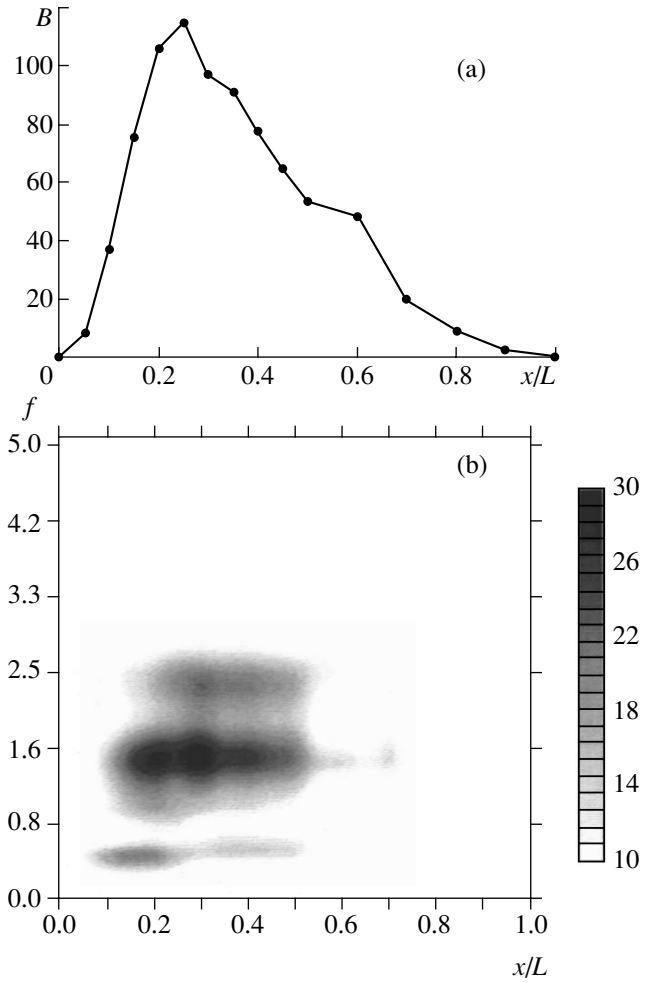

Fig. 2. (a) The plot of a total bicoherency B versus spatial coordinate x for the signals $h(t) = a\sin(2\pi f_0 t)$ and $g(t) = \varphi(t, x)$; (b) the projection of a bicoherent sum $B_\Sigma(x/L, f)$ constructed for the potential oscillations in various sections of the diode gap (different B_Σ values are represented by variable intensity of the projection color).

teristics exhibits a developed spatiotemporal pattern of chaotic oscillations. Figures 1a and 1b show the power spectra $P(f)$ (plotted in a nonlogarithmic scale), phase portraits (reconstructed using the Takens method [11]), and time variation of the electric field potential $\varphi(t)$ (Fig. 1a) and space charge density $\rho(t)$ (Fig. 1b) in the region of oscillating VC ($x/L = 0.25$). As can be seen, the temporal dynamics of the system is strongly irregular. The potential oscillations in the VC region show a more regular pattern as compared to that of the space charge density: the $\varphi(t)$ spectrum has a base frequency (f_0) and the phase portrait exhibits a structure related to the phase trajectory rotation with a time scale of $T \approx 1/f_0$. For this reason, we will use the $\varphi(t)$ oscillations for an analysis of processes in the system studied. It should be noted that the base frequency f_0 of the power spectrum is the same for oscillations in various diode cross sections.

Let us determine the total bicoherency (3) of data for the potential oscillations in vacuous diode sections x and a harmonic signal with a frequency corresponding to the base frequency f_0 of the power spectrum. This implies that we select signal h in relation (1) in the form of $a\sin 2\pi f_0 t$, while signal g represents the potential oscillations $\varphi(t, x)$. The calculations were performed using a base wavelet transformation of the Morlet type [12], which provides for a convenient interpretation of the results [4]. The results of calculations of the total bicoherency $B(x)$ as a function of the coordinate x are presented in Fig. 2a. As can be seen, the maximum total bicoherency (i.e., the maximum phase coupling between potential oscillations and the main time scale dynamics in the system) corresponds to the potential oscillations in the region of $x/L \approx 0.25$. This result implies that the basic spatiotemporal structure determining the main features in the behavior of the system is localized at $x/L \sim 0.25$.

Now let us calculate the bicoherency sum $B_\Sigma(f)$ according to (2) using the spatiotemporal data for the potential oscillations in the diode gap. The signal h is selected in the form of potential oscillations $\varphi(t, 0.25/L)$ in the region of maximum total bicoherency (Fig. 2a), and the signal g represents the potential oscillations $\varphi(t, x)$ in various sections of the diode gap. The results are presented in Fig. 2b in the form of a projection of the B_Σ surface onto the coordinate plane (x, f), where x is the diode section coordinate and f is the frequency for which the bicoherency sum is determined. Different values of the function of two variables $B_\Sigma(x, f)$ in Fig. 2b are represented by variable intensity of the projection color. As can be seen, the $B_\Sigma(x, f)$ surface contains two clearly distinguished regions where the wavelet bicoherency sharply increases. On the (x, f) plane, these regions are located in the vicinity of $x \sim 0.2$–0.4, $f \sim 1.6$ and $x \sim 0.1$–0.15, $f \sim 0.4$. The magnitude of bicoherency in the first of these regions is significantly greater than that in the second region. The two regions can be related to two coherent structures determining the electron beam dynamics in the system studied. Using the data obtained, it is possible to estimate the characteristic time scales and spatial localization of these structures.

In order to verify the results of the bicoherent wavelet analysis, we have studied physical processes in an electron beam (see also [6]). Figure 1c shows a spatiotemporal diagram of the electron beam dynamics under the condition studied, in which each curve represents a charged particle trajectory. The diagram extends over three characteristic periods of the VC oscillations, which corresponds to a time interval of $t \sim 3/f_0$. As can be seen, for large n values, the VC forms outside the ion layer and permanently exists in the flow. The minimum potential depth performs irregular oscillations at a base frequency f_0. At the same time, a potential well is formed between the injection plane and VC, with an extremum at $x \sim 0.1$. This well traps either particles

reflected from VC (and possessing small velocity on approaching the exit plane) or injected particles having lost the initial velocity in a strong retarding VC field. Trapped particles oscillating in the potential well are clearly distinguished in the spatiotemporal diagram (see Fig. 1c, where the trapped particle trajectory is depicted by a thick solid line). Thus, the beam features the formation of two electron bunches representing two self-sustained structures: the VC proper and a metastable structure comprised of long-lived particles occurring in the interaction space, trapped in the potential well between the injection plane and VC. The spatial localization and characteristic time scales of both structures coincide with those determined by methods of bicoherent wavelet transformation.

It should be noted that the spatiotemporal dynamics of the system studied is similar to the flow dynamics in a generator with a VC of the triode type [7, 13, 14], which also exhibits a two-humped potential profile. The flow features a self-sustained vortex structure of trapped particles. The interaction between the VC and this vortex gives rise to complicated flow dynamics analogous to that described in [15].

Thus, the chaotic dynamics and structure formation in an electron beam with a VC in a diode with a strongly inhomogeneous ion background were analyzed by the bicoherent wavelet transformation method. Using this method for analysis of spatiotemporal data, it is possible to effectively reveal coherent structures determining the dynamics of systems featuring developed spatial chaos.

Acknowledgments. This study was supported by the Russian Foundation for Basic Research, project no. 01-02-17392.

REFERENCES

1. B. Ph. van Milligen, E. Sánchez, T. Estrada, *et al.*, Phys. Plasmas **2** (8), 3017 (1995).
2. N. M. Astaf'eva, Usp. Fiz. Nauk **166** (11), 1145 (1996) [Phys. Usp. **39**, 1085 (1996)].
3. *Wavelets in Physics*, Ed. by J. C. van den Berg (Cambridge Univ. Press, Cambridge, 1998).
4. V. G. Anfinogentov, A. A. Koronovskiĭ, and A. E. Khramov, Izv. Akad. Nauk, Ser. Fiz. **64** (12), 2383 (2000).
5. V. G. Anfinogentov and A. E. Khramov, Pis'ma Zh. Tekh. Fiz. **24** (21), 74 (1998) [Tech. Phys. Lett. **24**, 860 (1998)].
6. V. G. Anfinogentov and A. E. Khramov, Izv. Akad. Nauk, Ser. Fiz. **62** (12), 2428 (1998).
7. V. D. Selemir, B. V. Alekhin, V. E. Vatrunin, *et al.*, Fiz. Plazmy **20** (8), 689 (1994) [Plasma Phys. Rep. **20**, 621 (1994)].
8. *High Power Microwave Sources*, Ed. by V. L. Granatstein and I. Alexeff (Artech House, Boston, 1987), Chap. 13.
9. C. K. Bridsall and A. B. Langdon, *Plasma Physics via Computer Simulation* (McGraw-Hill, New York, 1985).
10. A. M. Afonin, A. N. Didenko, A. F. Pautkin, and A. S. Roshal', Radiotekh. Élektron. (Moscow) **37** (10), 1889 (1992).
11. F. Takens, in *Lectures Notes in Mathematics, Warwick 1980*, Ed. by D. Rand and L.-S. Young (Springer-Verlag, New York, 1981), p. 366.
12. A. Grossmann and J. Mortel, SIAM J. Math. Anal. **15**, 723 (1984).
13. V. P. Grigor'ev, A. G. Zherlitsyn, and T. V. Koval', Fiz. Plazmy **16**, 1353 (1990) [Sov. J. Plasma Phys. **16**, 784 (1990)].
14. A. P. Privezentsev and G. P. Fomenko, Izv. Vyssh. Uchebn. Zaved., Ser. Prikl. Nelineĭnaya Din. **2** (5), 56 (1994).
15. V. G. Anfinogentov and A. E. Khramov, Izv. Vyssh. Uchebn. Zaved., Ser. Prikl. Nelineĭnaya Din. **6** (1), 93 (1998).

Translated by P. Pozdeev

Technical Physics Letters, Vol. 28, No. 7, 2002, pp. 564–567. Translated from Pis'ma v Zhurnal Tekhnicheskoĭ Fiziki, Vol. 28, No. 13, 2002, pp. 67–73.

A Method for Determining the States of Gas Molecules and Radicals Participating in Heterogeneous Chemical Reactions

V. F. Kharlamov, T. S. Rogozhina, A. V. Barmin, I. A. Makushev, and M. I. Bykovskiĭ

Orel State Technical University, Orel, Russia

e-mail: khar@ostu.ru

Received January 23, 2002

Abstract—A new method is proposed for monitoring the participation of free, preadsorbed, and chemisorbed gas species in chemical reactions at a solid–gas interface. The phenomena of energy exchange in the layer of adsorbed radicals, leading to an increase in the rate of heterogeneous recombination processes, were observed.

The main results concerning the mechanisms of heterogeneous chemical reactions were obtained using small flows of gas molecules participating in reactions on the surface of solids under high-vacuum experimental conditions. Methodological problems encountered in the study of the mechanisms of heterogeneous reactions at "high" pressures of gas-phase molecules reacting on a catalyst surface (technical catalysis conditions) are related to the fact that use of the most informative relaxation techniques is hindered because of short characteristic relaxation times of kinetic processes in the systems studied. Moreover, the kinetic data obtained under these conditions cannot be unambiguously interpreted because of a change in the state of the solid surface as a result of uncontrolled surface processes (e.g., diffusion of gas molecules into bulk, etc.), the role of which significantly increases with the gas phase pressure. In order to eliminate this uncertainty, it is necessary to monitor the state of species participating in the chemical transformations. However, methods of such monitoring have still not been developed.

Below we describe an approach to solving the above problem. Consider a gas mixture continuously passing through a flow reactor and participating in a heterogeneous reaction on the surface of a catalyst under stationary conditions. Let us periodically introduce additional portions (packets) of substances reacting on the solid surface into a carrier gas pumped through the reactor. The time τ required for each packet of active molecules to travel through the reactor is selected so as to provide that these molecules would not significantly affect the state of the catalyst surface. Under these conditions, we can gain unambiguous information concerning the states of gas molecules participating in the heterogeneous chemical reactions by studying the amplitude of pulsations in the reaction rate as a function of the density of active molecules in the packet and the concentration of molecules chemisorbed on the solid surface.

As an example, we have studied a heterogeneous recombination of radicals. For this purpose, we simultaneously monitored the kinetics of the concentration of adsorbed radicals $N(t)$, the dynamic reaction response (DRR) $F(t) = GJ(t)$ [1], and the intensity of the radical recombination induced luminescence (RRL) $I(t) = \eta J(t)$ [2]. Here, t is the current time, G and η are coefficients, and $J(t)$ is the reaction rate. In the experiment, a gas (hydrogen containing no more than 5×10^{-3}% impurities) at a pressure of $P = 50$ Pa was continuously passed through a flow reactor containing a metal sample. Two identical RF generators induced gas discharges in the discharge tubes connected to the reactor. Each discharge was either stationary, pulsed, or combined (stationary-pulsed). The discharge pulses had a duration of 1s and a repetition rate of 0.02 or 0.04 s^{-1}. The pulsed discharge periodically increased the concentration of atoms n in the gas phase by Δn, thus creating the packets of atoms. The pulses were screened and were independent of each other. In the course of diffusion from a discharge tube to reactor, the excited particles relaxed, experiencing ~10^4 collisions in the gas phase. Therefore, only gas particles in the ground electronic and vibrationally-excited states entered the reactor.

The concentrations of H atoms supplied (with a stationary flow and in the form of packets) to the reactor were determined and expressed in relative units using a method [3] based on the intensity of the stationary and pulsed emission corresponding to the blue (λ_1 = 487 nm) and red (λ_2 = 656 nm) lines of hydrogen in the discharge plasma: $n = B_1 I_g$; $\Delta n = B_2 \Delta I_g$, where B_1 and B_2 are coefficients and I_g and ΔI_g are the steady-state and flash intensity of the hydrogen emission line. The required line in the emission spectrum of hydrogen was

separated with the aid of a UM-2 monochromator. The absolute values of n determined by the thermal probe technique obeyed the condition $n \le 7 \times 10^{13}$ cm^{-3}. In the experiment, the n and Δn values were varied by changing in a stepwise manner the power of stationary or pulsed discharge; the new values were measured after establishing the modified stationary values.

The concentrations of adsorbed radicals N were determined using a resonance piezoquartz balance technique with a sensitivity of 1×10^{-10} g. The piezocrystal transducer with the radicals adsorbed on both surfaces was mounted near a balance pan containing the same substance used for the DRR measurements [4]. The kinetic curves of $N(t)$, $F(t)$, and $I(t)$ were measured after a 10-min pause in the radical source operation. The catalyst was either an ultradisperse copper powder composed of spherical particles with an average diameter of 100 nm or a finely dispersed ZnS–Cu phosphor with a specific surface of ~1 m^2/g. The experimental techniques were described in more detail elsewhere [4, 5].

The study of interaction of the flow of H atoms with the copper surface revealed the following trends. Under stationary flow conditions, an increase in the concentration of hydrogen atoms in the gas phase was accompanied by a monotonic synchronous growth in both the concentration $N^*(n)$ of chemisorbed atoms and the DRR value $F^*(n)$. The $F^*(N^*)$ relationship was close to a linear dependence of the type $F^* \approx kN^*$, where k is a coefficient and the asterisk denotes stationary values of the physical variables. The shape of these curves does not change after switching on the pulsed source generating periodic packets of hydrogen atoms. When a packet of radicals passes through the reactor, the $N(t)$ and $F(t)$ curves exhibit peaks with a base duration of 3 s (Fig. 1, inset). After switching on the stationary discharge, the amplitude of periodic DRR pulses $F_m = F(n + \Delta n)$ first increases and then remains unchanged (curve *1*), irrespective of the concentration N of chemisorbed hydrogen atoms (which increases with time as depicted by curve *2*).

After switching off the stationary discharge, the amplitude F_m acquires the previous value and hydrogen atoms are desorbed from the catalyst surface. The shape of the (continuous) kinetic curve $F(t)$ observed after switching on the stationary discharge depends on the hydrogen concentration n in the gas phase: for $n < 2 \times 10^{13}$ cm^{-3}, the $F(t)$ curve exhibits a region where the DRR increases synchronously with the concentration of chemisorbed atoms (Fig. 1, curve *3*); for $n > 2 \times 10^{13}$ cm^{-3}, the $F(t)$ curve acquires a rectangular shape. At a fixed concentration Δn of atoms in the packets, an increase in the stationary concentration n (responsible for the change in N) does not lead to an increase of the DRR increments $\Delta F = F(n + \Delta n) - F(n)$ in the pulses; the ΔF values are also independent of the concentration N of chemisorbed hydrogen. At a constant stationary

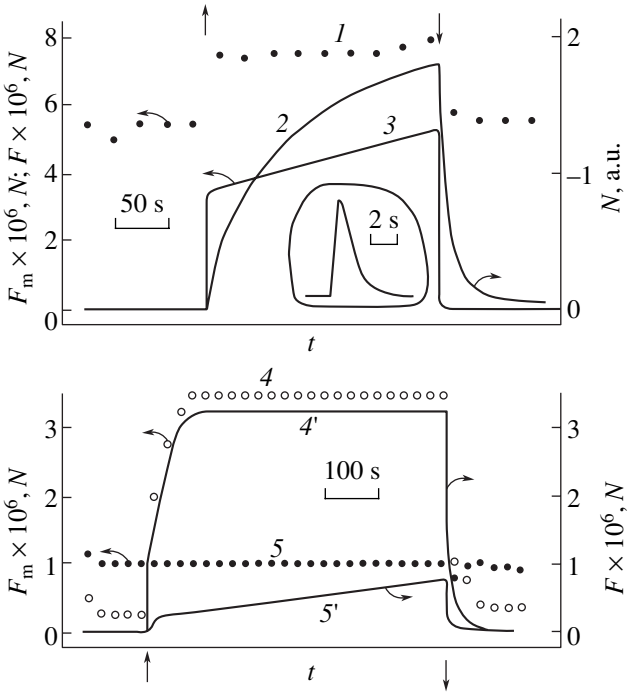

Fig. 1. Time variation of the quantities F_m (*1*, *4*, *5*), F (*3*, *4*', *5*'), and N (*2*) for hydrogen "packets" interacting with the surface of copper (*1*, *2*, *3*) and zinc sulfide (*4*, *4*', *5*, *5*') before and after switching the stationary flow of H atoms on (↑) and off (↓) at T = 293 K: (*1*, *2*, *3*) $n = 1 \times 10^{13}$ cm^{-3}, $n^{-1}\Delta n = 3$; (*4*, *4*') $n = 7 \times 10^{13}$ cm^{-3}, $n^{-1}\Delta n = 0.2$; (*5*, *5*') $n = 6 \times 10^{12}$ cm^{-3}, $n^{-1}\Delta n = 6$. The inset shows the shape of a DRR pulse.

concentration n (and N), the ΔF value increases with the concentration Δn. Analogous relationships were established for hydrogen atoms in the packets interacting with the ZnS–Cu phosphor (Fig. 1, curves *4*, *4*', *5*, and *5*').

Let us assume that chemical transformations involving chemisorbed atoms are described by the reactions

$$R + (RZ) \longrightarrow R_2 + Z,$$

$$2(RZ) \longrightarrow R_2 + 2Z,$$

$$RZ + (RZ) \longrightarrow R_2 + 2Z,$$

where Z is an adsorption center, (RZ) is a chemisorbed atom, and RZ is an atom trapped in the precursor state [6]. If these processes were significantly contributing to the reaction rate J, the relaxation time for the surface filled with chemisorbed atoms upon switching of the stationary source of free atoms could be estimated as $\tau_R < N_0 J^{-1} = N_0(0.25 n v \gamma)^{-1} = 10^{-4}$–$10^{-2}$ s [7], where N_0 is the concentration of the adsorption centers, v is the average velocity of the thermal motion of free hydrogen atoms, and γ is the heterogeneous recombination coefficient for hydrogen. However, the experimentally observed values of τ_R exceed this estimate by 3–5 orders

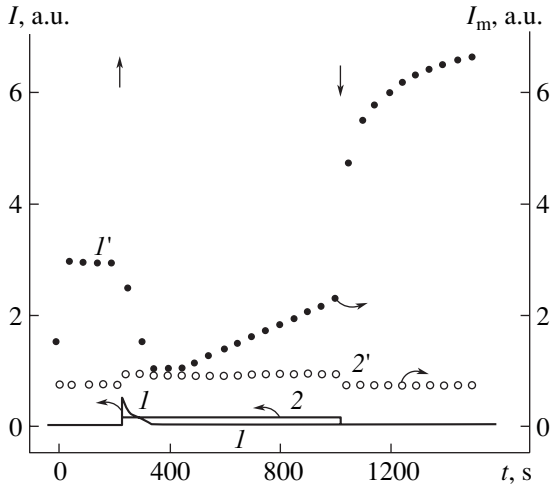

Fig. 2. Time variation of (*1'*, *2'*) the intensity of emission from ZnS–Cu phosphor for the "packets" of CO and O radicals interacting with the catalyst surface and (*1*, *2*) the stationary emission intensity before and after switching the stationary flow of CO and O radicals on (↑) and off (↓) for $n^{-1}\Delta n = 6$ and $T = 293$ (*1*, *1'*) and 390 K (*2*, *2'*).

of magnitude (Fig. 1, curve *2*), which indicates that the above assumption is incorrect.

Then, let us consider the following model reactions,

$$R + Z \underset{k_1'}{\overset{k_1}{\rightleftharpoons}} RZ; \quad R + Z \underset{k_2'}{\overset{k_2}{\rightleftharpoons}} (RZ);$$
$$2RZ \xrightarrow{k_3} R_2 + 2Z; \quad 2(RZ) \xrightarrow{k_4} R_2 + 2Z,$$

and the corresponding kinetic equations,

$$\dot{N}_1 = k_1(N_0 - N) - k_1'N_1 - 2k_3N_1^2;$$
$$\dot{N} = k_2(N_0 - N) - k_2'N - 2k_4N^2,$$

where N_1 is the concentration of atoms in the precursor state, k_1–k_4 are the reaction rate constants, $k_1 = 0.25n\nu\sigma$, and σ is the cross section for trapping free radicals in the precursor state. Let us assume that atoms in the precursor and chemisorbed states form two subsystems—"fast" and "slow," respectively. Using the adiabatic approximation, we obtain $J \cong k_3N_1^2$ and

$$J \approx k_3k_1^2(N_0 - N)^2(k_1')^{-2}, \; 8k_1k_3(N_0 - N) \ll (k_1')^2; \quad (1)$$

$$J \approx 0.5k_1(N_0 - N), \quad 8k_1k_3(N_0 - N) \gg (k_1')^2. \quad (2)$$

Under stationary condition ($\dot{N}_1 = \dot{N} = 0$), the reaction rate is

$$J^* = 0.5k_1k_2^{-1}k_2'N^* + (1 + k_1k_2^{-1})k_4(N^*)^2 - 0.5k_1'N_1^*.$$

For relatively small values of k_4 and k_1', this yields (in agreement with experiment) $J^* \approx kN^*$, where k is a coefficient. For $N \ll N_0$, expression (2) describes the experimental behavior of $F_m(t) = GJ_m(t)$ and $F(t) = GJ(t)$, corresponding to a "large" concentration of atoms in the gas phase (Fig. 1, curves *1*, *4*, *4'*, *5*). Under stationary conditions, the linear dependence of the reaction rate on the concentration of gaseous hydrogen is related to the fact that the recombination process $2RZ \longrightarrow R_2 + 2Z$ is limited by the trapping of H atoms in the precursor state RZ : $J \cong 0.5k_1N_0$. Expression (1) corresponds to the $F(t)$ curves obtained in the case of small n (Fig. 1, curves *3* and *5'*).

The constant values of F_m observed after switching on the stationary discharge (curves *1* and *5*) indicate that the ascending portion of $F(t)$ (curves *3* and *5'*) is not related to uncontrolled variation of the state of the surface with time. Therefore, this growth probably reflects a contribution of the chemisorbed atoms to stabilization of the recombined molecules due to energy exchange in the layer of adsorbed radicals:

$$2RZ + (RZ) \longrightarrow R_2 + 2Z + (RZ).$$

Some experiments were conducted with carbon dioxide of spectroscopic grade. In the case of a heterogeneous reaction $CO + O \longrightarrow CO_2$ proceeding on the surface of the ZnS–Cu phosphor at $T = 295$ K, the RRL kinetics is affected by a significant (and, under these conditions, partly irreversible) chemisorption of radicals. When both stationary and pulsed sources of radicals are operating ($n^{-1}\Delta n = 6$), the system obeys the conditions $I_mI^{-1} > 10^2$ and $I_mI^{-1} \gg n^{-1}\Delta n + N^{-2}(\Delta n)^2$, where $I_m = I(n + \Delta n)$ is the RRL peak amplitude and $\Delta N = N(n + \Delta n) - N(n)$ (Fig. 2, curves *1* and *1'*). Under the same flow conditions at a higher temperature ($T =$ 390 K), the concentration of chemisorbed radicals sharply drops. This leads to a decrease in I_m and a significant increase in the I_mI^{-1} ratio (Fig. 2, curves *2* and *2'*). These results cannot be explained by the participation of chemisorbed radicals in the heterogeneous reaction.

Let us consider a model in which the reaction rate is determined by the recombination of precursor radicals. Curves *2* and *2'* in Fig. 2 obey the condition $I_mI^{-1} \approx n_mn^{-1}$, which corresponds to $J = I\eta^{-1} \approx 0.5k_1\dot{N}_0$. This is the maximum possible value of the reaction rate, which grows with decreasing temperature under otherwise equal conditions (cf. curves *1'* and *2'*) only due to an increase in the cross section σ for the free radical trapping in the precursor state. The effect, related to an increase in the surface coverage by chemisorbed radicals with decreasing temperature, is caused by the participation of chemisorbed radicals in the removal of excess energy and stabilization of radicals in the pre-

cursor state on the catalyst surface according to the reaction

$$R + Z + (RZ) \longrightarrow RZ + (RZ).$$

Acknowledgments. This study was supported by the Russian Foundation for Basic Research, project no. 99-03-32097.

REFERENCES

1. V. F. Kharlamov, Poverkhnost, No. 11, 122 (1993).
2. F. F. Vol'kenshteĭn, A. N. Gorban', and V. A. Sokolov, *Radical Recombination Luminescence of Semiconductors* (Nauka, Moscow, 1976).
3. V. V. Zaĭtsev, Opt. Spektrosk. **72** (4), 859 (1992) [Opt. Spectrosc. **72**, 462 (1992)].
4. K. M. Anufriev, V. F. Kharlamov, and A. V. Razumov, Prib. Tekh. Éksp., No. 1, 152 (2000).
5. V. F. Kharlamov, L. Yu. Frolenkova, and T. S. Rogozhina, Zh. Tekh. Fiz. **71** (10), 90 (2001) [Tech. Phys. **46**, 1294 (2001)].
6. O. V. Krylov and B. R. Shub, *Nonequilibrium Processes in Catalysis* (Khimiya, Moscow, 1990).
7. V. F. Kharlamov, Khim. Fiz. **13** (6), 83 (1994).

Translated by P. Pozdeev

Technical Physics Letters, Vol. 28, No. 7, 2002, pp. 568–571. Translated from Pis'ma v Zhurnal Tekhnicheskoĭ Fiziki, Vol. 28, No. 13, 2002, pp. 74–82.

The Giant Dispersion of Critical Currents in a Superconductor with Fractal Clusters of a Normal Phase

Yu. I. Kuzmin

Ioffe Physicotechnical Institute, Russian Academy of Sciences, St. Petersburg, 194021 Russia
e-mail: yurk.shuv@pop.ioffe.rssi.ru; iourk@mail.ru

Received February 19, 2002

Abstract—The influence of fractal clusters of a normal phase on the dynamics of a magnetic flux trapped in a percolation superconductor is considered. The critical depinning current distribution and the current–voltage characteristics of fractal superconducting structures in the resistive state are determined for an arbitrary fractal dimension of the cluster boundaries. The interval of fractal dimensions is found in which the dispersion of critical currents exhibits unlimited growth. It is established that the fractality of clusters favors a decrease of the electric field arising during the magnetic flux motion, thus increasing the critical current value. The region featuring the giant dispersion of critical currents can be expected to provide for the maximum current-carrying capacity of a superconductor. *© 2002 MAIK "Nauka/Interperiodica".*

One way to increase the critical currents of superconductors is to create artificial pinning centers in the volume of the material. The role of such centers can be performed by the clusters of a normal phase formed in the course of the film growth at the sites of defects at the film–substrate interface [1–3]. New possibilities for the pinning enhancement are opened by clusters of the normal phase possessing fractal boundaries [4–7] (see also references in [7]). Below we will consider the influence of such fractal clusters on the critical currents and current–voltage characteristics of superconductors in the resistive state.

Formulation of the problem is analogous to that considered in [6, 7]. A superconductor containing columnar inclusions of a normal phase is cooled in a magnetic field below the critical temperature (field-cooling regime). As a result, the magnetic flux is trapped in isolated clusters of the normal phase. Then a transport current is passed through the sample in the direction perpendicular to the magnetic field. It is assumed that a superconducting percolation cluster is formed in the plane of the electric current passage. While the transport current increases, the trapped flux remains unchanged until the vortices begin to separate from the clusters in which the pinning force is smaller than the Lorentz force created by the current. The vortices travel through the superconducting space via weak links between clusters of the normal phase. The weak links are readily formed at various structural defects in high-temperature superconductors characterized by a small correlation length. In usual low-temperature superconductors, weak links can form as a result of the proximity effect at the sites of minimum distance between neighboring normal phase clusters.

Thus, irrespective of their nature, the weak links form channels for the transport of vortices. According to the vortex configuration, each cluster of the normal phase contributes to the total distribution of the depinning critical currents. A geometric probability analysis of the influence of distribution of the points of vortex entrance into weak links on the critical currents of clusters was performed in [7]. As the transport current increases, the vortices break away first from the clusters of a smaller pinning force and, accordingly, of a lower critical current. Therefore, a change in the trapped magnetic flux $\Delta\Phi$ is proportional to the number of normal phase clusters possessing critical currents below a preset value of I. For this reason, a relative flux decrease is equal to the probability that a critical current I' of an arbitrarily selected cluster is smaller than I:

$$\frac{\Delta\Phi}{\Phi} = \int_0^I f(I')dI', \qquad (1)$$

where $f(I)$ is the probability density for the distribution of the critical depinning currents.

At the same time, the magnetic flux trapped in a cluster is proportional to the cluster area A. Therefore, a change in the total trapped flux depends on the distribution of areas of the normal phase clusters. Thus, in order to determine how the transport current influences the trapped magnetic flux, it is necessary to find a relationship between distributions of the critical currents of clusters and their areas. This problem was solved in [8]

1063-7850/02/2807-0568$22.00

for the general case of the gamma-distribution of areas of clusters with fractal boundaries:

$$w(a) = \frac{(g+1)^{g+1}}{\Gamma(g+1)} a^g \exp[-(g+1)a], \qquad (2)$$

where $w(a)$ is probability density for the cluster area distribution function, $a \equiv A/\bar{A}$ is the dimensionless area of a cluster, $\bar{A}$ is the average cluster area, $g > -1$ is the gamma-distribution parameter determining the standard deviation of the cluster area ($\sigma_a = 1/\sqrt{g+1}$), and $\Gamma(\nu)$ is the Euler gamma-function. In this case, the distribution of critical currents is as follows:

$$f(i) = \frac{2G^{g+1}}{D\Gamma(g+1)} i^{-\frac{2}{D}(g+1)-1} \exp\left(-Gi^{-\frac{2}{D}}\right), \qquad (3)$$

where

$$G \equiv \frac{\theta^{\frac{2}{D}(g+1)+1}}{\left[\theta^{g+1} - \frac{D}{2}\exp(\theta)\Gamma(g+1,\theta)\right]^{\frac{2}{D}}}, \quad \theta \equiv \frac{D}{2} + g + 1,$$

$\Gamma(\nu, z)$ is the complementary incomplete gamma-function, $i \equiv I/I_c$ is the dimensionless electric current, $I_c = \alpha[(g+1)/(G\bar{A})]^{D/2}$ is the critical current of the transition into the resistive state, α is the form factor, and D is the fractal dimension of the cluster boundary. The fractal dimension determines the scaling relation between perimeter and area:

$$P^{1/D} \propto A^{1/2}, \qquad (4)$$

where P is the perimeter of a cluster with area A. Relation (4) is consistent with the generalized Euclidean theorem according to which the ratios of the corresponding geometric measures are equal when reduced to the same dimension [9].

In the particular case of $g = 0$, the gamma-distribution (2) reduces to exponential, $w(a) = \exp(-a)$, for which $\bar{a} = \sigma_a = 1$. This distribution of areas of the normal phase clusters with fractal boundaries, realized in YBCO-based film structures, was considered in detail elsewhere [6, 7].

The found critical current distribution function (3) provides for an adequate description of the effect of a transport current on the trapped magnetic flux. Using this function, the density n of vortices broken away from the pinning centers by the current i can be determined from relation (1):

$$n(i) = \frac{B}{\Phi_0}\int_0^i f(i')di' = \frac{B}{\Phi_0}\frac{\Gamma(g+1, Gi^{-2/D})}{\Gamma(g+1)}, \qquad (5)$$

where B is the magnetic field, $\Phi_0 \equiv hc/(2e)$ is the magnetic flux quantum, h is the Planck constant, c is the speed of light, and e is the electron charge. The integral in the right-hand part of (5) is the accumulated probability function, which is a measure of the number of clusters with the critical current not exceeding the preset value of i.

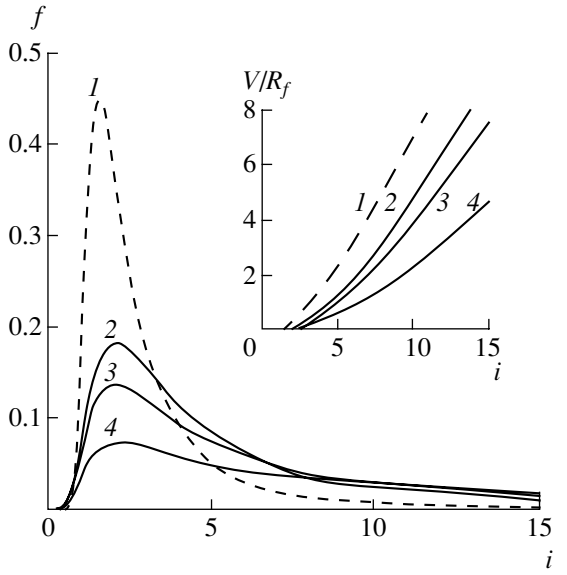

Fig. 1. Effect of the fractal dimension D and the gamma-distribution parameter g on the distribution of critical currents. Dashed curves refer to the Euclidean clusters ($D = 1$) and solid curves, to the clusters with most fractal boundaries ($D = 2$): (*1*) $D = 1$, $g = 0$; (*2*) $D = 2$, $g = 0.5$; (*3*) $D = 2$, $g = 0$; (*4*) $D = 2$, $g = -0.5$. The inset shows the corresponding current–voltage characteristics.

Figure 1 shows how the fractal dimension of cluster boundaries influences the critical current distribution. A comparison between curves *1* and *3* shows that an increase in the fractal dimension leads to a significant extension of the "tail" of the $f = f(i)$ distribution. This effect is more pronounced for smaller values on the gamma-distribution parameter g.

In the interval of currents $i > 1$, the magnetic flux motion leads to the appearance of an electric voltage across the sample, which passes into the resistive state. Because of the finite resistance, the current passage is accompanied by the energy dissipation. Similarly to any hard superconductor (type II superconductor with pinning centers), the presence of dissipation in the resistive state does not necessarily imply breakage of the phase coherence. The superconducting state collapses only when the dissipation exhibits an avalanche growth due to the thermomagnetic instability development.

In the resistive state, the superconductor is adequately described by the current–voltage characteristic. Using the fractal distribution of critical currents (3), it is possible to determine the electric field arising from the magnetic flux motion after the vortices have been broken away from the pinning centers. Since each cluster of the normal phase contributes to the overall distribution of critical current, the voltage across the superconductor $V = V(i)$ is an integral response to the sum of

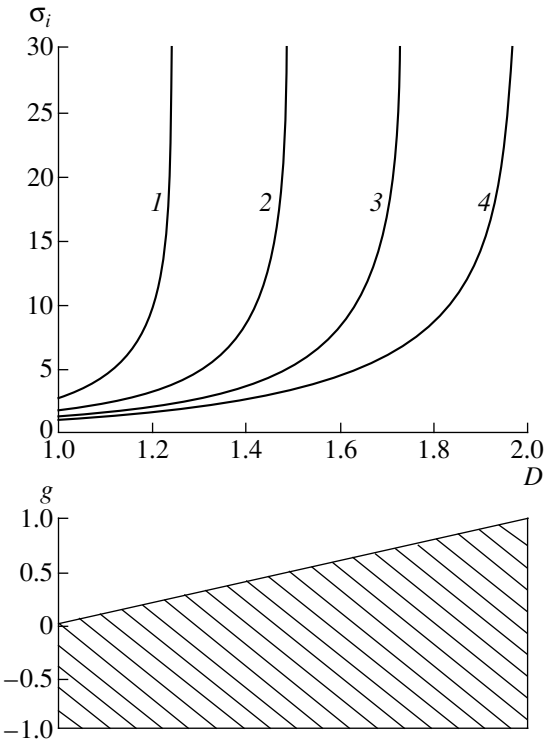

Fig. 2. Plots of the rms deviation of critical currents versus fractal dimension of the normal phase clusters for various values of the gamma-distribution parameter g = 0.25 (*1*), 0.5 (*2*), 0.75 (*3*), and 1 (*4*). The cross-hatched area corresponds to the region of giant dispersion of the critical current for $D \geq g + 1$.

contributions from all clusters:

$$V = R_f \int_0^i (i - i') f(i') di', \tag{6}$$

where R_f is the flux flow resistance. This representation of the voltage across the sample is frequently employed in the description of pinning of the vortex filament bundles in superconductors [10] and in the analysis of critical scaling of the current–voltage characteristics [1] (that is, in all cases when there is a distribution of the critical depinning currents). Below we will concentrate on the conclusions following from the properties of fractal distribution (3) and will not consider the questions related to the possible dependence of the flux flow resistance R_f on the transport current.

After substituting distribution function (3) into convolution integral (6) and performing integration, we eventually obtain an expression for the voltage across the sample:

$$\frac{V}{R_f} = \frac{1}{\Gamma(g+1)} \times \left[i\Gamma\left(g+1, Gi^{-\frac{2}{D}}\right) - G^{\frac{D}{2}}\Gamma\left(g+1-\frac{D}{2}, Gi^{-\frac{2}{D}}\right)\right]. \tag{7}$$

The inset in Fig. 1 shows the current–voltage characteristics calculated by formula (7) for a superconductor with fractal clusters of the normal phase. It should be noted that analogous current–voltage characteristics were observed in a fractal dissipation regime in the experiments devoted to determination of the dynamic resistance of BPSCCO composites containing silver inclusions [5]. A significant drop in the voltage across a sample for all fractal dimensions is observed beginning with the transport current i = 1, which coincides with the current of the transition into the resistive state determined in [6] from the accumulated probability function of the critical current distribution. For smaller currents, the trapped flux remains virtually unchanged because there are no centers with such a small depinning current.

As can be seen from the inset in Fig. 1, the fractality of clusters significantly reduces the electric field arising from the magnetic flux motion in a superconductor, the effect increasing with a decrease in parameter g. This is explained by features of the exponential-hyperbolic distribution (3). An increase in the fractal dimension leads to expansion of the critical current distribution toward greater values of the current. At the same time, the total area under the curve $f = f(i)$ remains unchanged because the probability function (3) is normalized to unity in the whole interval of possible positive critical currents. This implies that an increasing number of clusters capable of effectively trapping the magnetic flux are involved in the process under consideration. For this reason, the number of vortices broken away from the pinning centers by the Lorentz force tends to decrease, a smaller proportion of the magnetic flux can move and, hence, an electric field of lower strength is generated. The lower the electric field, the smaller the energy dissipated as a result of the transport current passage; a decrease in the heat liberation (which can induce the transition into the normal state) leads to an increase in the critical current for a superconductor containing such fractal clusters. The maximum current-carrying capacity is achieved upon decreasing the parameter g. In this case, the clusters of small size, which possess maximum critical currents, produce a maximum contribution to the resulting distribution.

This probability redistribution resulting from a change in the fractal dimension is characterized by the variance of critical currents and expressed by the rms deviation

$$\sigma_i = G^{\frac{D}{2}} \sqrt{\frac{\Gamma(g+1-D)}{\Gamma(g+1)} - \left[\frac{\Gamma(g+1-D/2)}{\Gamma(g+1)}\right]^2}.$$

Dependence of the critical current rms deviation on the fractal dimension exhibits a pronounced superlinear character (Fig. 2). For $g < 1$, there exists an interval of $D \geq g + 1$ in which the dispersion of critical currents exhibits infinite growth. This giant dispersion region is indicated by cross-hatching in Fig. 2. Distributions with

infinite variance are known in the theory of probability, a classical example being offered by the Cauchy distribution [12]. However, this behavior of the exponential-hyperbolic distribution (3) is of special interest, since an increase in the variance leads to the increase in critical currents. A statistical distribution with the giant dispersion possesses an extremely extended "tail" corresponding to the contributions from clusters characterized by high depinning currents. To the present, a minimum value of g ($g = 0$) is realized in the YBCO-based composites with exponential distribution of the areas of normal phase clusters [3]. The films containing such clusters exhibit increased current-carrying capacity. We may expect that superconductors containing normal phase clusters with the distribution of areas characterized by the values $g \le D - 1$ would provide for an additional increase in the critical currents.

Thus, the fractal properties of normal phase clusters significantly influence the dynamics of magnetic flux trapped in a superconductor. This phenomenon is related to a radical change in the distribution of critical currents caused by an increase in the fractal dimension of cluster boundaries. The most important result is that the fractal character of the normal phase clusters enhances pinning, thus preventing the destruction of superconductivity by the transport current. This effect opens fundamentally new possibilities for increasing the critical currents in composite superconductors by means of optimization of their geometrical–morphological characteristics.

Acknowledgments. This study was partly supported by the Russian Foundation for Basic Research, project no. 01-02-17048.

REFERENCES

1. E. Mezzetti, R. Gerbaldo, G. Ghigo, *et al.*, Phys. Rev. B **60** (10), 7623 (1999).
2. T. Higuchi, S. I. Yoo, and M. Murakami, Phys. Rev. B **59** (2), 1514 (1999).
3. Yu. I. Kuzmin, I. V. Pleshakov, and S. V. Razumov, Fiz. Tverd. Tela (St. Petersburg) **41** (10), 1739 (1999) [Phys. Solid State **41**, 1594 (1999)].
4. R. Surdeanu, R. J. Wijngaarden, B. Dam, *et al.*, Phys. Rev. B **58** (18), 12467 (1998).
5. M. Prester, Phys. Rev. B **60** (5), 3100 (1999).
6. Yu. I. Kuzmin, Phys. Lett. A **267** (1), 66 (2000).
7. Yu. I. Kuzmin, Phys. Rev. B **64** (9), 094519 (2001).
8. Yu. I. Kuzmin, Phys. Lett. A **281** (1), 39 (2001).
9. B. B. Mandelbrot, *The Fractal Geometry of Nature* (Freeman, San Francisco, 1982).
10. W. H. Warnes and D. C. Larbalestier, Appl. Phys. Lett. **48** (20), 1403 (1986).
11. B. Brown, Phys. Rev. B **61** (5), 3267 (2000).
12. D. J. Hudson, *Statistics* (CERN, Geneva, 1964).

Translated by P. Pozdeev

Technical Physics Letters, Vol. 28, No. 7, 2002, pp. 572–573. Translated from Pis'ma v Zhurnal Tekhnicheskoĭ Fiziki, Vol. 28, No. 13, 2002, pp. 83–87.

Effect of the Texture of a Thin Zinc Oxide Film on the Volume Acoustic Emission

A. A. Veselov and A. G. Veselov

Saratov Branch, Institute of Radio Engineering and Electronics, Russian Academy of Sciences, Saratov, Russia

Received December 3, 2001

Abstract—The influence of defects in piezoelectric zinc oxide film transducers on the lateral volume emission of hypersonic waves is considered for real and model piezoelectric activity distributions in the case when the wavelength is comparable with the material grain size and the emitter aperture is on the order of several wavelengths. For this purpose, the piezoelectric activity distribution in zinc oxide films on extended substrates is studied. Some possible mechanisms of the defect formation and the means of controlling these defects during the film synthesis in a gas-discharge plasma are analyzed. Directivity patterns of the piezoelectric transducers are calculated for real and model defect distributions. *© 2002 MAIK "Nauka/Interperiodica".*

In most papers devoted to the synthesis and application of polycrystalline zinc oxide films in microwave acoustics, the presence of defects in the material is admitted; however, the aperture of zinc oxide film transducers is usually so large that taking these defects into account is inexpedient. A different situation takes place in piezoelectric transducers of small aperture (on the order of ten wavelengths) and the related array structures employing side lobes of the directivity patterns of these acoustic wave emitters.

This work aimed at an experimental investigation of real and model piezoelectric activity distribution in zinc oxide films. Using a microprobe technique, the intensity of acoustic emission within a certain angular range was studied for the transducers with an aperture on the order of several wavelengths.

The films of zinc oxide used in the experiments were synthesized in a gas-discharge plasma generated in a magnetron sputtering system [1]. The character of the piezoelectric activity distribution was studied using two experimental setups employing tungsten needle probes with an edge diameter on the order of 10 μm. The needles were manufactured by electrochemical etching of a tungsten film in an alkali solution, followed by grinding the edge plane of a needle mounted in a special holder. The first setup was used for measuring the electric potential difference between a needle and metal sublayer during impact of the needle on the sample film surface. The impact strength was stabilized to a high precision with the aid of a special mechanical spring device. In the second setup, a probe served the central electrode of a low-ohmic coaxial cable (with a total diameter of about 100 μm) to which a pulsed microwave signal with a frequency of 9.5 GHz was applied. A zinc oxide film was deposited onto an yttrium–aluminum garnet (YAG) crystal with plane-parallel faces. In this system, the piezoelectric activity was evaluated as the amplitude of the first echo signal.

Figure 1 shows a typical piezoelectric activity distribution (in relative units), which could be obtained by any of the two methods. The probe moved along the substrate diameter until reaching a "hazy" zone where the optical axes of grains in the film are fully disordered. The magnetic field configuration and the substrate–target distance were selected so as to provide that the hazy ring zone would possess a diameter of about 40 mm and a width of 5–7 mm. As can be seen from Fig. 1, a given magnetron system design provides for a signal scatter not exceeding

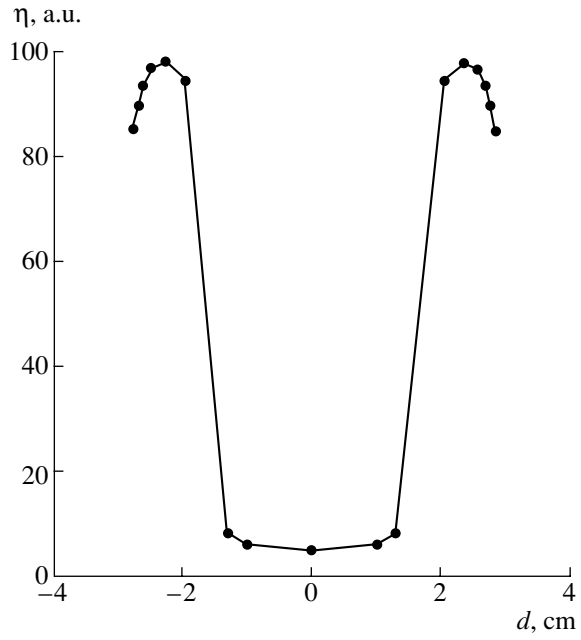

Fig. 1. A typical piezoelectric activity (η) profile of a zinc oxide film, showing a 5% scatter in the central zone and a 100% scatter in the "hazy" ring zone (*d* is the distance to the target center).

1063-7850/02/2807-0572$22.00 © 2002 MAIK "Nauka/Interperiodica"

10% inside a circle with a diameter of about 20 mm and reaching up to 100% in the hazy zone.

It was of interest to study the directivity patterns of small-aperture transducers for various dimensions and piezoelectric activities of grains in the films. The investigation was performed for both experimental (Fig. 1) and numerically modeled activity distributions. The importance of this study is related to the need in using side emission of the volume acoustic waves from both single piezoelectric transducers and array structures of such emitters.

The directivity patterns were calculated using the aperture method widely used in the theory of antennas. This method can be also used in microwave acoustics, where the assumptions necessary for its applicability are satisfied with high accuracy: the emission sources occur in the same plane (on the surface of a piezoelectric film or crystal) and the distance to detector (expressed in wavelengths) is much greater than the emitter size (aperture). These conditions correspond to a Fresnel zone, in which the directivity pattern is described by a Fourier integral from the field distribution over the emitter aperture. In our case, the emitters have an aperture on the order of ten wavelengths (for a wavelength of about 1 μm). The above conditions were certainly satisfied, since real systems employ the waveguides with a length of not less than several millimeters.

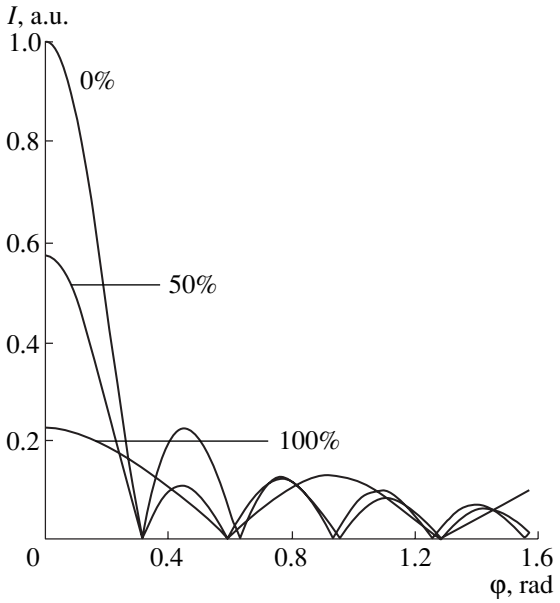

Fig. 2. Directivity patterns calculated for the piezoelectric transducers with various degrees of the texture misorientation (0, 50, and 100%) between neighboring grains (φ is the angle measured from normal to the film surface). The transducer aperture equals to ten wavelengths. The grain size is comparable to the wavelength.

Figure 2 presents the results of calculations showing that, as expected, emission in the major lobe is very sensitive with respect to defects in the films. This implies that the polycrystalline structure of the piezoelectric films has to be taken into account in the experiments employing hypersonic waves with frequencies above 10 GHz propagating at an angle to the substrate surface (acoustooptics, nanosecond delay lines).

Note that a film transducer comprising grains with 100% scatter of the activity (hazy zone) partly emits in the crystal surface (Fig. 2). In our model calculations, this is related to the fact that the grain size was taken comparable with the wavelength.

Returning to the experimental results reported previously [1], let us consider some mechanisms of the defect formation in polycrystalline films. Factors influencing stoichiometry of the deposited films were indicated in [1]. Using an experimental setup analogous to that described in [1], we conducted a series of experiments devoted to conditions determining the grain size and the optical axis orientation. As is known, both these characteristics strongly depend on almost all parameters of the gas-discharge plasma deposition process, including the substrate temperature, discharge power, and the distribution of magnetic fields. Using the quasi-closed volume technique, we stabilized the regime of synthesis and studied the effect of misorientation of the grain texture axis (which we believe to be the only factor of variation under these conditions).

Continuing the experiments described in [2], we have established that, at the center of a circular zone bounded by the hazy ring (where the degree of grain misorientation is maximum), the optical axes of grains deviate from each other within several degrees for the samples deposited at a substrate temperature of not less that 300°C. A decrease in the substrate temperature during deposition results in a strong misorientation of the optical axes, which makes the films practically inapplicable. Note that these conclusions refer to the experiments in which the film were grown on an aluminum sublayer deposited preliminarily in the same chamber. This circumstance (the presence of an unoxidized aluminum substrate) is decisive for stabilization of the experimental results and the piezoelectric film technology.

The above results can be useful for the experiments employing side lobes in the directivity patterns of both individual piezoelectric transducers and array structures with emitters based on the textured zinc oxide films.

Acknowledgments. This study was supported by the Russian Foundation for Basic Research, project no. 01-02-16317.

REFERENCES

1. E. I. Burylin, A. A. Veselov, A. G. Veselov, *et al.*, Pis'ma Zh. Tekh. Fiz. **26** (7), 31 (2000) [Tech. Phys. Lett. **26**, 282 (2000)].
2. A. G. Veselov and A. S. Dzhumaliev, Zh. Tekh. Fiz. **70** (4), 209 (2000) [Tech. Phys. **45**, 497 (2000)].

Translated by P. Pozdeev

Technical Physics Letters, Vol. 28, No. 7, 2002, pp. 574–576. Translated from Pis'ma v Zhurnal Tekhnicheskoĭ Fiziki, Vol. 28, No. 13, 2002, pp. 88–94.

Nonequilibrium Solidification Effects Induced by a Pulsed Magnetic Field in Ionic Crystals

L. A. Bityutskaya, E. S. Mashkina, V. V. Kryachko, and N. A. Rumyantseva

Voronezh State University, Voronezh, Russia

e-mail: phme22-1@main.vsu.ru

Received February 28, 2002

Abstract—A digital DTA study of the process of solidification in KCl pretreated in a weak pulsed magnetic field (PMF) reveals a latent decrease in the enthalpy of solidification, followed by recovery of the initial state 144 h after the treatment. A sharp drop in the enthalpy of solidification observed 72 h after the PMF treatment gives rise to an additional relaxation process (postsolidification effect) revealed by a long-term fluctuational evolution of dissipated heat. According to the X-ray diffraction data, the PMF action upon KCl induces an intracrystalline transformation manifested by a small decrease in the lattice parameter and a sharp increase in the reflection intensity. *© 2002 MAIK "Nauka/Interperiodica".*

Our previous investigations of the kinetics of KCl (ionic crystal) melting in the dynamic regimes by a digital DTA technique revealed cooperative pre- and postmelting transition phenomena. The observed effects exhibited features typical of the nonequilibrium phase transitions and could be characterized by a set of parameters J [1–3]. This set of parameters is kinetically dependent and sensitive to external factors. Investigation of the kinetics of melting of KCl crystals preliminary exposed to a pulsed magnetic field (PMF) ($H \sim 10^6$ A/m) showed that this treatment induced a special latent nonequilibrium phase state, which was manifested by a significant change both in the transition process parameters J and in a basic parameter—the enthalpy of melting [4].

This study, performed in development of the previous investigation [4], is devoted to the analysis of stability of the PMF-induced KCl mesophase upon melting. The criteria of stability were the parameters of the solidification process, including both the transition effects and the solidification as such.

The kinetics of solidification of the PMF-treated KCl samples was studied, in a common cycle with the melting process, using techniques described previously [1–3]. The computer-aided DTA system ensured digital data recording and automated control of the melting–solidification cycle and the data acquisition process. The DTA measurements were conducted in evacuated quartz Stepanov vessels at a heating rate of $v = 5$ K/min. The experiments were performed with 2-g samples of crystalline KCl (reagent grade, doubly recrystallized).

A pulsed magnetic field with an amplitude of $H \sim 10^6$ A/m was generated by a solenoid; the field pulses had a half-sinusoid shape, a duration of 30 μs, and a repetition rate of 50 Hz. The PMF treatment duration was $t \sim 30$ s. The samples were treated in the magnetic field and stored prior to measurements at room temperature. The DTA measurements were performed upon a single PMF treatment. Four independent series of samples (with three samples in each) were measured 24, 48, 72, and 96 h after the treatment.

Prior to the PMF treatment, each sample was characterized by determining the parameters of melting and solidification measured in a dynamic regime at a temperature variation rate of 5 K/min. The thermal cycle included heating from room temperature to 1123 K, followed by cooling from 1123 K to room temperature. The solidification process exhibited a two-stage character, with presolidification and solidification stages. In the DTA curve depicted in Fig. 1, region I corresponds to the endothermal effect of presolidification and region II, to the exothermal effect of solidification as such.

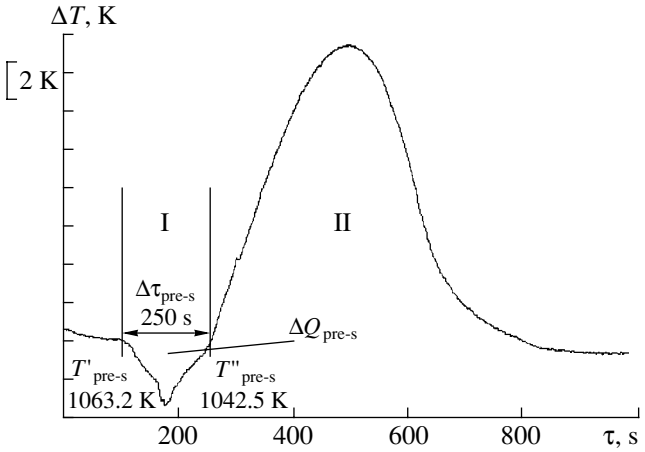

Fig. 1. The DTA curve of solidification of a PMF-treated KCl sample cooled at a rate of 5 K/min, showing the presolidification (I) and solidification (II) stages.

1063-7850/02/2807-0574$22.00 © 2002 MAIK "Nauka/Interperiodica"

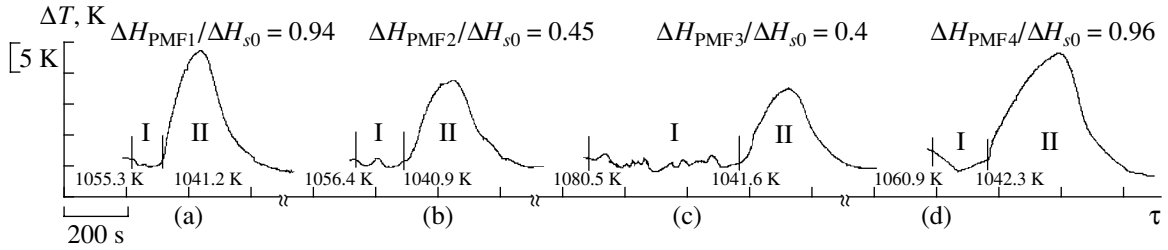

Fig. 2. Evolution of the presolidification (I) and solidification (II) stage and relative changes in the enthalpy of solidification in PMF-treated ($H \sim 10^6$ A/m, t = 30 s) KCl samples measured (a) 24, (b) 48, (c) 72, and (d) 96 h after the treatment.

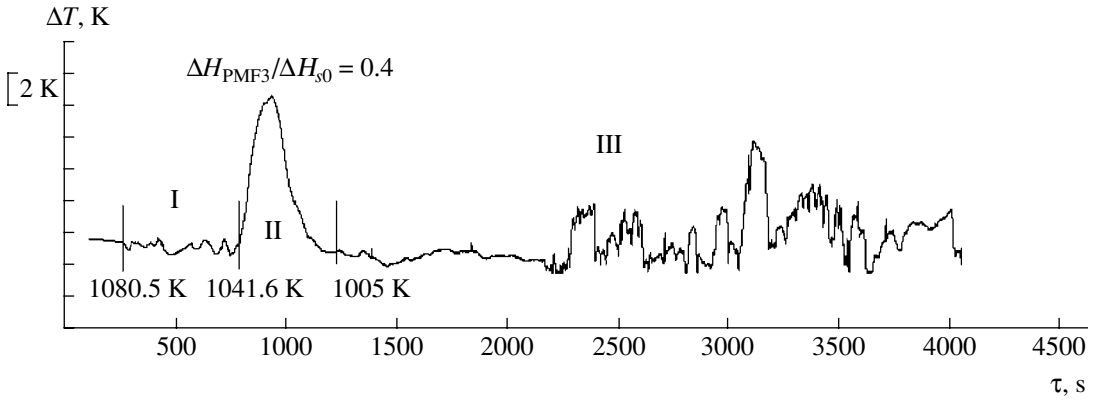

Fig. 3. The DTA curve of solidification of a PMF-treated ($H \sim 10^6$ A/m, t = 30 s) KCl sample, measured at a cooling rate of 5 K/min 72 h after the treatment, showing the presolidification (I), solidification (II), and postsolidification (III) stages.

The presolidification phenomena occurring in melts in the vicinity of the melting temperature T_m were considered in detail by Ubbelohde [5]. Observed in the melts of ionic crystals, metals, and semiconductors, these phenomena are manifested by anomalies in the physical properties and structure of the melt, in particular, by the formation of "crystal-like" regions (clusters). The presolidification effect observed in our samples apparently reflects the entropy process of melt ordering and can be characterized by a system of dynamic parameters similar to those used for description of the pre- and post-melting phenomena: $T'_{pre\text{-}s}$ (presolidification onset temperature), $T''_{pre\text{-}s}$ (presolidification end temperature), $\Delta\tau_{pre\text{-}s}$ (presolidification time interval), and $\Delta Q_{pre\text{-}s}$ (presolidification heat). The phenomenon under consideration exhibits both common and special features for substances with different types of chemical bonds: KCl, Ge, Cu, Sb [6].

The DTA measurements performed for four series of samples showed that the enthalpy of solidification of the PMF-induced mesophase changes in phase with the enthalpy of melting and also exhibits a latent character which is most pronounced 72 h after the PMF treatment [4]. Relative variations of the enthalpy were determined by changes in the area under solidification peak in the DTA curves of the same sample in series *1–4* measured before (S_0) and after (S_{PMF}) the PMF treatment. These changes were calculated by the formula $S_{PMF}/S_0 = \Delta H_{PMF}/\Delta H_{s0}$, where ΔH_{s0} and ΔH_{PMF} are the enthalpies of solidification before and after the PMF treatment, respectively. The peak areas were determined by the trapezoid method.

Figure 2 shows the pattern of changes in the presolidification behavior and the relative variations of the enthalpy of solidification over 96 h. Similar to the premelting phenomena observed 72 h after a PMF treatment, the ratio $\Delta H_{PMF}/\Delta H_{s0}$ exhibits an extremum reaching ~0.4 under the experimental conditions studied. The temperature–time domain of presolidification increases and acquires a fluctuational character. A sharp decrease in the enthalpy of solidification upon the PMF treatment gives rise to a relaxation process—the postsolidification effect (Fig. 3, region III). Beginning with a temperature of T = 1005 K, the system exhibits a thermodynamic instability leading to long-term fluctuational evolution of dissipated heat, which terminates upon cooling to room temperature.

Relaxation of the PMF-induced nonequilibrium state of KCl to the initial state was monitored by variation of the presolidification parameters and the enthalpy of solidification. Similar to the case of premelting, the relaxation has a long-term character and retains "memory" of the PMF action even 144 h after the treatment.

The KCl crystal structure after the PMF treatment was studied by X-ray diffraction in the Bragg–Brentano focusing mode on a DRON-4 diffractometer. The measurements were performed using a filtered CoK_α radiation with a weight-average wavelength of λ = 1.79021 Å generated by an X-ray tube operated in a 30 kV, 20 mA regime. The lattice parameters were determined for the initial KCl sample (a_0), immediately upon the PMF treatment (a_1) and upon storage for 72 h (a_2) and 144 h (a_3) after the treatment. There was a weak tendency to decrease in the lattice parameter measured 72 h after the PMF treatment and a relaxation close to the initial value in the sample measured 144 h after the treatment: a_1 = 6.2936 Å, a_2 = 6.2930 Å, a_3 = 6.2937 Å. The intensity of reflections varied more significantly: the most intense refection (200), measured 72 h after the PMF treatment, decreased to almost one-third of the initial height and restored the initial intensity after 144 h. The reflection intensity variations are correlated with changes in the lattice parameter: a sharp drop in the (200) reflection intensity is related to a decrease in the lattice parameter and an increase in the primary extinction. It should be noted that a radical change in the thermodynamic parameters upon solidification is not related to significant changes in the crystal structure.

Thus the melting–solidification process in KCl ionic crystals pretreated in a pulsed magnetic field is reversible. This is evidence of thermodynamic stability of the PMF-induced nonequilibrium mesophase in a broad range of temperatures on the time scale studied. The long-term fluctuational evolution of dissipated heat observed for the first-order phase transitions is analogous to the relaxation phenomena accompanying the chemically induced magnetic polarization of nuclei [7]. Observation of the magnetic-field-sensitive thermodynamic parameters of melting and solidification supplements and expands the existing notions about magnetic spin effects in condensed media [8, 9].

Acknowledgments. This study was supported by the Russian Foundation for Basic Research, project no. 01-03-32848.

REFERENCES

1. L. A. Bityutskaya and E. S. Mashkina, Pis'ma Zh. Tekh. Fiz. **21** (18), 85 (1995) [Tech. Phys. Lett. **21**, 763 (1995)].
2. L. A. Bityutskaya and E. S. Mashkina, Phase Transit. **71**, 317 (2000).
3. L. A. Bityutskaya and E. S. Mashkina, Zh. Fiz. Khim. **74** (7), 1189 (2000).
4. L. A. Bityutskaya, E. S. Mashkina, and I. Yu. Butusov, Pis'ma Zh. Tekh. Fiz. **27** (20), 14 (2001) [Tech. Phys. Lett. **27**, 850 (2001)].
5. A. R. Ubbelohde, *Molten State of Matter: Melting and Crystal Structure* (Wiley, Chichester, 1978; Mir, Moscow, 1982).
6. L. A. Bityutskaya and E. S. Mashkina, in *Fractals and Applied Synergetics: Proceedings of the First Interdisciplinary Workshop, Moscow, 1999*, p. 200.
7. Ya. B. Zel'dovich, A. L. Buchachenko, and E. L. Frankevich, Usp. Fiz. Nauk **155** (1), 3 (1988) [Sov. Phys. Usp. **31**, 385 (1988)].
8. M. N. Levin and B. A. Zon, Zh. Éksp. Teor. Fiz. **111** (4), 1373 (1997) [JETP **84**, 760 (1997)].
9. Yu. I. Golovin and R. B. Morgunov, Zh. Éksp. Teor. Fiz. **115** (2), 605 (1999) [JETP **88**, 332 (1999)].

Translated by P. Pozdeev

Technical Physics Letters, Vol. 28, No. 7, 2002, pp. 577–580. Translated from Pis'ma v Zhurnal Tekhnicheskoĭ Fiziki, Vol. 28, No. 14, 2002, pp. 1–8.

Additional Possibilities Offered by Using Porous Metallic Materials for Cooling Laser Diode Bars

V. V. Apollonov, S. I. Derzhavin, and V. N. Timoshkin

Institute of General Physics, Russian Academy of Sciences, Moscow, Russia

e-mail: vtim@kapella.gpi.ru

Received January 8, 2002

Abstract—A new scheme of using porous metallic materials (PMs) for cooling laser diode bars is proposed, which provides for a two-dimensional regime of heat removal and reduces the effective filtration length of a cooling agent. The values of characteristic limiting thermal fluxes are calculated for the heat sink made of a permeable PM, operating under conditions of a maximum permissible temperature of the active layer in a laser diode bar. *© 2002 MAIK "Nauka/Interperiodica".*

Previously [1], we suggested using permeable porous metallic materials (PMs) in heat sinks of emitters based on laser diode bars, which provides for intensification of the heat exchange process and, hence, ensures an increase in the output radiation power. A distinguishing feature of such materials is the developed stochastic carcass structure, which allows limiting possibilities of the heat exchange to be realized through optimization of the microchannel structure. The heat exchange was analyzed within the framework of a one-dimensional (1D) model [1, 2] applicable when the effective heat absorption length is smaller than the characteristic size of a laser bar. This assumption is valid for a large group of PMs in a broad range of their characteristic.

However, use of the 1D heat exchange regime was mostly related to the need for taking into account dependence of the heat-exchange properties of a PM layer on its thickness in the direction of coolant filtration [3]. In [1], we selected a minimum possible value of about 500 μm (equal to the transverse size of the diode bar along the optical axis of diodes). The role of this factor for the application of PMs (as well as any other microchannel heat sinks) increases in view of the passage to wide (up to 2 mm) diode bars. In addition, the 1D regime restricts the possible values of thermal fluxes removed from the active region of the emitter.

Thus, an additional increase in efficiency of the PM layers used in heat sinks of the laser diode bars can be provided by realization of a 2D heat exchange and/or by reduction of the effective coolant filtration length. In this communication, we propose a modular scheme of arrangement of the PM layer, which allows both possibilities to be implemented in practice.

According to the proposed scheme (Fig. 1), a heat-absorbing layer is composed of like units representing PM modules separated by impermeable spacers (made of the same material as the PM carcass) with a thickness on the order of a characteristic diameter of the carcass structure-forming elements. Small gaps on both sides of the spacers are provided for the entrance and exit of a cooling agent [4]. The spacers split the total coolant flow into equal streams (each cooling a separate module) flowing along the longitudinal bar axis. Taking into account that both spacer thickness and gap width are small as compared to the module width, the structure can be considered as a continuous porous layer, in which the effective coolant filtration length is equal to the module thickness and (in contrast to the case studied in [1]) can be selected several times smaller than the bar width.

Let us consider, by analogy with [1], the problem of determining the values of characteristic thermal fluxes Q removed by the porous layer, which are limited by the maximum permissible temperature T^* of the active layer of a laser diode bar. For example, in most of the usual GaAs-based laser diode bars, this maximum temperature does not exceed 50°C [5]. According to the results obtained in [1] in the approximation of a thermally insulated cathode with neglect of the Joule heat sources outside the active layer, $Q = T^*/(r_T + R_T)$, where R_T and r_T are the specific (per unit area) thermal resistances of the porous layer and of a combination of the diode p-layer, anode, and solder (separating the porous layer from the active layer), respectively.

Since we are interested in the maximum possible values of the output thermal fluxes, we may consider a stationary regime and assume that the characteristic dimensions of the porous layer in all directions exceed

1063-7850/02/2807-0577$22.00 © 2002 MAIK "Nauka/Interperiodica"

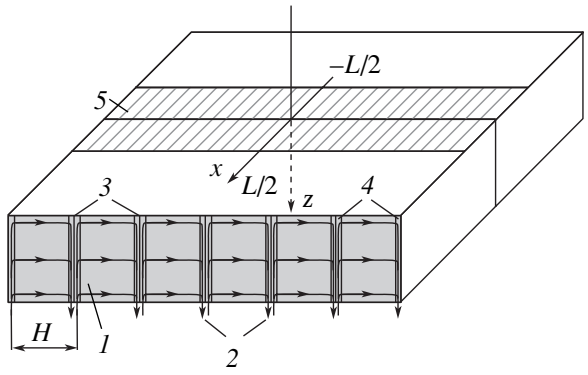

Fig. 1. Schematic diagram of a modular porous layer: (*1*) porous modules; (*2*) coolant flux; (*3*) spacers; (*4*) gaps for the entrance and exit of the coolant; (*5*) area of contact with the laser diode bar.

the characteristic heat absorption length $\Lambda = \gamma^{-1}$. Therefore, we may consider a heat exchange (which proceeds essentially via a PM carcass) with a half-space filled by a porous medium:

$$(\partial_x^2 + \partial_z^2)T - \gamma^2 T + q(\mathbf{r}) = 0$$

with the boundary conditions $\partial_z T = 0$, $z = 0$, $T = 0$, $|\mathbf{r}| \longrightarrow \infty$. The values of temperature $T(x, z)$, $z \geq 0$ are measured relative to the coolant temperature at the entrance of the channels. A flat source $q(\mathbf{r})$ on the surface of the porous layer is restricted to the size of the contact area between the porous layer and the laser diode bar (Fig. 1):

$$q(\mathbf{r}) = \frac{q}{\kappa}\delta(z)\theta\left(x + \frac{L}{2}\right)\theta\left(\frac{L}{2} - x\right),$$

where q is the thermal flux density, κ is the PM thermal conductivity, L is the bar thickness, and $\theta(x)$ is the Heaviside function.

The problem formulated above is solved using Fourier transforms (cosine and exponent transforms with respect to coordinates z and x, respectively). Eventually, the temperature distribution in the plane $z = 0$ is as follows:

$$T(x, 0) = \frac{q}{\pi\kappa\gamma}[F(1_+) \mp F(1_-)], \qquad (1)$$

where the upper and lower signs in square brackets refer to the regions of $x > L/2$ and $0 \leq x \leq L/2$, respectively;

$$F(s) = \gamma s K_0(\gamma s) + \frac{\pi}{2}\gamma s[K_0(\gamma s)L_1(\gamma s) - K_1(\gamma s)L_0(\gamma s)],$$

where $K_n(s)$ is the Macdonald function and $L_n(s)$ is the modified Struve function [6],

$$1_+ = x + \frac{L}{2}, \quad 1_- = \left|x - \frac{L}{2}\right|.$$

For $x \gg L/2$, we obtain $T(x, 0) \propto e^{-\gamma x}/\sqrt{\gamma x}$. The heat absorption in the porous layer is characterized by the distribution over z for $z \gg L/2$, which yields $T(0, z) \propto e^{-\gamma z}(1 - L\sqrt{\gamma/2\pi z})$.

In order to obtain numerical estimates of the limiting thermal fluxes Q from Eq. (1), we used a particular example (also mentioned in [1]) of a highly porous (average porosity $\Pi > 0.7$) material described in [7, 8]. Here, this PM is selected as satisfying the 2D heat exchange condition $\Lambda > L$. In the interval of Péclet numbers ($\mathrm{Pe} = d_p V/\chi$) from 50 to 2000, this material well obeys the empirical relationship $\mathrm{Nu} = 0.606\mathrm{Pe}^{0.56}$ [7, 8], where Nu is the Nusselt number for pores related to the reciprocal heat absorption length as $\gamma^2 = \kappa_l \mathrm{Nu}/\kappa_p d_p^2$ (where κ_l and χ are the thermal conductivity and thermal diffusivity coefficients of the coolant); $d_p = d\Pi/(1 - \Pi)$ is the average pore diameter for a wire carcass structure with the mean wire diameter d, $\kappa_p = \kappa_0(1 - \Pi)/(1 + \Pi)^2$ is the effective thermal conductivity of the carcass, and κ_0 is the thermal conductivity of the carcass in a compact state.

The average coolant filtration velocity V along the cooled surface in the porous layer was calculated by the equation [3, 8]

$$p/H = a\eta V + b\rho V^2, \qquad (2)$$

where p is the pressure drop across a region of thickness H, and η and ρ are the dynamic viscosity and density of the coolant. For the PM under consideration, the coefficients in Eq. (2) are as follows: $a = 6.61 \times 10^9(1 - \Pi)^{1.98}d^{-1.98}\Pi^{-6.73}$ cm^{-2} and $b = 5.16 \times 10^3(1 - \Pi)^{1.07}d^{-1.07}\Pi^{-13.07}$ cm^{-1} (d is expressed in μm).

In order to compare these results to the data obtained previously for the 1D case, we will use the same values of parameters as in [1]: $T^* = 15$ K relative to the coolant temperature (room-temperature water); $r_T \sim 10^{-3}$ K cm^2/W; $p = 1$ atm; and $L = H = 0.5$ mm. A specific thermal resistance of the porous layer was calculated using the temperature distribution averaged over the heated area: $R_T = \langle T(x, 0)\rangle/q$.

The function $Q(\Pi, d)$ calculated for the above values using Eqs. (1) and (2) is presented in Fig. 2a. For comparison, Fig. 2b shows the same function calculated using the 1D solution [1]. As can be seen, the 2D heat exchange for the PM type under consideration ($\Lambda > L$) provides for a significant increase in the characteristic limiting thermal fluxes as compared to the 1D case. Analogous calculations were performed for the

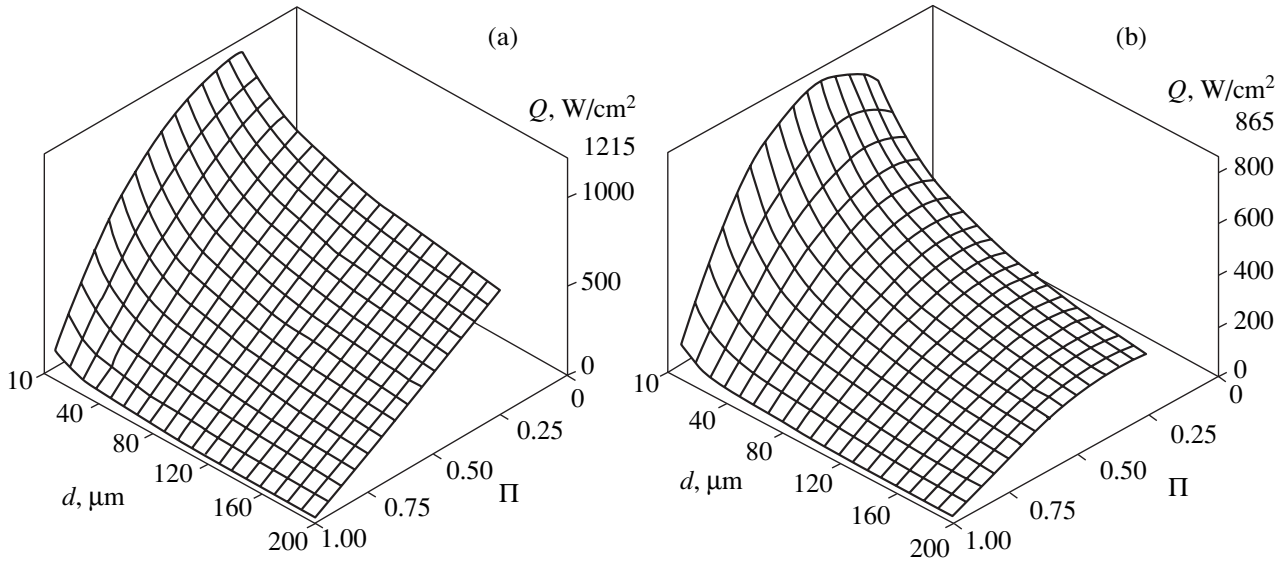

Fig. 2. Limiting thermal fluxes Q removed from an active layer by a PM layer with $\mathrm{Nu} = 0.606\mathrm{Pe}^{0.56}$ at a permissible active layer heating of $T^* = 15$ K as a function of the carcass wire diameter d [μm] and average porosity Π: (a) calculated by formula (1) for a 2D heat exchange in the modular layer; (b) calculated for a 1D heat exchange in a continuous porous layer using data from [1].

unified dependence $\mathrm{Nu} = 0.004\mathrm{Pe}$ considered in [1] (except for the Pe vale determined from b/a rather than from d_p). In the latter example, an allowance for a 2D spreading of the thermal flux leads to a difference in Q not exceeding 5%, which can be naturally expected for $\Lambda \ll L$.

It should be emphasized that the characteristic Q values presented in Fig. 2a can be significantly surpassed by increasing the limiting possible heating of the active layer (T^*) and/or by decreasing the width H of the PM module (i.e., by reducing the effective coolant filtration length). The curves in Fig. 3 calculated by Eq. (2), illustrating dependence of the limiting thermal fluxes Q on the effective coolant filtration length H, confirm the main initial stipulations concerning dependence of the cooling efficiency on this parameter.

In most modern laser diode based emitters, the bars are arranged at the edge of a heat sink so as to provide for the yield of laser radiation [9]. Therefore, the heat is removed into a quarter-space (corresponding to a region $x > -L/2$, $z > 0$ in Fig. 1). The solution (1) obtained above is mirror-symmetric relative to the plane $x = 0$ and, hence, can be considered as a combination of two independent temperature distributions created in the neighboring quarter-spaces sharing the thermoinsulating front wall ($\partial_x T|_{x=0} = 0$) by the heat sources representing the halves of the bar separated by this plane. This case of a diode bar arranged at the edge of a heat sink corresponds to half of the thermal flux calculated by formula (1) in which L is replaced by $2L$.

An especially interesting case is offered by a system in which the thickness of spacers separating the porous modules exceeds the characteristic carcass diameter. In this case, the whole structure can be considered as a system of parallel slit channels formed by spacers separating the gaps filled with a PM. It can be expected that, for a certain relation between the spacer thickness and the module width, the heat-removal capacity of such a structure would be superior to that of both continuous and modular porous layer with thin spacers.

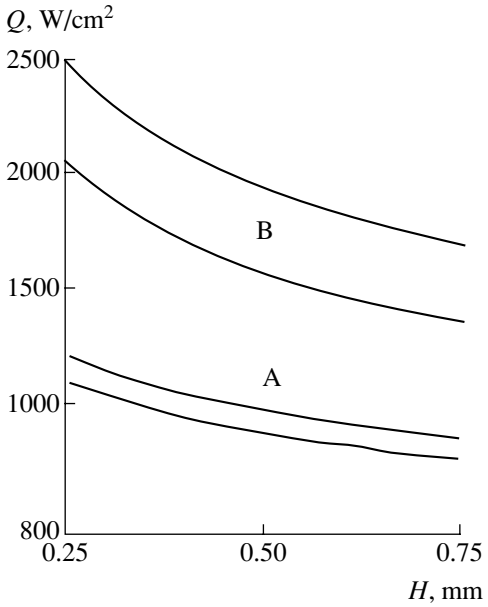

Fig. 3. The plots of limiting thermal fluxes Q versus module thickness H for PMs with $\mathrm{Nu} = 0.606\mathrm{Pe}^{0.56}$ (A) and $0.004\mathrm{Pe}$ (B) for $d = 10$ μm, $\Pi = 0.65$, $p = 1$ atm (lower curve in each pair) and 2 atm (upper curve in each pair).

REFERENCES

1. V. V. Apollonov, S. I. Derzhavin, V. N. Timoshkin, *et al.*, Pis'ma Zh. Tekh. Fiz. **25** (1), 87 (1999) [Tech. Phys. Lett. **25**, 38 (1999)].
2. V. V. Apollonov, S. I. Derzhavin, V. N. Timoshkin, *et al.*, Opt. Express **4** (1), 27 (1999); http://epubs.osa.org/opticsexpress.
3. *Porous Permeable Materials*, Ed. by S. V. Belov (Nauka, Moscow, 1987).
4. Application No. 2001132964 (2001).
5. *SDL Product Catalog 96/97* (SDL Inc., 1996).
6. *Handbook of Mathematical Functions*, Ed. by M. Abramowitz and I. A. Stegun (National Bureau of Standards, Washington, 1964; Nauka, Moscow, 1979).
7. Yu. F. Gortyshov, G. B. Murav'ev, and I. N. Nadyrov, Inzh. Fiz. Zh. **53** (3), 357 (1987).
8. V. V. Kharitonov, *Thermal Physics of Laser Mirrors* (Mosk. Inzh.-Fiz. Inst., Moscow, 1993).
9. R. W. Solarz, M. A. Emanuel, J. A. Skidmore, *et al.*, Laser Phys. **8** (3), 737 (1998).

Translated by P. Pozdeev

Technical Physics Letters, Vol. 28, No. 7, 2002, pp. 581–583. Translated from Pis'ma v Zhurnal Tekhnicheskoĭ Fiziki, Vol. 28, No. 14, 2002, pp. 9–14.

Features of the Photoconductivity of Iodine-Doped Cotton Fibers Illuminated in the Fundamental Absorption Range

A. T. Mamadalimov, B. L. Oksegendler, Sh. O. Otazhonov, B. É. Turaev, T. A. Usmanov, N. K. Khakimova, and Zh. A. Kadirov

National University of Uzbekistan, Tashkent, Uzbekistan

e-mail: mamadalimov@yahoo.com

Received January 17, 2002

Abstract—The photoelectric properties of cotton fibers treated with iodine were studied in the fundamental absorption range. The samples exhibit a sublinear illumination–current characteristic and a long-term relaxation of photoconductivity (PC) after UV irradiation ($h\nu = 5$ eV) of the iodine-doped fibers. A PC mechanism is proposed which explains both the nonlinear variation of photocurrent with illumination intensity and the PC decay according to a bimolecular recombination law after UV irradiation of the iodine-doped fiber in the fundamental absorption range. © *2002 MAIK "Nauka/Interperiodica".*

In semiconductors with sharply asymmetric deep-level trapping cross sections for electrons (S_n) and holes (S_p), dependence of the photocurrent on the intensity of illumination with $h\nu \geq E_g$ can be nonlinear (E_g is the semiconductor bandgap) [1–3]. Previously [4], we studied the temperature dependence of the electric conductivity of cotton fibers and suggested that these fibers can possess semiconductor properties. The photoelectric properties of cotton fibers containing various impurities are virtually unstudied.

In this context, we studied the photoconductivity (PC) of the iodine-doped cotton fibers illuminated in the fundamental absorption range.

Consider a semiconductor with a single deep donor level in the upper half of the forbidden band, characterized by the ionization energy E_t and the concentration M. If the Fermi level E_F is situated below E_t, the level is charged positively. The cross sections for the charge carrier trapping on this level, especially at low temperatures, may differ by several orders of magnitude, so that $S_n \gg S_p$ and $S_n \gg S_{nr}$ (S_{nr} is the cross section for electron trapping on the levels of uncontrolled impurities) [3].

Introducing deep donor levels (including multiply charged ones) into a semiconductor featuring conductivity of the hole type leads to a sharp drop in the electron lifetime τ_n and an increase in the hole lifetime τ_p. As a result, illumination of the semiconductor with light at a quantum energy of $h\nu \geq E_g$ leads to the trapping of nearly all nonequilibrium electrons by positively charged donor levels, while uncontrolled levels do not participate in the recombination process. Since τ_p is large (which corresponds to a small cross section for the hole trapping at positively charged deep donor levels), the holes are accumulated in the valence band. Therefore, the PC is determined by nonequilibrium concentration of holes generated by illumination of the semiconductor with light in the fundamental absorption range. The total photosensitivity increases, which is equivalent to sensitization of the material. In this case, the total hole concentration p is determined by the equation

$$\chi IM = \alpha_p mp, \tag{1}$$

where χ is the cross section of photoionization at the optical transition, I is the illumination flux [photons/(cm^2 s)], m is the electron concentration on levels M, $\alpha_p = V_p S_p$, and V_p is the thermal velocity of holes. If the PC is determined only by recharging of the E_t level, while the thermal generation from this level can be ignored, we may assume that $m = \Delta p = p - p_t$, where p_t and Δp are the equilibrium and nonequilibrium hole concentrations. Under these conditions,

$$\chi IM = \alpha_p(p^2 - pp_t). \tag{2}$$

In high-resistivity samples illuminated at a low intensity, $p \gg p_t$ and, hence,

$$\Delta p = \sqrt{\chi IM/\alpha_p} \sim \sqrt{I}. \tag{3}$$

The PC decay is determined by the equation

$$dp/dt = -\alpha_p p(p - p_t). \tag{4}$$

A solution to this equation for the initial condition $p =$

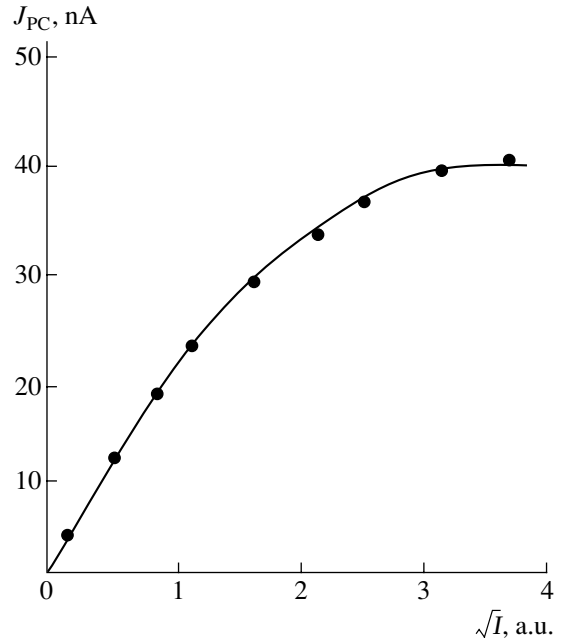

Fig. 1. The plot of photocurrent versus UV illumination intensity for the iodine-doped Golib cotton fibers ($h\nu$ = 5 eV, T = 300 K, U = 100 V).

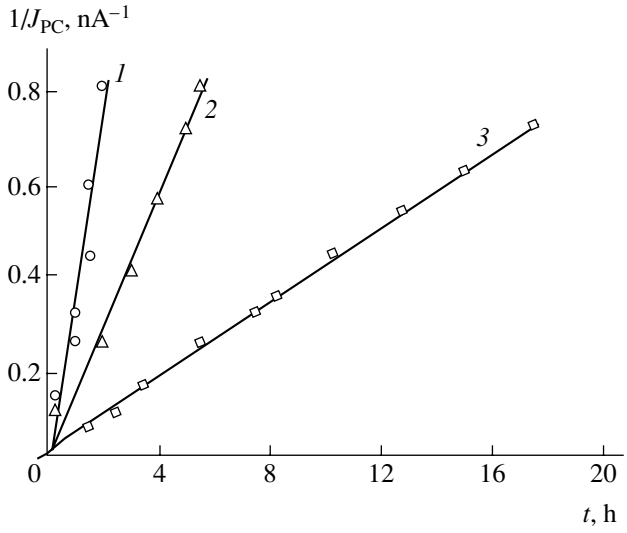

Fig. 2. The PC decay kinetics plotted as $J_{PC}^{-1} = f(t)$ for the iodine-doped cotton fibers of Khazina (*1*), Golib (*2*), and 175F (*3*) grades illuminated in the fundamental absorption range ($h\nu$ = 5 eV, T = 300 K, U = 100 V).

p_m (t = 0) and $p_t/p_m < p_t/p \ll 1$ is [5]

$$1/p = 1/p_m - \alpha_p t, \quad (5)$$

$$p = p_m/(1 - \alpha_p t p_m), \quad (6)$$

from which it is seen that the PC decay after switching off the illumination at $h\nu \geq E_g$ proceeds according to the bimolecular recombination law.

It was of interest to apply the above approach to the experimental results for iodine-doped cotton fibers. The samples were manufactured using hackled and cleaned fibers of Golib cotton, combined into ≈10-mm-long parallel bundles, each containing ≈7000 fibers. The fibers were impregnated for 10 h in a 10% iodine solution in ethanol at T = 50°C and dried in a thermostat for 30 min at 100°C (type A samples). For comparison, analogous samples were prepared without iodine treatment (type B samples). The results of measurements showed that the conductivity of type A samples increases on heating in the temperature interval from 20 to 120°C. The growth is exponential and corresponds to an activation energy of E_t = 0.77 eV. The conductivity of the cotton fibers of type A is higher than that of type B by a factor of 10^2–10^3.

We studied the PC spectra of iodine-doped Golib cotton fibers. It was found that the longwave PC limit occurs at $h\nu \approx 78$ eV, in good agreement with the experimental ionization energy determined from the temperature dependence of the electric conductivity. The PC spectra revealed a sharp decrease in the photocurrent at $h\nu$ = 2.42 eV, followed by an increase at $h\nu$ = 3.2 eV. This behavior is probably related to the fact that iodine impurity creates a deep donor level in cotton fibers at $E_t = E_c - 0.78$ eV, while the bandgap of the material is E_g = 0.78 eV + 2.42 eV = 3.2 eV.

Figure 1 shows the experimental plot of photocurrent versus illumination intensity for the iodine-doped Golib cotton fibers exposed to UV light with $h\nu$ = 5 eV. As can be seen, the region of small light intensities conforms well to the law $J_{PC} \sim \Delta p \sim \sqrt{I}$ according to relation (3). As the illumination intensity grows, the iodine donor level in the cotton fibers is filled, the effective lifetime decreases, and the $J_{PC} = f(\sqrt{I})$ curve exhibits saturation.

The PC decay kinetics was studied in iodine-doped cotton fibers of three grades: 175F, Khazina, and Golib. As can be seen from Fig. 2, the response signal variation well obeys the bimolecular recombination law. It should be noted that analogous behavior of the photocurrent was observed in silicon containing sulfur and palladium impurities [5, 6]. The fact that the PC kinetics is well described by a simple bimolecular law leads to an important conclusion. The cotton fiber structure comprises a combination of periodically arranged crystalline and amorphous regions [7]. If the electron–ion processes related to the presence of iodine atoms were to occur in the amorphous regions, the process kinetics would obey the Kohlrausch law $f(t) = \text{const} \cdot \exp[-(t/\tau)^\beta]$, where $0 < \beta < 1$ [8]. Since the real system behaves differently, we conclude that the iodine donor impurity is located in the crystalline regions of cotton fibers.

REFERENCES

1. S. M. Ryvkin, *Photoelectric Effects in Semiconductors* (Fizmatgiz, Moscow, 1963; Consultants Bureau, New York, 1964).
2. A. A. Lebedev, A. T. Mamadalimov, and N. A. Sultanov, Fiz. Tekh. Poluprovodn. (Leningrad) **5** (12), 2277 (1971) [Sov. Phys. Semicond. **5**, 1990 (1971)].
3. A. T. Mamadalimov, A. A. Lebedev, and E. V. Astrova, *Spectroscopy of Deep Centers in Semiconductors* (Tashkent University, Tashkent, 1999).
4. M. Shermatov, A. T. Mamadalimov, T. A. Usmanov, and Sh. M. Shermatov, Dokl. Akad. Nauk Resp. Uzb., No. 4, 21 (1995).
5. A. A. Lebedev, N. A. Sultanov, and V. M. Tuchkevich, Fiz. Tekh. Poluprovodn. (Leningrad) **5** (1), 31 (1971) [Sov. Phys. Semicond. **5**, 25 (1971)].
6. A. A. Lebedev, M. S. Yunusov, A. T. Mamadalimov, and N. A. Tursunov, Fiz. Tekh. Poluprovodn. (Leningrad) **8** (4), 691 (1974) [Sov. Phys. Semicond. **8**, 442 (1974)].
7. M. Aliev and A. Bekmukhamedov, *Cotton and Its Production* (Ukituvchi, Tashkent, 1991).
8. *Fractals in Physics*, Ed. by L. Pietronero and E. Tosatti (North-Holland, Amsterdam, 1986; Mir, Moscow, 1988).

Translated by P. Pozdeev

Technical Physics Letters, Vol. 28, No. 7, 2002, pp. 584–585. Translated from Pis'ma v Zhurnal Tekhnicheskoĭ Fiziki, Vol. 28, No. 14, 2002, pp. 15–18.

On the Possible Mechanism of Crystal Growth from Melt under Zero Gravity Conditions

S. V. Kotov, A. R. Lyutikov, Yu. P. Khukhryansky, I. N. Arsent'ev, and E. A. Kuznetsova

Voronezh State Technical University, Voronezh, Russia

e-mail: kotov@vmail.ru

Received January 24, 2002

Abstract—A possible mechanism of the growth of semiconductor single crystals from melt under zero gravity conditions is considered. The results of computer simulation performed by the molecular dynamics method for a thin layer of melt on a single crystal surface are presented. The main characteristics of the melt component dynamics suggest a mechanism whereby the crystal grows to a significant extent due to the attachment of atoms or small atomic clusters, which accounts for the perfection of the crystal structure being grown. © *2002 MAIK "Nauka/Interperiodica".*

In recent years, large attention of researchers has been drawn to the theory and practice of growing semiconductor single crystals under zero gravity conditions. This interest is related to the fact that, using this process, it is possible to obtain single crystals possessing highly perfect structure. However, the actual technology of growing semiconductor single crystals under zero gravity conditions is very expensive. This is related, first, to the high cost of experiments necessary for determining some important technological parameters of the crystallization process and, second, to difficulties encountered in the attempts to model this crystallization process because of the lack of an established theory of the single crystal growth under zero gravity conditions.

Below we will consider a possible mechanism of the growth of a semiconductor single crystal from melt under zero gravity conditions.

As is known, atoms on the substrate surface produce a force field favoring the formation of mobile atomic groups (clusters) of a crystallizing substance [1]. Weakly bound to the substrate, these clusters perform chaotic motions in the melt at the substrate surface. Moving sufficiently far away from the surface, the clusters break into separate atoms. Apparently, at a certain distance δ from the substrate surface, the aforementioned field significantly decays and the probability of atomic association into clusters becomes small, whereas the probability of separation is large. On the contrary, immediately at the substrate surface, the field potential exhibits a maximum which leads to a high probability of the cluster formation at a low probability of decay.

The dynamic process of cluster formation and decay proceeds in the δ-layer occurring in thermodynamic equilibrium with the substrate. Figure 1 shows a schematic diagram illustrating the distribution of atoms and clusters across the δ-layer under zero gravity conditions. As can be seen, the concentration gradients of atoms and clusters are directed oppositely. A decrease in the temperature violates the thermodynamic equilibrium so that both atoms and clusters in the near-surface layer tend to deposit onto the substrate *I*.

Let us consider the dynamics of this process. A change in the number of atoms in a cluster is determined by interplay of the probabilities of the cluster formation and decay. As noted above, the formation of clusters is caused by the presence of a force field at the substrate surface. Assuming that variation of the force field with distance from the substrate possesses an exponential character, we can use the following expressions for the probabilities of association and decay events:

$$W_A = W_{A0}\exp\left(-\frac{E_A}{kT}\right)\left(2\exp\left(\frac{z}{\delta}\ln(0.5)\right)-1\right), \quad (1)$$

$$W_D = W_{D0}\exp\left(-\frac{E_D}{kT}\right)\left(\exp\left(\frac{z}{\delta}\ln(2)\right)-1\right), \quad (2)$$

where E_A and E_D are the characteristic energies of the cluster association and decay, respectively, and W_{A0} and W_{D0} are the corresponding normalization factors; z is the normal coordinate.

The phase trajectories of the clusters were determined using standard procedures of the molecular dynamics method. For atoms in the melt (performing statistically independent motions), the dynamics of the phase trajectory variation was not traced and the atomic coordinates at each step were set in a pseudorandom manner within a certain sphere (with a radius of several σ) surrounding each cluster [2].

Let us consider the results of preliminary calculations using this model. Figure 2 shows the patterns of

1063-7850/02/2807-0584$22.00

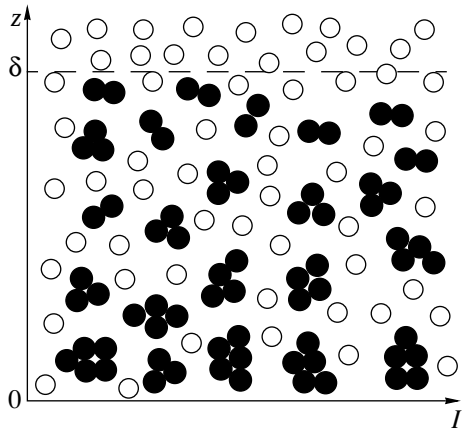

Fig. 1. A schematic diagram illustrating the distribution of atoms and clusters across a δ-thick layer in the melt (*I* is the substrate).

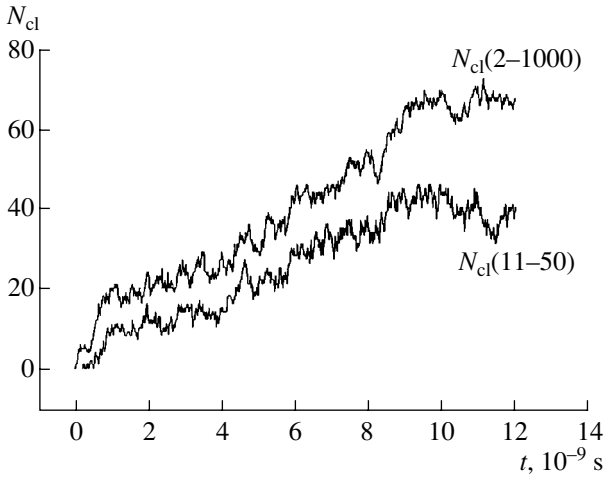

Fig. 2. Variation of the number of clusters in a boundary layer at the substrate surface.

variation in the total numbers $N_{cl}(2–1000)$ and $N_{cl}(11–50)$ of clusters containing from 2 to 1000 atoms and from 11 to 50 atoms, respectively. As can be seen, the number of clusters reaches a maximum value within 10^{-8} s and then fluctuates around this level.

During simulation, we determined the average values of the cluster velocity components. For the lateral components v_x and v_y, the average values were close to zero. For the normal velocity component v_z, the average value was about $v_z = 10^{-1}$ m/s, which is 2–3 orders of magnitude lower as compared to the root-mean-square velocity of the thermal atomic motion. Thus, the system features a drift of clusters from substrate to the bulk of a melt at a velocity increasing with the cluster size. There are two possible variants. If the density of clusters is greater than that of the melt, the force field will drive the clusters toward the growth surface. In this case, the growth rate is higher, but the single crystal structure is less perfect. Should the cluster density be lower than that of the melt, the clusters will tend to drift away from the surface and the growth will proceed primarily due to the attachment of small-size clusters or atoms. In this case, the growth rate will be low, but the single crystal structure will be more perfect.

Thus, using the phenomenon described above, it is possible to provide for the conditions under which single crystal growth would proceed predominantly due to atoms or small-size clusters. This must lead to the formation of structurally perfect crystal layers.

Acknowledgments. This study was supported by the Ministry of Education of the Russian Federation within the program of basic research in technical sciences "Semiconductor Metallurgy" (project no. T00-5.4-2927).

REFERENCES

1. G. I. Distler, V. M. Kanevskiĭ, and D. M. Gerasimov, Izv. Akad. Nauk SSSR, Ser. Fiz. **48** (9), 1698 (1984).
2. A. R. Lyutikov and Yu. P. Khukhryansky, in *Proceedings of the Fourth International Conference on Single Crystal Growth, Materials Strength Problems, and Heat and Mass Transfer, Obninsk, 2001*, p. 1059.

Translated by P. Pozdeev

Technical Physics Letters, Vol. 28, No. 7, 2002, pp. 586–588. Translated from Pis'ma v Zhurnal Tekhnicheskoĭ Fiziki, Vol. 28, No. 14, 2002, pp. 19–25.

Effects of Deterministic Chaos and Strange Attractor in the Radar of Dynamic Systems of the Vegetative Cover Type

A. A. Potapov and V. A. German

Institute of Radio Engineering and Electronics, Russian Academy of Sciences, Moscow, Russia

e-mail: potapov@mail.cplire.ru

Received January 10, 2002

Abstract—The results of experiments aimed at detecting the regime of deterministic chaos in the 2.2 mm circularly polarized radar of vegetative cover are reported. Processing of the reflected signals with the aid of a correlation integral revealed a strange attractor controlling the radar scattering of millimetric waves. The dynamic and geometric characteristics of the strange attractor were measured. *© 2002 MAIK "Nauka/Interperiodica".*

The attention of many researchers in various fields of science is now drawn to the chaotic behavior of dynamical systems and fractal geometry problems [1–7]. By dynamical system (DS) is termed an object or process for which the state (or a set of selected quantities) at a given time instant is uniquely determined and a deterministic operator of evolution is defined. The concept of DS is applicable to the objects of any nature. Upon the decay of transient processes in a given DS, we can separate a limiting set of points in the phase space of this system which attracts the phase trajectories. The existence of such sets, called attractors, is related to the ability of the phase volume of a DS to contract under the action of the evolution operator. If an attracting set in the phase space of a DS exhibits a regime of established aperiodic oscillations, this attractor is called strange [8]. A strange attractor is always characterized by a fractional fractal dimension *D*. An important feature of chaotic motions is their extremely high sensitivity to small changes in the initial conditions. This implies that two closely spaced trajectories in the phase space exponentially recess with time.

The rate of recession is quantitatively expressed in terms of Lyapunov exponents, which provide for a complete characterization of the degree of complexity of a chaotic behavior and the structure of an attractor in the phase space of a DS. The most important is the maximum Lyapunov exponent λ_1, the positive value of which is indicative of chaos in the DS. The Lyapunov exponent can be defined as

$$\lambda = \lim_{\substack{t \to \infty \\ d(0) \to 0}} \left(\frac{1}{t}\right) \log_2 \left[\frac{d(t)}{d(0)}\right], \qquad (1)$$

where $d(t) = [\sum_{i=1}^{n} \delta x_i^2(t)]^{1/2}$ is the norm determining the measure of recession for two adjacent trajectories (the base trajectory $\mathbf{x}$ and the neighboring trajectory with the initial conditions $\mathbf{x}(0) + \delta\mathbf{x}(0)$). The dimension of a DS attractor can be determined using Lyapunov exponents by the Caplan–Jork, Mori, and Young formulas [9]. Note that the geometry and dynamics of strange attractors are closely related: upon finding the Lyapunov exponents, one can make a judgment on the geometry of attractors; by measuring the fractal dimension *D*, it is possible to gain information about the Lyapunov exponents of the given DS [10].

From the classical standpoint, irregular behavior in the nature of a physical phenomenon is related to a large number of degrees of freedom. A radar signal scattered from Earth covers is modeled by a stochastic noise process. However, progress in the theory of dynamical systems allows us to consider this problem in more detail from different positions. The theory of stochastic processes is based on an empirical method which allows us to eliminate difficulties related to insufficient information about physical sources responsible for the appearance of the given phenomenon. However, this theory fails to explain the reasons of stochasticity. According to DS theory, even a very small number of degrees of freedom is sufficient to give rise to a deterministic chaos [11, 12]. The idea of using such models for the description of radar response is highly promising and provides for a deeper insight into the nature of the phenomenon under consideration. The first experimental results [13–15] suggested that a low-dimensional strange attractor might exist that determines the radar backscattering from a sea surface.

In this study, we obtained the first experimental evidence for the existence of a strange attractor controlling the millimetric radar signal scattering from a vegetative cover, which was hypothetically predicted by one of the authors as early as in 1997 [16]. The initial experimental data were represented by the 2.2 mm circularly polarized radar results [17] obtained with an energy potential of 140 dB. The angle of incidence was Θ = 0°–80°, and the average wind velocity was 3 m/s. The biometric characteristics of the vegetative cover were

1063-7850/02/2807-0586$22.00

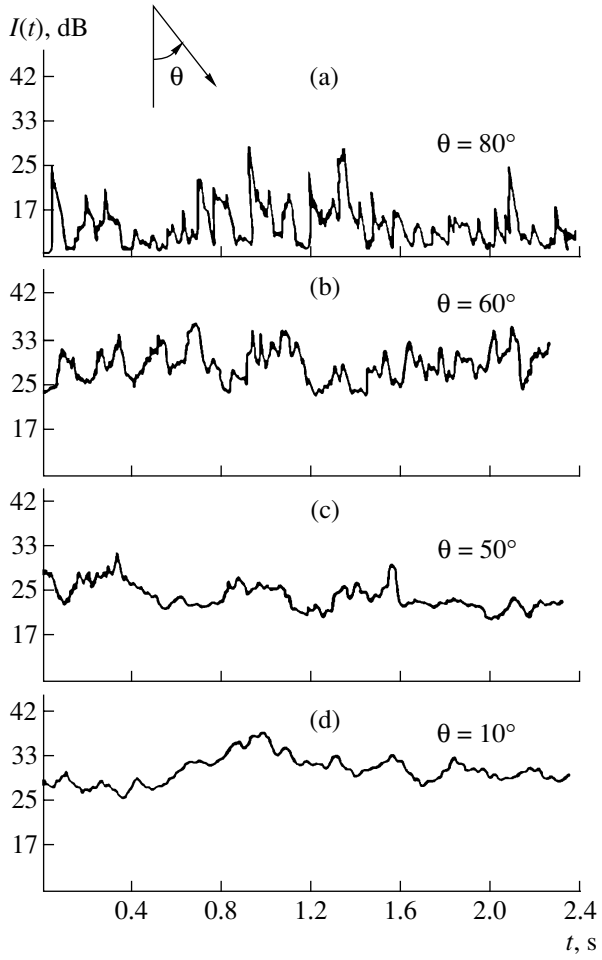

Fig. 1. Fluctuations of the intensity of 2.2 mm radio waves scattered from a dry herbage at various angles of incidence Θ = 80° (a), 60° (b), 50° (c), and 10° (d).

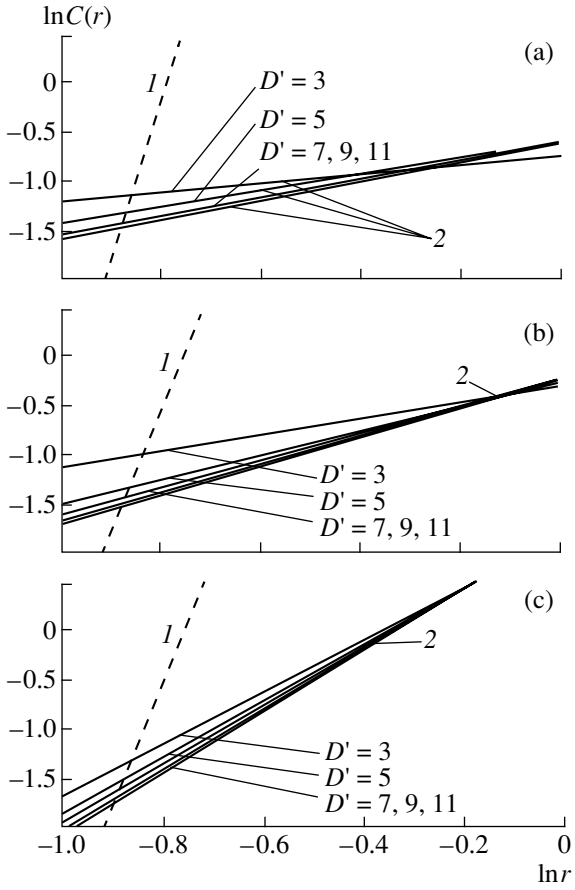

Fig. 2. Plots of the correlation integral $C(r)$ versus size r of the phase space partition cell for (*1*) the Gauss noise process and (*2*) the radar reflections from a vegetative cover for the dimensions of embedding D' = 3, 5, 7, 9, and 11: (a) radar reflection without noise; (b) noise level, 6 dB; (c) noise level, 3 dB.

reported in [17]. Diagrams of the received signal are presented in Fig. 1.

The DS attractor reconstruction using a one-dimensional time series was based on the Takens theorem [18]. In order to reconstruct the attractor proceeding from ordered measurements of a single variable, it is necessary to construct an embedded space of dimension $D' = 2N_0 + 1$, so as to describe all possible topological features of the attractor. The quantity $N_0 \geq \text{int}[D] + 1$ determines the number of differential equations of the first order necessary for description of the physical behavior of the DS studied. Here, int[D] denotes the operation of separating the integer part of D, and D is the true fractal dimension of the attractor. The attractor dimension was estimated using a correlation integral defined as

$$C(r) = \lim_{N\to\infty} \frac{1}{N^2} \sum_{\substack{i,j=1 \\ i\neq j}} H(r - |\mathbf{x}_i - \mathbf{x}_j|), \qquad (2)$$

where r is the size of the phase space partition cell, N = 50 000 is the number of points in the initial pattern, H is the Heaviside function, $\mathbf{x}_i = \mathbf{x}(i\Delta t)$, and Δt is the time step of discretization.

The correlation integral is essentially the number of the pairs of points spaced by a distance shorter than r, normalized to N^2. The slope of the linear portion of $\ln C(r) = f(\ln r)$ determines the required value of the strange attractor dimension. For a finite dimension of D, the correlation integral (2) exhibits saturation. Figure 2 shows the experimental plots of $C(r)$ versus r for radar reflections from vegetative cover with and without noise at an incident angle of 50°, in comparison to the Gauss process. For the process of radio wave reflection from a vegetative cover, the dimension of embedding is $D' = 5$. The higher the noise in the initial data set, the greater the D' value. When the level of noise exceeds that of the useful signal, the process of saturation ceases. According to the data of Fig. 2, the fractal dimension of the strange attractor is $D \approx 1.8$. The correlation integral $C(r)$ can be also used as a means of separating deterministic chaos and external white noise. The Gauss noise exhibits no tendency to saturation (Fig. 2) and, hence, corresponds to an attractor of

infinite dimension. This difference is widely used for the treatment of time patterns of unknown nature. In the experiments involving identification of a chaotic process on the additive noise background, the main limitation is the signal-to-noise ratio. In our case, the minimum signal to noise ratio is +10 dB, in sharp contrast to the data reported in [15].

The maximum Lyapunov exponent, calculated by formula (1) using an algorithm [19] as modified in [20], was found to be $\lambda_1 \geq 0.6$ bit/s. Therefore, on measuring the current conditions to within 1 bit, we loss all the predictive power in time for 1.7 s. For this reason, the interval of prediction [21] of the reflected signal intensity is greater than the correlation time τ by a factor of approximately 8 (at a wind velocity of 3 m/s, $\tau \approx$ 210 ms [17]).

Thus, we have experimentally studied for the first time the characteristics of a strange attractor arising in the radar signal reflected from a vegetative cover. Using these data, it is possible to construct new models of signal scattering from natural dynamical systems. The results indicate that no more than three independent variables are necessary to provide for a correct description of the process of radio wave scattering.

REFERENCES

1. A. S. Dmitriev and V. Ya. Kislov, *Stochastic Oscillations in Radiophysics and Electronics* (Nauka, Moscow, 1989).
2. V. S. Anishchenko, T. E. Vadivasova, and V. V. Astakhov, *Nonlinear Dynamics of Chaotic and Stochastic Systems* (Saratov. Univ., Saratov, 1999).
3. A. B. Katok and B. Hasselblatt, *Introduction to the Modern Theory of Dynamical Systems* (Cambridge Univ. Press, Cambridge, 1995; Faktorial, Moscow, 1999).
4. G. G. Malinetskiĭ and A. B. Potapov, *Modern Theory of Nonlinear Dynamics* (Editorial URSS, Moscow, 2000).
5. E. E. Peters, *Chaos and Order in the Capital Markets: A New View of Cycles, Prices, and Market Volatility* (Wiley, New York, 1996; Mir, Moscow, 2000).
6. M. Tabor, *Chaos and Integrability in Nonlinear Dynamics: An Introduction* (Wiley, New York, 1989; Editorial URSS, Moscow, 2001).
7. *Risk Management: Risk, Stable Development. Synergetics*, Ed. by V. A. Vladimirov, Yu. A. Vorob'ev, S. S. Salov, *et al.* (Nauka, Moscow, 2000).
8. *Strange Attractors: Collection of Articles*, Ed. by Ya. G. Sinaĭ and L. P. Shil'nikov (Mir, Moscow, 1981).
9. V. P. Dymnikov and A. N. Filatov, *Principles of Mathematical Theory of Climate* (VINITI, Moscow, 1994).
10. A. A. Potapov, Zarubezhn. Radioélektron. Usp. Sovrem. Radioélektron., No. 6, 3 (2000).
11. H. G. Schuster, *Deterministic Chaos* (Physik-Verlag, Weinheim, 1984; Mir, Moscow, 1988).
12. A. A. Potapov and V. A. German, in *Proceedings of the VII All-Russia School-Workshop "Physics and Application of Microwaves"* (Mosk. Gos. Univ., Moscow, 1999), Vol. 2, p. 196.
13. H. Leung and S. Haykin, Appl. Phys. Lett. **56** (6), 593 (1990).
14. H. Leung and T. Lo, IEEE J. Ocean Eng. **OE-18** (3), 287 (1993).
15. D. Blacknell and C. J. Oliver, J. Phys. D **27** (8), 1608 (1994).
16. A. A. Potapov, in *Proceedings of the LII Scientific Session Devoted Radio Day, Moscow, 1997*, Vol. 1, p. 169.
17. A. A. Potapov, Radiotekh. Élektron. (Moscow) **36** (2), 239 (1991).
18. F. Takens, in *Dynamical Systems and Turbulence*, Ed. by D. A. Rang and L. S. Young (Springer-Verlag, New York, 1981), Lecture Notes in Mathematics, Vol. 898, p. 366.
19. A. Wolf, J. B. Swift, H. L. Swinney, and J. A. Vastano, Physica D (Amsterdam) **16** (3), 285 (1985).
20. P. S. Landa and V. I. Chetverikov, Zh. Tekh. Fiz. **58** (3), 433 (1988) [Sov. Phys. Tech. Phys. **33**, 263 (1988)].
21. *Limits of Predictability*, Ed. by Yu. A. Kravtsov (TsentrKom, Moscow, 1997).

Translated by P. Pozdeev

Technical Physics Letters, Vol. 28, No. 7, 2002, pp. 589–591. Translated from Pis'ma v Zhurnal Tekhnicheskoĭ Fiziki, Vol. 28, No. 14, 2002, pp. 26–31.

On the Cathodoluminescence of a CuCl Powder

T. V. Zakharova and N. A. Zakharov

Moscow State University of Polygraphy, Moscow, Russia

e-mail: zakharov@igic.ras.ru

Received January 8, 2002

Abstract—The electron-beam-excited luminescence spectra of a CuCl powder were studied in a temperature interval from 80 to 400 K. New emission peaks were observed at 393.5, 700, 780, and 830 nm. The emission intensity distribution in the spectrum significantly varies with the temperature. The Z_3 exciton emission band exhibits an anomalous temperature-induced displacement. © *2002 MAIK "Nauka/Interperiodica"*.

The luminescent properties of copper chloride (CuCl) have been extensively studied for many years [1–8]. It was established that the emission spectrum of CuCl measured at liquid nitrogen temperature at the fundamental absorption edge exhibits $Z_{1,2}$ (377.0 nm) and Z_3 (385.0 nm) bands due to the free excitons [2–5], the I_1 band at 387.8 nm due to a bound exciton [2–6], and a band at 390.0 nm assigned to exciton molecules [4]. In the longwave region, the spectrum displays a violet luminescence band peaked at 425 nm [2, 5]. Additional broad emission bands were observed at 450, 490, 530, and 650 nm [2].

We have experimentally studied the luminescence of a CuCl powder in the spectral range from 300 to 900 nm using the samples excited by an electron beam. Variation of the emission spectrum was studied in the temperature interval from 80 to 400 K. The experiments were performed with a commercial CuCl powder of analytical grade, possessing a cubic crystal structure. The samples were excited by an electron beam with a current density on the order of 2×10^{-5} A/cm^2 and a total power of 10 kW.

Figure 1 shows the cathodoluminescence spectra of a CuCl powder measured at various fixed temperatures. In the UV range, the spectra were normalized to the intensity of the emission band at 390.0 nm (Fig. 1a), and in the visible and near IR range, to the 780.0 nm band intensity (Fig. 1b). Figure 2 shows the temperature variation of the intensity of some emission bands in the interval from 80 to 300 K.

The cathodoluminescence spectrum of a CuCl powder at 80 K is characterized by the emission maxima at 385.0, 387.8, 390.0, 393.5, 418, 630, 700, 780, and 830 nm (Fig. 1). In the UV spectral range, a dominating emission band is that at 390.0 nm. When the temperature is increased, the intensity of this band decreases, while that of the Z_3 free-exciton band (situated at 385.0 nm at 80 K) initially increases (up to ~127 K) and then drops. The growth in the Z_3 emission band intensity is accompanied by rapid "blocking" of the recombination channels responsible for most of the other emission bands (387.8, 390.0, 393.5, 418, 630, 700, and 830 nm at 80 K), which probably accounts for the buildup of the free-exciton emission. The activation energy of the temperature quenching calculated for the Z_3 and 390.0 nm emission bands is 0.2 eV, while that for the violet emission band is 0.14 eV.

An increase in the temperature to 130 K leads to the appearance of a green emission with a peak at 530 nm. The intensity of this band reaches maximum at 200 K and then decreases (see Figs. 1b and 2). The luminescence band observed at 780 nm also grows with the temperature and behaves like the green emission band.

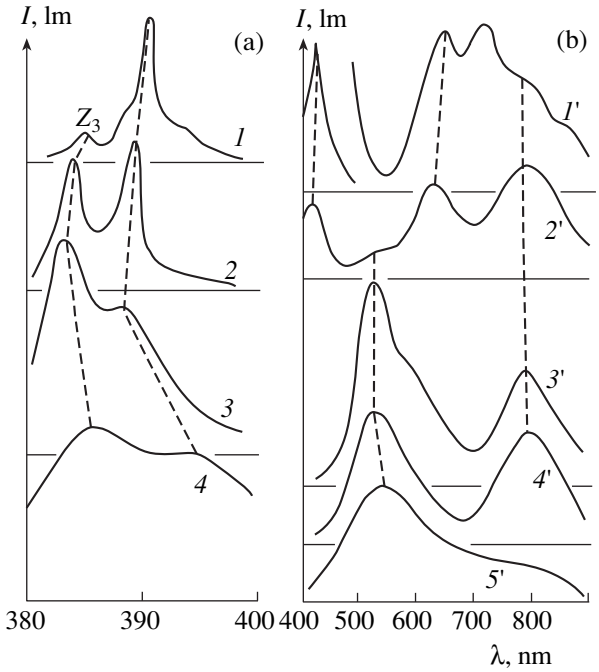

Fig. 1. The cathodoluminescence spectra of a CuCl powder measured at various fixed temperatures T = 80 (*1*, *1'*), 127 (*2*), 129 (*2'*), 166 (*3'*), 230 (*3*, *4'*), 323 (*4*), and 354 K (*5'*)

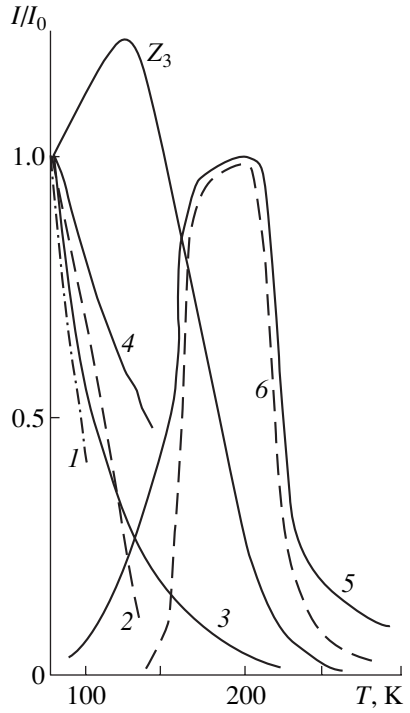

Fig. 2. Temperature dependence of the intensity of various emission bands peaked at 383.5 (*1*), 418 (*2*), 390.0 (*3*), 387.8 (*4*), 780 (*5*), and 500 nm (*6*) at 80 K, and of the Z_3 emission band at 385.0 nm.

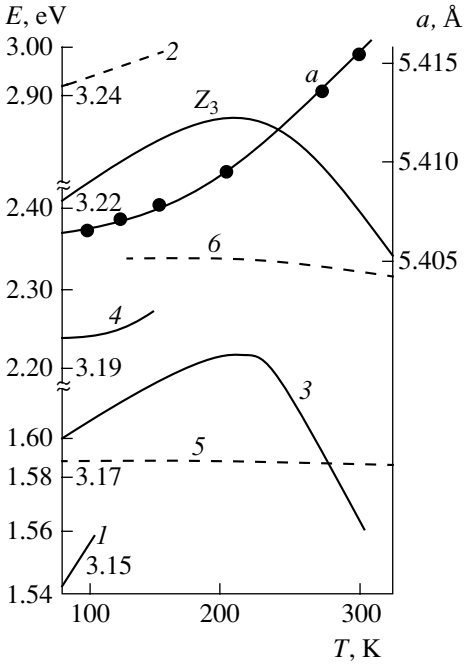

Fig. 3. Temperature dependence of the crystal lattice parameter *a* of CuCl [12] and the positions of various bands (*1–6*, Z_3) in the cathodoluminescence spectrum of CuCl (notation is the same as in Fig. 2). The left-hand scale on the energy axis refers to curves *2*, *5*, and *6*, and the right-hand scale, to the other curves.

These results coincide with the data for CuCl films [1], but differ from the behavior reported in [2, 9], where luminescence of this type exhibited a decay at temperatures above 78 K [2] or above 140 K [9]. The red emission band at 630 nm was also reported to decrease at temperatures above 140 K [9]. It should be noted that no emission bands at greater wavelengths were previously observed in the emission spectra of CuCl. At temperatures above 80 K, only the band peaked at 780 nm is retained among the aforementioned bands, and even this band disappears above 300 K.

It is possible to perform a comparative analysis of behavior of the emission centers responsible for the bands at 418 and 530 nm. The interplay between these emission centers can be interpreted within the framework of the theory of recombination interaction between various centers based on a model suggested by Fock [10]. According to this model, the recombination interaction between emission centers related to two levels in the forbidden band must lead to the emission energy redistribution over the spectrum in favor of the longwave band, while an increase in the excitation changes the spectral energy distribution in favor of the shortwave band. It should be noted that the latter phenomenon was observed on comparing the photoluminescence spectra of the powders excited by a nitrogen laser and by a mercury lamp. We believe that a similar reasoning applies to the behavior of some orange and red emission bands.

We observed an anomalous temperature-induced shift of the Z_3 free-exciton emission band and the band at 390.0 nm (Fig. 3). It is possible to separate several regions in which these bands exhibit a monotonic displacement characterized by a certain average temperature coefficient β. The Z_3 band monotonically shifts in the temperature intervals 80–127, 127– 200, 200–230, and 230–400 K with the coefficient $\beta = 1.6 \times 10^{-4}$, 0.5×10^{-4}, 0, and -2.5×10^{-4} eV/K, respectively. By the same token, the 390.0 nm emission band monotonically shifts in the temperature intervals 80–127, 127–200, 200–230, and 230–400 K with the coefficient $\beta = 1.54 \times 10^{-4}$, 0.84×10^{-4}, 0, and -4.6×10^{-4} eV/K, respectively. Thus, there is a significant bending at 200–230 K in the temperature-induced shift of both the Z_3 and 390.0 nm emission bands.

According to the published data [2, 3, 5, 7], these emission bands of CuCl must shift toward shorter wavelength with increasing temperature. In order to explain the anomalous behavior, we might suggest that a new emission band appears on heating above 150 K and shifts toward longer wavelengths with increasing temperature. This component must be close to the 390.0 nm band, since it is characterized by a large negative shift at high temperatures (Fig. 3). Such a band *H*, appearing above 150 K and shifting toward longer wavelengths, was reported in [7]. However, our attempts at detecting this band failed. The shape of the

observed luminescence spectra does not allow us to suggest any overlap with the *H* band. It should be noted that the anomalous temperature displacement of the Z_3 and N_3 bands was also not observed in [7].

The longwave shift of the fundamental absorption of CuCl at temperatures above 77 K was reported in [11]. Therefore, it is not excluded that the observed anomalous temperature-induced displacement of the Z_3 and 390.0 nm emission bands (Fig. 3) reflects a monotonic thermal expansion of the CuCl crystal lattice described in [12], explained by a growth in the fraction of ionic bonds with temperature in the 80–300 K range.

REFERENCES

1. K. V. Shalimova and N. S. Mendakov, Zh. Éksp. Teor. Fiz. **26** (2), 248 (1954).
2. M. Ueta and T. Gono, J. Phys. Soc. Jpn. **20** (3), 401 (1965).
3. M. Ueta, T. Gono, and T. Yashiro, J. Phys. Soc. Jpn. **20** (6), 122 (1965).
4. J. B. Grun, S. Nikitine, A. Bivas, *et al.*, J. Lumin. **1/2**, 241 (1970).
5. Y. Kaify, Y. Kawate, and S. Naranishi, J. Phys. Soc. Jpn. **22** (2), 517 (1967).
6. M. Certier, C. Wecker, and S. Nikitine, J. Phys. Chem. Solids **30** (9), 2135 (1969).
7. In Yu Chong, T. Goto, *et al.*, J. Phys. Soc. Jpn. **34** (3), 693 (1973).
8. H. Souma, T. Goto, T. Ohta, *et al.*, J. Phys. Soc. Jpn. **29** (3), 679 (1970).
9. T. Goto, J. Phys. Soc. Jpn. **20** (9), 1654 (1965).
10. M. V. Fok, *Introduction to the Kinetics of Luminescence of Phosphor Crystals* (Nauka, Moscow, 1964).
11. M. S. Brodin and A. S. Krochuk, Opt. Spektrosk. **14** (1), 88 (1964).
12. J. Plendy and I. C. Mansur, Appl. Opt. **11** (5), 1194 (1972).

Translated by P. Pozdeev

Technical Physics Letters, Vol. 28, No. 7, 2002, pp. 592–594. Translated from Pis'ma v Zhurnal Tekhnicheskoĭ Fiziki, Vol. 28, No. 14, 2002, pp. 32–37.

The Photoluminescence of Amorphous Carbon in a-C:C_{60} Films Obtained by Fullerene C_{60} Deposition

A. V. Vasin, L. A. Matveeva, and V. A. Yukhimchuk

Institute of Semiconductor Physics, National Academy of Sciences of Ukraine, Kiev, Ukraine

e-mail: matveeva@isp.kiev.ua

Received February 14, 2002

Abstract—The results of experimental investigations of the carbon deposits obtained in the course of fullerene C_{60} sublimation are presented. It is shown that the films formed at a high deposition rate possess a composite structure representing a mixture of fullerenes and an amorphous carbon phase with a graphitelike short-range order. The films containing amorphous nonhydrogenated carbon possess photoluminescent properties analogous to those of hydrogenated amorphous carbon films with a high hydrogen content. The possible mechanism of photoluminescence of the composite carbon films is discussed. *© 2002 MAIK "Nauka/Interperiodica".*

As is known, films of amorphous carbon may exhibit photoluminescent properties. Intense photoluminescence is usually observed in the films of hydrogenated amorphous carbon (a-C:H) with a high hydrogen content (above 40 at.%) and a low concentration of paramagnetic centers (10^{19} cm^{-3} and below) [1–4]. The quantum yield of photoluminescence in such films increases with the degree of hydrogenation. The films of amorphous nonhydrogenated carbon (a-C) usually obtained by ion-plasma sputtering techniques are characterized by high defectness. According to the EPR data, the concentration of paramagnetic centers in such films is on the order of 10^{20} cm^{-3} and above [1, 2].

To our knowledge, no experimental data have been reported that would be evidence of the photoluminescence in the films of nonhydrogenated carbon. The absence, or at least a very low quantum yield of the photoluminescence in nonhydrogenated carbon films, is explained by a high concentration of defects playing the role of nonradiative recombination centers. The question as to which particular type of defects is responsible for the nonradiative recombination is still under discussion.

Below we present the experimental results showing evidence of the photoluminescence in nonhydrogenated a-C films obtained by vacuum deposition of fullerene C_{60}.

Experimental. A purified powder of fullerene C_{60} was sublimed from a tantalum effusion cell at an evaporator temperature of 600°C. The substrates were placed at a distance of 4 and 10 cm from the evaporator. This arrangement allowed the sample films to be obtained at various deposition rates under otherwise identical physical and technological conditions. The film growth rate was about 0.1 μm/min for the distant substrate and 0.5 μm/min for the nearest one.

The nanostructure of the deposits was studied by methods of Raman spectroscopy and photoluminescence. The Raman and photoluminescence (PL) spectra were measured at room temperature with the aid of a DFS-24 double-grating monochromator. The spectra were excited by an Ar^+ laser operating at a wavelength of 488 nm and measured using a cooled photoelectron multiplier operating in the photon counting mode.

Results and discussion. Typical Raman spectra of the carbon films are presented in Fig. 1. The high-frequency region of the spectrum of a film grown at a lower deposition rate displays three lines peaked at 1426, 1470, and 1578 cm^{-1} (Fig. 1, curve *1*), which can be assigned to the vibrational modes of fullerene molecules with H_g, A_g, and H_g symmetry, respectively.

The Raman spectrum of a film grown at a higher deposition rate is observed on the background of the PL signal and exhibits two broad bands with the maxima at 1410 and 1600 cm^{-1} and a narrow band at 1470 cm^{-1} (Fig. 1, curve *2*). The shapes and positions of the broad bands allow us to identify these signals with *D* and *G* bands characteristic of the films of amorphous carbon with a graphitelike short-range order. However, it is necessary to note a rather significant high-frequency shift and relatively small halfwidths (about 200 and 74 cm^{-1}, respectively) of these bands as compared to the typical values for a-C and a-C:H films [5]. The narrow line at 1470 cm^{-1} is probably a manifestation of the A_g vibrational mode of the fullerene molecules.

In this letter, we will not attempt to elucidate the physical mechanism responsible for the decomposition of fullerene molecules. However, some general remarks can still be made. The difference between the structures of films deposited at various distances from the evaporator can be due to a significant difference in the growth rate and/or in the thermal action of the evaporator as

such. We believe that the decomposition of fullerene molecules takes place on the substrate surface. If the fragmentation were proceeding in the effusion cell, the simultaneous deposition of a purely fullerene film on one substrate and an amorphous graphitelike phase on the other would be low-probable. Moreover, graphitelike clusters formed at the given evaporator temperature would be oxidized by oxygen in the residual atmosphere with the formation of volatile products, carbon mono- and dioxide.

Figure 2 shows a PL spectrum of the a-C:C_{60} composite film obtained at a higher deposition rate. The energy position (2.1 eV) and halfwidth (0.4 eV) of the PL band are close to the corresponding values for the films of hydrogenated carbon.

It was reported that high-quality single crystals of fullerenes exhibit PL in the region of 1.5–1.8 eV [6]. However, we did not observe PL signals in this spectral region in the samples studied. Based on the fact that the Raman spectroscopy confirms the presence of amorphous carbon in the films deposited at a higher rate, it is natural to attribute the PL observed at 2.1 eV to this very phase. At the same time, the presence of a PL signal in the films of amorphous nonhydrogenated carbon (a-C) is rather unexpected, since such films are usually characterized by a high concentration of defects playing the role of nonradiative recombination centers.

As is known, the problem of identifying defects in amorphous carbon and establishing their relationship with PL is extensively discussed. Despite the fact that the hydrogenated amorphous films of carbon and silicon possess very similar structures, the PL properties of these films are significantly different. In particular, the a-C:H films exhibit no correlation between the optical width of the forbidden band and the energy position of the PL band maximum. Nor do these carbon films exhibit a temperature variation of the PL intensity like that in the silicon films. Moreover, the recombination process in a-C:H films proceeds at a significantly higher rate than in a-Si:H. Taking into account these differences, it is hardly possible to use the PL mechanism adopted for a-Si:H, where the radiative recombination takes place on the electron states related to the dangling bonds. In addition, in a-C:H films, the problem is complicated by a large number of the possible configurations of structural defects.

In recent years, it was quite convincingly demonstrated [7, 8] that defect states in the tails of bands and at the Fermi level are related to the sp^2 clusters. In particular, it was shown that paramagnetic centers most probably represent the clusters with an odd number of π orbitals. From this standpoint, the PL observed in our amorphous nonhydrogenated carbon films can be explained as follows. The decomposition of fullerene C_{60} is accompanied by the formation of sp^2 clusters. As is known [9], it is energetically more favorable for the excited fullerene molecules to decay into clusters with even number of atoms. In the case under consideration,

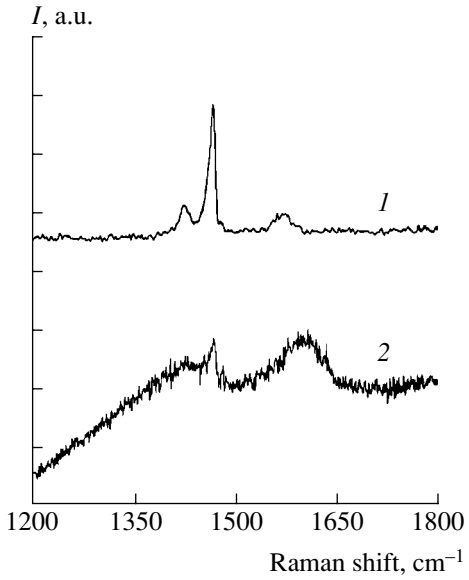

Fig. 1. The Raman spectra of carbon films grown at various deposition rates: (*1*) 0.1 μm/min; (*2*) 0.5 μm/min.

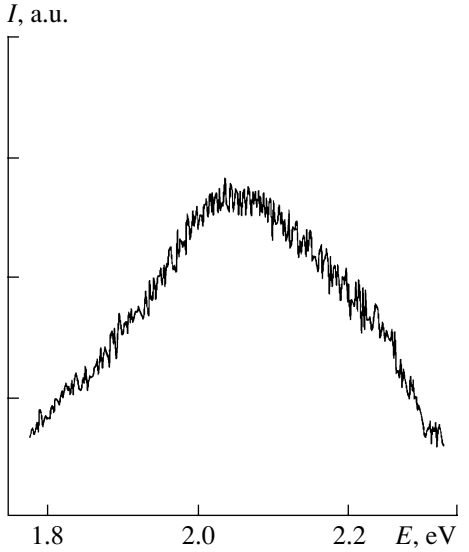

Fig. 2. The PL spectrum of an a-C:C_{60} composite film.

most of the graphitelike clusters formed from decomposed C_{60} molecules also contain even numbers of atoms. We may suggest that this factor determines a relatively low concentration of the nonradiative recombination centers and, hence, accounts for the PL observed in these films. However, a more reliably justified interpretation of PL in amorphous nonhydrogenated carbon requires additional investigation of the a-C:C_{60} films involving EPR spectroscopy and fundamental absorption-edge fine-structure measurements.

Conclusion. The results of our investigation lead to a conclusion that, during the growth of carbon films at high deposition rates, fullerene molecules may exhibit decomposition and form graphitelike amorphous nano-

clusters on an unheated substrate surface. It was demonstrated that films with this structure possess PL properties. It is suggested that the PL of a-C:C_{60} films is due to a relatively low concentration of nonradiative recombination centers. The low concentration of such defects can be explained by the fact that the graphitelike clusters are formed from the C_{60} molecules possessing an even number of atoms.

REFERENCES

1. S. Schute, S. Will, H. Mell, *et al.*, Diamond Relat. Mater. **2**, 1360 (1993).
2. F. Demichelis, S. Schreiter, and A. Tagliaferro, Phys. Rev. B **51** (4), 2143 (1995).
3. F. Giorgis, F. Giuliani, C. F. Pirri, *et al.*, Diamond Relat. Mater. **7** (2–5), 435 (1998).
4. J. Xu, W. Li, T. Ma, *et al.*, Appl. Phys. A **71** (6), 651 (2000).
5. R. O. Dillon, J. A. Woollam, and V. Katkanant, Phys. Rev. B **29** (6), 3482 (1984).
6. T. L. Makarova, Fiz. Tekh. Poluprovodn. (St. Petersburg) **35** (3), 257 (2001) [Semiconductors **35**, 243 (2001)].
7. M. Fanciulli, G. Fusco, and A. Tagliaferro, Diamond Relat. Mater. **6** (5–7), 725 (1997).
8. H. J. von Bardeleben, J. L. Cantin, A. Zeinert, *et al.*, Appl. Phys. Lett. **78**, 2843 (2001).
9. A. F. Ryabenko, V. E. Muradyan, P. V. Fyrsikov, *et al.*, in *Proceedings of the 7th International Conference on Hydrogen Material Science and Chemistry of Metals, Alushta, 2001*, p. 524.

Translated by P. Pozdeev

Technical Physics Letters, Vol. 28, No. 7, 2002, pp. 595–596. Translated from Pis'ma v Zhurnal Tekhnicheskoĭ Fiziki, Vol. 28, No. 14, 2002, pp. 38–42.

On the Magnetic Field Acting upon Moving Domain Walls in $(Bi,Yb)_3(Fe,Ga)_5O_{12}$ Garnet Ferrite Films

V. V. Randoshkin, V. A. Polezhaev, Yu. N. Sazhin, N. N. Sysoev, and V. N. Dudorov

Moscow State University, Moscow, Russia

United Laboratory of Magnetooptoelectronics, Institute of General Physics (Russian Academy of Sciences) and Mordvinian State University, Saransk, Mordvinia, Russian Federation

Received February 15, 2002

Abstract—The dependence of the domain wall velocity V on the magnetic field strength H in (111)-oriented $(Bi,Yb)_3(Fe,Ga)_5O_{12}$ single crystal garnet ferrite films is studied by the method of pulsed remagnetization at the point of angular momentum compensation. It is established that the acting field strength H is decreased by an effective internal magnetic field existing in the films studied. © *2002 MAIK "Nauka/Interperiodica".*

Some methods used for the measurement of the dynamic parameters of single crystal garnet ferrite (SCGF) films employ a pulsed magnetic field H_p applied along the easy magnetization axis [1, 2]. If the initial SCGF possesses a domain structure, the magnetic field strength acting immediately upon application of the field pulse is $H = H_p$. However, the H value monotonically decreases with time as the domain walls (DWs) move toward their equilibrium positions.

This disadvantage, as well as some others, are not inherent in the remagnetization method [3], according to which SCGF in the initial state is magnetized to saturation using a bias field H_b applied along the easy axis. Then the pulsed field is applied in the opposite direction, leading to the nucleation of a reverse magnetization domain (RMD) at a point or linear defect, and translation $X(t)$ of the DW is measured. At a sufficiently large distance from the RMD nucleation center ($X >$ 100 μm), the acting magnetic field strength is [3]

$$H = H_p - H_b. \quad (1)$$

Investigations of the domain dynamics in SCGFs of various compositions at the point of angular momentum compensation (AMC) showed that the initial portion of the $V(H)$ curve is linear and, if extrapolated, passes in the vicinity of the origin [4]. Subsequent behavior of the $V(H)$ curve depends on the dimensionless decay parameter α: for $\alpha > 1$, the first linear portion is followed by the second with a lower slope; for $\alpha < 1$, the linear portions are separated by a nonlinear region.

We studied dependence of the DW translation velocity on the acting magnetic field strength in SCGFs with the composition $(Bi,Yb)_3(Fe,Ga)_5O_{12}$ grown on (111)-oriented $Gd_3Ga_5O_{12}$ substrates [5]. The parameters of two samples are presented in the table, where h is the SCGF film thickness, w is the equilibrium strip domain width, H_0 is the bubble collapse field, H_K is the uniaxial magnetic anisotropy field, T_N is the Néel temperature, and μ is the DW mobility. The DW dynamics was studied by the method of pulsed remagnetization [2] using a high-speed photographic setup [6]. High-speed photography was used to monitor the DW translation of a RMD nucleated at a point defect.

Figure 1 shows the $V(H)$ curve for sample A (see table). As can be seen, the curve displays two linear portions separated by a nonlinear region, with the slope of the second linear portion (71 cm/(s Oe)) only slightly differing from that of the first (78 cm/(s Oe)). Assuming that $V(H)$ behavior is described by a one-dimensional theory of the DW motion, according to which the first and second linear portions (Fig. 1) reflect the stationary and precession DW motions, respectively, and using the relation [7, 8]

$$\alpha = (\mu/\mu_0 - 1)^{-1/2}, \quad (2)$$

we obtain $\alpha = 3.2$. However, for this dimensionless decay parameter, the nonlinear region on the $V(H)$ curve must be absent [8]. Therefore, the second linear

Room-temperature parameters of single crystal garnet ferrite films

Parameter	Sample	
	A	B
h, μm	11.4	13.2
w, μm	10.0	8.6
H_0, Oe	51	95
H_K, Oe	730	810
T_N, °C	129	122
μ, cm/(s Oe)	78	153

1063-7850/02/2807-0595$22.00 © 2002 MAIK "Nauka/Interperiodica"

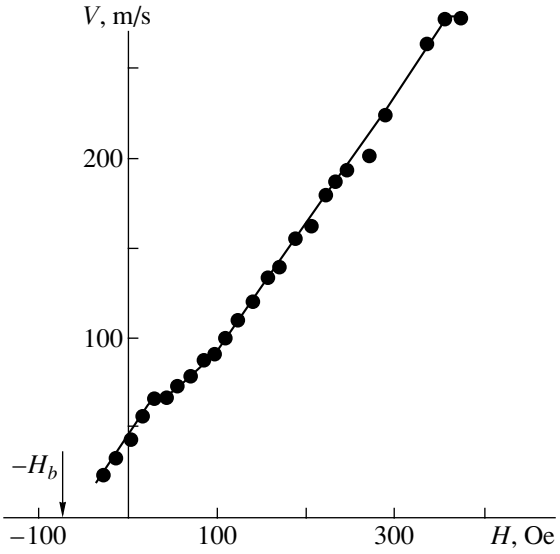

Fig. 1. Dependence of the DW velocity V on the acting magnetic field strength H for sample A (see table). The arrow indicates the bias field.

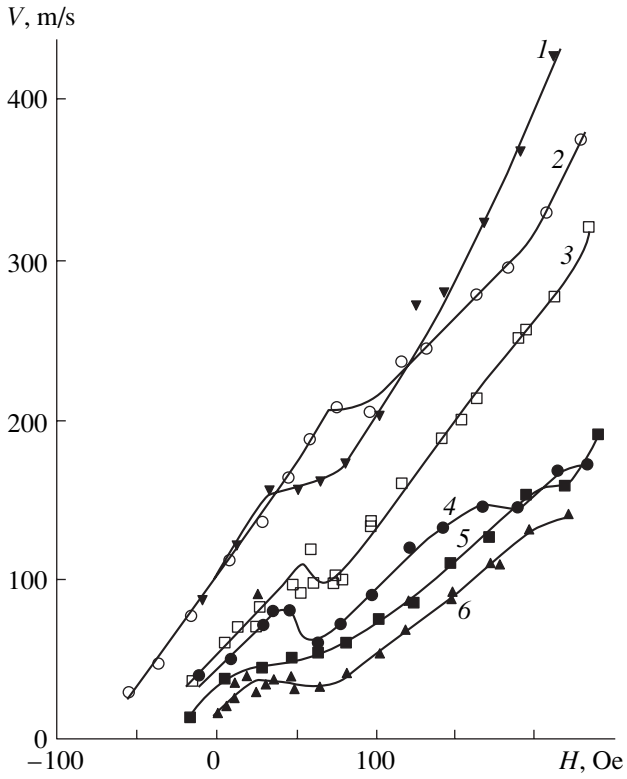

Fig. 2. The $V(H)$ curves for sample B (see table) measured for the bias field H_b = 100 Oe at various temperatures T = 18 (*1*), 30.5 (*2*), 44 (*3*), 60.5 (*4*), 78.5 (*5*), and 96.5°C (*6*).

portion (following the nonlinear region) is related to a mechanism of the DW motion with SW emission [9, 10]. Additional evidence for this mechanism is provided by the fact that a narrow region of fields between the nonlinear region and the second linear portion of the $V(H)$ curve features spatial distortions of the circular RMD analogous to those observed in the vicinity of the AMC point in Tm-containing SCGFs [7].

An unusual fact (see Fig. 1) is that the initial linear portion of the $V(H)$ curve begins in the region of negative H values. This can be explained by the presence of an effective internal magnetic field oriented in the same direction as the bias field. A source of this field can be, for example, a highly coercive interfacial layer the state of which is not affected by the pulsed magnetic field.

Figure 2 shows the $V(H)$ curves for sample B (see table) measured for the same bias field at various temperatures T. As the temperature grows, the $V(H)$ curves shift to the right. Therefore, the effective internal magnetic field strength, like the saturation magnetization, decreases with increasing SCGF temperature. As can be seen from Fig. 2, the most extended initial linear portion on the $V(H)$ curve is observed at T = 30.5°C, which is close to the AMC point. As expected [7], the DW mobility decreases when the temperature deviates from the AMC point.

Thus, we demonstrated that the pulsed remagnetization of a $(Bi,Yb)_3(Fe,Ga)_5O_{12}$ single crystal garnet ferrite is accompanied by the appearance of an effective internal magnetic field which decreases the acting field strength. This effective internal field decreases with increasing temperature.

REFERENCES

1. A. M. Balbashov, F. V. Lisovskiĭ, V. K. Raev, *et al.*, *Elements and Devices Based on Circular Magnetic Domains: A Handbook*, Ed. by N. N. Evtikhiev and B. N. Naumov (Radio i Svyaz', Moscow, 1987).
2. V. V. Randoshkin, Zavod. Lab. **62** (9), 32 (1996).
3. V. V. Randoshkin, Prib. Tekh. Éksp., No. 2, 155 (1995).
4. V. V. Randoshkin, Fiz. Tverd. Tela (St. Petersburg) **37** (3), 652 (1995) [Phys. Solid State **37**, 355 (1995)].
5. A. A. Aĭrapetov, M. V. Logunov, V. V. Randoshkin, and V. I. Chani, Pis'ma Zh. Tekh. Fiz. **18** (2), 74 (1992) [Sov. Tech. Phys. Lett. **18**, 53 (1992)].
6. V. V. Randoshkin, M. V. Logunov, and V. B. Sigachev, Prib. Tekh. Éksp., No. 5, 247 (1985).
7. V. V. Randoshkin and V. B. Sigachev, Fiz. Tverd. Tela (Leningrad) **32** (1), 246 (1990) [Sov. Phys. Solid State **32**, 138 (1990)].
8. V. V. Randoshkin, Fiz. Tverd. Tela (St. Petersburg) **37** (3), 652 (1995) [Phys. Solid State **37**, 355 (1995)].
9. V. V. Randoshkin and V. B. Sigachev, Fiz. Tverd. Tela (Leningrad) **28** (5), 1522 (1986) [Sov. Phys. Solid State **28**, 859 (1986)].
10. V. V. Randoshkin, Fiz. Tverd. Tela (St. Petersburg) **39** (8), 1421 (1997) [Phys. Solid State **39**, 1260 (1997)].

Translated by P. Pozdeev

Technical Physics Letters, Vol. 28, No. 7, 2002, pp. 597–598. Translated from Pis'ma v Zhurnal Tekhnicheskoĭ Fiziki, Vol. 28, No. 14, 2002, pp. 43–47.

Features in the Electromagnetic Field Intensity Distributions Near the Source in a Stochastic Discrete Medium

A. Yu. Vetluzhskiĭ

Buryatian Scientific Center, Siberian Division, Russian Academy of Sciences, Ulan-Ude, Buryatia, Russia

e-mail: vay@ofpsrv.bsc.buryatia.ru

Received January 25, 2002

Abstract—Spatial distributions of the average and coherent intensities of the electromagnetic field in a stochastic, strongly fluctuating discrete nonlossy medium are studied by experimental and theoretical methods. It is established that, at a certain density of the medium, the average field intensity near the source immersed into this medium can significantly exceed the value in the free space. © *2002 MAIK "Nauka/Interperiodica".*

Electromagnetic waves propagating in stochastically inhomogeneous media have been extensively studied. The interest of researchers in such problems is related to their wide applications, since most natural media can be considered as belonging to this type. Theoretical approaches to the description of such systems are numerous, examples being offered by the theory of radiation transfer, methods of the theory of multiple scattering, etc. [1, 2]. As a rule, practically significant results can be derived only within the framework of certain approximations. One of these assumes that the field source is located far from the region of the stochastic medium in which statistical characteristics of the field have to be determined.

This work aimed at the theoretical and experimental investigation of the spatial distribution of the field intensity near a source immersed into a stochastic, strongly fluctuating discrete medium.

Let us analyze the excitation of a structure composed of ideally conducting, infinitely long cylinders of a small electric radius $ka = 0.1$ (a is the geometric radius, $k = 2\pi/\lambda$, and λ is the wavelength). The cylinders are parallel to one another and, in the plane perpendicular to their axes, are randomly distributed with an average number density σ within a region of restricted area S. The probability that a cylinder occurs within a finite part of this region is described by the Poisson law. The field source is represented by an infinite filament carrying electric current, located at the center of the area occupied by the cylinders and parallel to their axes. Thus, we consider a two-dimensional problem.

Calculations of the average field intensity $I = \langle|E|^2\rangle$ and the coherent field intensity $I_c = |\langle E\rangle|^2$, where E is the field strength at the point of observation, were performed using the method of separation of variables [3], not posing restrictions on the mutual arrangement of cylinders and the field source. The field was represented as a sum of the known primary field and an unknown secondary field scattered from elements of the medium. The latter component was written in the form of infinite series in elementary wave functions with unknown coefficients. In particular, the field scattered from N elements was found in the form of a sum of N diffraction series, one of which was composed of the wavefunctions of one particular element, while the wave functions in the other series were expressed (using addition theorems) through eigenfunctions of the first element. The boundary conditions on the surfaces of each cylinder yielded infinite systems of equations with infinite numbers of variables representing the unknown coefficients in the expansions of wavefunctions. These equations were solved upon truncating the series based on the assumption of smallness of the geometric dimensions of structural elements.

The averaging was performed over an ensemble of 500 realizations of the arrangements of N elements. The number N of elements in each realization was varied according to the selected law of distribution of the probability of finding a given number of elements within the area S. The calculations yielded the field intensity as a function of the distance from the source for various densities of the structure and various dimensions of the region in which the elements were arranged.

It was established that, as expected, the coherent intensity decreases with increasing distance from the source. The rate of this decay grows with increasing number density of the elements. The results of calculations of the average field intensity are presented in the figure, where the abscissa represents the ratio R/λ (R is the distance from the source) and the ordinate represents the ratio of the average field intensity in the structure to the field intensity I_0 created by the source in the free space. In this case, the cylinders were arranged within a rectangular area of $12\lambda \times 7\lambda$ in the plane perpendicular to their axes. The spatial section of the field in each realization was performed along the large side of this area and passed through the center. Curves *1–3*

1063-7850/02/2807-0597$22.00

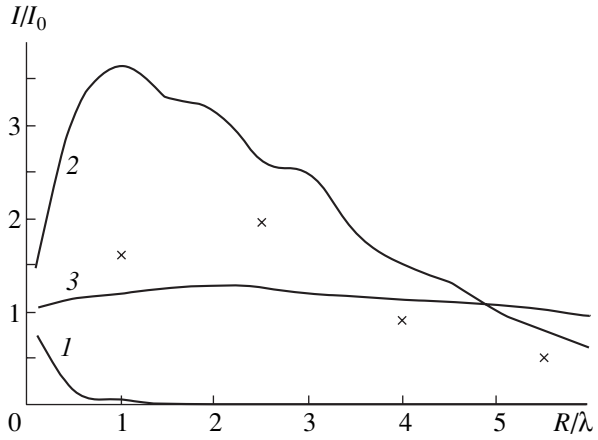

Theoretical (curves *1*–*3*) and experimental (crosses) field intensity profiles in a model stochastic discrete medium. See the text for explanations.

describe the average field intensity in the structures with the number densities of elements 4, 0.444, and 0.063 cm^{-2}, respectively.

The above results indicate that a source immersed into a high-density medium virtually does not radiate into the surrounding space. The field is concentrated in the immediate vicinity of the source, while the average field intensity within the structure is lower than that in the free space and rapidly decays with increasing distance from the source.

Of special interest are the results depicted by curve *2*. When the structure density decreases, the source begins to radiate the electromagnetic energy concentrated within a certain zone surrounding the source and does not spread over distant regions of the structure because of a sufficiently high number density of elements. It should be noted that maximum values of the average field intensity within the stochastic discrete structure are several times greater than the value in the free space.

As the density of the discrete structure decreases further (curve *3*), the distribution becomes more uniform over the whole structure and the relative field intensity tends to unity. This is a quite evident result [1] reflecting the fact that the total energy radiated by a source immersed into infinite stochastic nonlossy medium must be conserved.

The structure considered above possessed limited dimensions. In order to demonstrate applicability of the results to stochastic media, analogous calculations of the field intensity were performed for the cylindrical elements occupying regions of various dimensions, beginning with the case when the elements were arranged in a single row along the line connecting the source and the point of observation.

It was established that the behavior observed in the figure for the dependence of the spatial distribution of intensity on the density of the structure takes place only for sufficiently extended structures. For example, a characteristic maximum in curve *2* is manifested only for a transverse (relative to the field section) size of the structure of not less than three wavelengths. As the size of the structure increases, the field intensity at the point of maximum grows and tends to a certain constant level corresponding to the field intensity in an infinite medium.

The results of theoretical calculations were verified by the experimental investigation of the field intensity distribution in a structure representing a system of cylindrical metal elements mounted vertically on a conducting substrate. The measurements were performed at a frequency of 10 GHz. The role of a radiating source was performed by an open end of a waveguide placed at the edge of the structure, while the receiving antenna represented a quarter-wave dipole immersed into the structure. The experiments were performed at a structure density of 0.44 cm^{-2} for four distances between the radiating and receiving antennas. The results of these measurements are depicted in the figure by crosses representing averages over an ensemble of 50 realizations.

The observed discrepancy between calculation and experiment can be explained by a small number of realizations in the latter case, as well as by the fact that the source was located at the edge of the structure, rather than immersed into bulk. However, a qualitative agreement between the theoretical and experimental behavior is evident.

Thus, it was established that excitation of a stochastic discrete medium by an immersed source leads, at a certain density of the medium, to the formation of a region in which the average field intensity significantly exceeds the value in the free space. Similar effects must probably be observed in a three-dimensional case, for example, during the excitation of a medium composed of conducting balls possessing small electric radii.

REFERENCES

1. A. Ishimaru, *Wave Propagation and Scattering in Random Media* (Academic, New York, 1978; Mir, Moscow, 1981).
2. S. M. Rytov, Yu. A. Kravtsov, and V. I. Tatarskii, *Introduction to Statistical Radio Physics* (Nauka, Moscow, 1978), Vol. 2.
3. E. I. Ivanov, *Diffraction of Electromagnetic Waves on Two Bodies* (Nauka i Tekhnika, Minsk, 1968).

Translated by P. Pozdeev

Technical Physics Letters, Vol. 28, No. 7, 2002, pp. 599–601. Translated from Pis'ma v Zhurnal Tekhnicheskoĭ Fiziki, Vol. 28, No. 14, 2002, pp. 48–53.

The Effect of Nanosecond Ionization on the Characteristics of a Fast-Flow CO_2 Laser with Self-Sustained Discharge

L. M. Vasilyak, S. P. Vetchinin, P. G. Kadieva, D. N. Polyakov, and A. V. Khotina

Institute for High Energy Densities, Associated Institute for High Temperatures, Russian Academy of Sciences, Moscow, Russia

e-mail: lab852@ihed.ras.ru

Received February 4, 2002

Abstract—We studied the possibility of increasing the electric discharge stability, efficiency, and working range of a technological continuous-wave electric-discharge CO_2 laser at the expense of an additional pulsed ionization produced by nanosecond high-voltage pulses. *© 2002 MAIK "Nauka/Interperiodica".*

Experience gained from the practical use of high-power CO_2 lasers showed that the most promising sources of radiation for technological purposes are offered by lasers with an output power of ~1 kW. The simplest and most widely used method of pumping high-power lasers employs a stationary electric discharge. However, the domain of existence of a homogeneous glow discharge in molecular gases and related mixtures is limited with respect to the current as a result of the thermal contraction at high deposited energies. In order to expand the range of currents and pressures compatible with the volume discharge and to increase the lasing efficiency, it is possible to use the electroionization method of pumping, whereby the gas is ionized by an electron beam or by additional high-voltage pulses [1–3], while the lasing levels are excited by the induced discharge. Generalov *et al.* [4] studied the effect of an external ionization (analogous to a capacitive microwave discharge) produced by the high-voltage pulses (with an amplitude of about 20 kV) in a longitudinal dc discharge of a high-power technological laser of the "Lantan" type. The pulses were applied via additional electrodes. It was reported that the external ionization led to an increase in the limiting power supplied to the combined discharge and produced leveling of the electric field strength and electron density along the discharge.

We studied the effect of additional ionization, produced by high-voltage (up to 30 kV) nanosecond (FWHM, 50–150 ns) pulses applied at a repetition rate of 1 kHz, on the operation of a 1.5-kW CO_2 laser of the "Proton" type [5] employing a self-sustained transverse electric discharge and a closed gas pumping cycle.

The additional ionization pulses were applied to the working electrodes via blocking capacitors. The laser cathode had the form of a copper rod with a diameter of 1.4 cm and a length of 80 cm. The anode represented a 15-cm-wide plate of the same length spaced from the anode by 6 cm. Both electrodes were cooled with water. The capacitance of the storage capacitor of the pulse generator could be varied from 500 to 3000 pF. The stationary power supply unit was protected and decoupled by *LC* filters. The experiments were performed using the discharge in various CO_2–N_2–He mixtures with the $CO_2 + N_2$ partial pressure varied from 6 to 18 Torr. The working mixture was pumped across the discharge at a rate of 30–60 m/s. The discharge characteristics were studied in the self-sustained and combined regimes.

In the absence of ionizing pulses, no visible luminescence was observed in the interelectrode gap at a current below 4 A (emission took place only in the near-cathode layer). Application of nanosecond pulses induced homogeneous emission from the whole discharge gap. The additional ionization significantly expanded the range of stable dc discharge regimes, both ensuring stable operation at much smaller currents and eliminating the contraction at high currents. In the usual scheme, stable operation of a self-sustained discharge at reduced currents could be provided only by connecting large ballast resistors and increasing the supply voltage.

Figure 1 shows the current–voltage characteristics of discharge in various mixtures with a $CO_2 + N_2$ partial pressure of 8 Torr, a gas flow rate of 60 m/s, and a pulse generator storage capacitor of 1000 pF. Depending on the latter parameter, the dc voltage across the discharge gap at a fixed current may either increase or decrease. Accordingly, depending on the pulsed ionization parameters, we may either provide for a higher energy deposited in the discharge (with decreasing capacitance) which leads to an increase in the laser output power or allow the laser to operate at a higher current for the same dc voltage across the discharge gap (Fig. 1).

Additional pulsed ionization stabilizes the dc discharge, expands the range of pressures admitting stable operation of a self-sustained discharge without contraction, and allows a homogeneous discharge to be obtained on increasing the working gas pressure with-

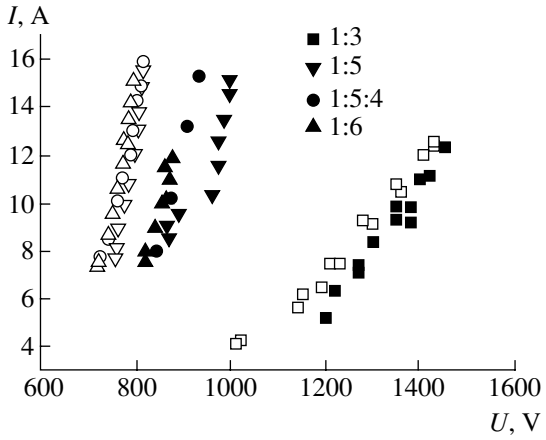

Fig. 1. Typical current–voltage characteristics of discharge in various CO_2–N_2–He mixtures with a CO_2 + N_2 partial pressure of 8 Torr. Open and filled symbols correspond to the combined and self-sustained discharge, respectively.

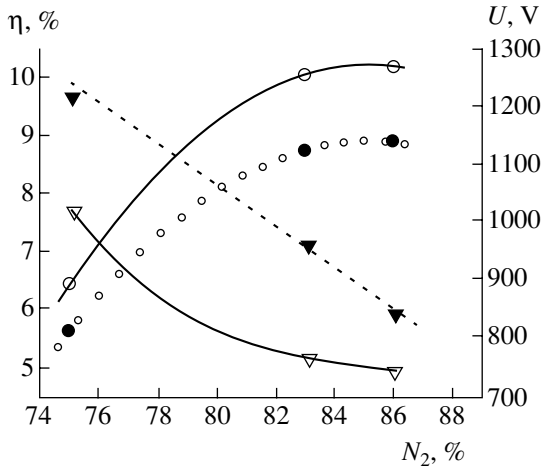

Fig. 2. The plots of maximum laser efficiency η (circles) and the corresponding voltage *U* (triangles) versus the nitrogen content in a helium-free molecular mixture (8 Torr). Open and filled symbols correspond to the combined and self-sustained discharge, respectively.

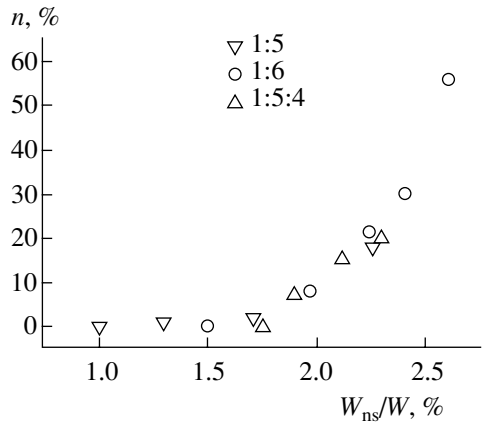

Fig. 3. A plot of the relative increase in the efficiency of a CO_2 laser pumped with a combined discharge versus the ratio of the nanosecond pulse source power (W_{ns}) to the self-sustained discharge power *W* for various working gas mixtures.

out decrease in the limiting current, thus increasing the energy deposited in the plasma. Since the high-voltage pulse amplitude is much greater than the breakdown voltage, these pulses produce significant ionization in the discharge gap without heating the gas. The nanosecond discharge takes place in the gap together with the ionization produced by the stationary discharge. For this reason, the discharge acquires the form of a high-speed ionization wave [6], which accounts for the most effective additional ionization. A minimum duration of the nanosecond pulse is determined by the time required for the ionization wave to travel across the gap at a characteristic velocity of 10^9 cm/s [6].

As can be seen from Figs. 1 and 2, the pulsed discharge leads to an increase in the electron density. A detailed numerical analysis of nonstationary processes in the glow discharge [7] showed that this is related to a sharp decrease in the rate of electron attachment in a strong electric field. Under these conditions, the lack of low-mobility negative ions results in their replacement by electrons moving from the cathode, after which both the conductivity and the discharge current increase (Fig. 1), The application of nanosecond pulses leads to a shift of the field strength toward lower values (Fig. 2, triangles) as compared to the case of a self-sustained discharge. The changed values provide for an optimum excitation of the vibrational lasing levels, thus increasing the laser efficiency (Fig. 2, circles).

A maximum gain in the laser efficiency for the mixtures studied was observed at a laser output power of 0.3–1 kW. The efficiency increases with the ratio of energy supplied from the pulsed source to that from the stationary discharge. The relative gain in the efficiency reaches 55% and exhibits a tendency to grow further (Fig. 3). As can be seen from Fig. 3, it is more expedient to use the working gas mixtures with increased nitrogen content. In a combined discharge, the main fraction of energy spent for an additional excitation of laser levels after the nanosecond pulse is supplied to the plasma from the dc source. The region of optimum *E*/*P* values is characterized by an almost linear dependence of the laser output power on the discharge current for various gas mixture compositions. In contrast to the case of a non-self-sustained discharge, a system operating in the combined regime features both the multiplication of electrons and the effective excitation of lasing levels between nanosecond pulses due to the self-sustained discharge. While the pulse repetition rate in the non-self-sustained discharge is small, there are time instants between pulses at which the electron density drops so strongly that the laser pumping is suspended. In our case, the laser is pumped continuously.

Thus, we demonstrated that the superposition of short (nanosecond) pulses onto a self-sustained discharge is a promising method which allows the efficiency of pumping of the CO_2 lasers with transverse discharge to be increased without modification of the laser design. Using this method, it is possible to

increase the laser efficiency, eliminate the discharge contraction, and provide for laser operation with simple (unsectioned) electrodes and helium-free (high-nitrogen) working gas mixtures. Using the combined regime improves the working characteristics of CO_2 lasers; increases the range of current control, facilitates discharge initiation; and increases stability and homogeneity of the discharge at high currents. Increasing discharge stability provides for a more homogeneous intensity distribution in the laser beam cross section.

REFERENCES

1. N. A. Generalov, V. P. Zimakov, V. D. Kosynkin, *et al.*, Kvantovaya Élektron. (Moscow) **9** (8), 1549 (1982).
2. V. G. Naumov and V. I. Shashkov, Kvantovaya Élektron. (Moscow) **4** (11), 2427 (1977).
3. A. P. Napartovich, V. G. Naumov, and V. I. Shashkov, Pis'ma Zh. Tekh. Fiz. **3**, 349 (1977) [Sov. Tech. Phys. Lett. **3**, 142 (1977)].
4. N. A. Generalov, V. P. Zimakov, I. G. Rudnyĭ, *et al.*, in *Laser Technology* (Inst. Fiziki Akad. Nauk LitSSR, Vilnius, 1988), Vol. 6, pp. 23–24.
5. A. I. Ivanchenko, V. V. Krasheninnikov, and A. G. Ponomarev, Élektrotekhnika, No. 11, 37 (1987).
6. L. M. Vasilyak, S. I. Kostyuchenko, N. N. Kudryavtsev, and I. V. Filyugin, Usp. Fiz. Nauk **164** (3), 263 (1994) [Phys. Usp. **37**, 247 (1994)].
7. V. V. Breev, S. V. Dvurechenskiĭ, and S. V. Pashkin, Teplofiz. Vys. Temp. **17** (2), 250 (1979).

Translated by P. Pozdeev

Technical Physics Letters, Vol. 28, No. 7, 2002, pp. 602–603. Translated from Pis'ma v Zhurnal Tekhnicheskoĭ Fiziki, Vol. 28, No. 14, 2002, pp. 54–58.

The Effect of Doping on the Electron Properties of Carbon Films

S. V. Simonov, S. Yu. Suzdal'tsev, and R. K. Yafarov

Saratov Branch, Institute of Radio Engineering and Electronics, Russian Academy of Sciences, Saratov, Russia

e-mail: pirpc@renet.ru

Received February 19, 2002

Abstract—It is demonstrated that doping with cadmium and treating in a low-energy argon plasma influence the electron emission properties of carbon films obtained in a microwave gas discharge plasma. The emission currents with a density of 0.3 A/cm^2 were obtained at an electric field strength in the diode gap of up to 7 V/μm.

At present, an important technological problem is to obtain nanocrystalline carbon films, representing carbon in various allotropic modifications and possessing a broad spectrum of physical properties. This task is related to the extensive search for pathways leading to the development of highly stable low-voltage cold electron emitters for flat displays and vacuum microwave electronics. As is known, significant factors decreasing the electron emission threshold are the topographical enhancement of electric field at the surface of such emitters and the properties of a nanostructural material such as the electric conductivity and negative electric affinity typical of many wide-bandgap semiconductors, in particular, diamond [1].

In this context, an important role is played by modification of the electron configuration and properties of the surface layers of nanocrystalline carbon films. This is confirmed, in particular, by the electron emission at an anomalously low voltage from "open" carbon nanotubes with a structure of the graphite type [2]. Carbon atoms occurring at the boundaries of nanostructures, as well as the atoms with dangling electron bonds occurring at the upper ends of carbon nanotubes, may possess a modified electron configuration whereby hybridization of the atomic bonds is different from the sp^2 type typical of ordinary graphite. This may lead to a negative electric affinity or, at least, to a significant decrease in the electron work function of the surface, thus favoring the electron emission.

In connection with this, our study aimed at finding technological means of modifying the surface layers of carbon films so as to obtain the desired electron properties of nano- and microcrystalline graphitelike film materials possessing a developed surface microtopography.

The carbon films were obtained by chemical vapor deposition (CVD) onto glass substrates from ethanol vapors in an electron cyclotron resonance microwave gas discharge in a setup described elsewhere [3]. The substrate temperature in a stationary regime was measured to within 5 K using a calibrated thermoresistor fixed on the substrate holder. The deposited film thicknesses were determined with the aid of a laser ellipsometer and an interference microscope. Microtopography of the sample film surface was studied in detail using a scanning atomic force microscope (AFM) and the film bulk structure was studied on a DRON-3.0 X-ray diffractometer.

The CVD of carbon films was conducted at an ethanol vapor pressure of 0.05 Pa in the gas discharge plasma with an accelerating potential of 300 V applied to the substrate holder. The substrate holder temperature was maintained at 350°C. The microwave power pumped to the plasma source was 250 W. The samples were prepared with a thickness of 0.25 μm. The X-ray diffraction data showed that the films consisted predominantly of a fine crystalline graphite phase with an interplanar spacing of d = 3.36 Å [4]. The resistivity of the sample films did not exceed several tens of Ω m.

In the experiments on doping the carbon films with a metal impurity (cadmium), a sample representing a carbon film on a glass substrate was mounted on a grounded holder in a vacuum–plasma setup and oriented perpendicularly to the plasma flow direction. The plasma-sputtered metal plate-target was placed at a distance of 1.5–2 cm from the substrate holder and inclined to make an angle of 120° to the sample surface. The experiments on sputtering Cd were performed in a microwave discharge plasma in an argon atmosphere at a pressure of 0.05 Pa with an accelerating potential of 80–90 V. The thickness of a sputter-deposited Cd layer was 100 nm. After terminating the deposition of cadmium and switching off the plasma source, cadmium was incorporated by diffusion into the film, for the purpose of which the sample was heated for 2 h at 180–200°C and a residual pressure of 1 Pa. After termination of the diffusion process, the carbon film was exposed to a beam of argon plasma in order to remove undiffused

1063-7850/02/2807-0602$22.00

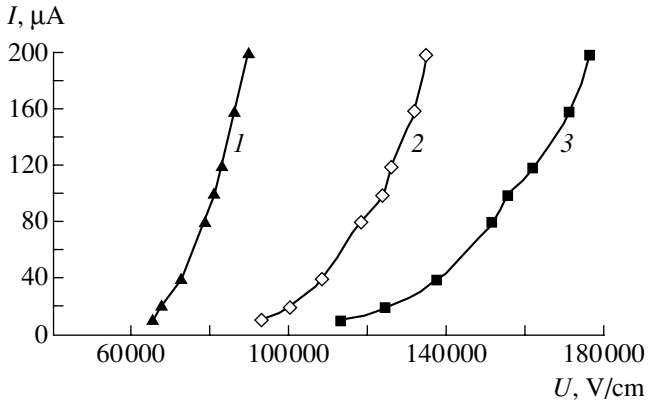

Fig. 1. Plots of cold electron emission current versus electric field strength measured in a microdiode structure with an interelectrode gap width of 120 μm for (*1*) a Cd-doped carbon film, (*2*) an initial carbon film, and (*3*) a film treated in an Ar plasma without doping.

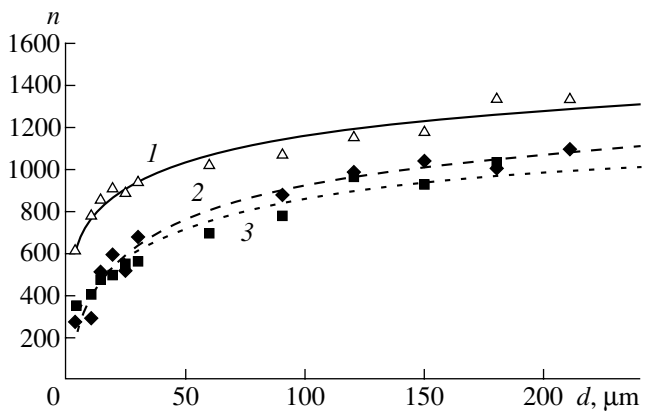

Fig. 2. Plots of the electric field enhancement coefficient *n* versus interelectrode gap width *d* for microdiodes with (*1*) a Cd-doped carbon film, (*2*) an initial carbon film, and (*3*) a film treated in an Ar plasma without doping.

cadmium from the sample surface. This was provided by applying an accelerating voltage of 150 V to the substrate holder for a time equal to that of the cadmium deposition stage.

The cold electron emission current was measured under high-vacuum conditions (10^{-5} Pa) in a diode structure where the distance between electrodes could be controlled to within 1 μm. The working surface of an anode made of an MPG-6 carbon-containing composite was 3 mm in diameter. The experiments devoted to studying the dopant effect on the electron properties of the emitting surface were performed with samples of three types, including (i) carbon films doped with Cd, (ii) those treated in an Ar plasma without doping, and (iii) the initial carbon films.

Figure 1 shows typical experimental curves of the cold emission current versus electric field strength in a microdiode with an interelectrode gap width of 120 μm, measured for the diodes with emitters of three types. As can be seen, doping the carbon films with cadmium significantly improves, while treatment in the low-energy argon plasma without doping markedly deteriorates, the emission properties.

Effects of the cadmium doping and the low-energy argon plasma treatment without doping on the coefficient of electric field enhancement in the microdiode gap is illustrated in Fig. 2. The field enhancement coefficients were calculated for carbon films of all three types assuming that the electron work function is unchanged and equal to the value for the corresponding carbon-containing material. The experimental results show that the field enhancement coefficient increases with the microdiode gap width and eventually attains a constant level depending on the regime of sample processing. The ion bombardment in a low-energy argon plasma does not change (or decreases) the electric field enhancement coefficient.

Doping the carbon film with cadmium rather significantly increases the field enhancement coefficient. This fact may be indicative of a decrease in the electron work function in the Cd-doped carbon films, since the surface roughness after accomplishing the doping and low-energy argon plasma treatment was virtually the same for the samples of all three types. This was established by examination of the surface of samples in a scanning AFM.

A comparative analysis of the current–voltage characteristics plotted in the Fowler–Nordheim coordinates showed that the electron work function of the Cd-doped carbon films is 20% lower than that of the initial films. In contrast, the electron work function of the carbon films treated in a low-energy argon plasma even increases by approximately 2% as compared to the initial material.

REFERENCES

1. J. Robertson, Thin Solid Films **296**, 61 (1997).
2. Y. Saito, K. Hamaguchi, K. Nata, *et al.*, Nature **389**, 555 (1997).
3. N. N. Bylinkina, S. P. Mushtakova, V. A. Oleĭnik, *et al.*, Pis'ma Zh. Tekh. Fiz. **22** (6), 43 (1996) [Tech. Phys. Lett. **22**, 245 (1996)].
4. A. Ubbelohde and F. Lewis, *Graphite and Its Crystal Compounds* (Clarendon, Oxford, 1960; Mir, Moscow, 1965).

Translated by P. Pozdeev

Technical Physics Letters, Vol. 28, No. 7, 2002, pp. 604–605. Translated from Pis'ma v Zhurnal Tekhnicheskoĭ Fiziki, Vol. 28, No. 14, 2002, pp. 59–63.

Radial Distributions of Rapidly Varying Currents and Fields in a Cylindrical Conductor

N. I. Kuskova[a] and S. I. Tkachenko[b]

[a] *Institute of Pulsed Processes and Technologies, National Academy of Sciences of Ukraine, Nikolaev, Ukraine*
e-mail: kvp@aip.mk.ua

[b] *Associated Institute for High Temperatures, Russian Academy of Sciences, Moscow, Russia*

Received February 13, 2002

Abstract—It is demonstrated that a rapid variation of the electric current in a cylindrical conductor is accompanied by redistribution of the current density and field strength in the conductor cross section. At the stage of increase, the current flows primarily in the surface layer, while at the stage of decrease, the current density can be maximum in internal regions of the conductor. At the time instants corresponding to the maximum current, the current density tends to a homogeneous distribution. © *2002 MAIK "Nauka/Interperiodica".*

As is known, rapid periodic variations of the electric current in a cylindrical conductor at a frequency ω, as described by the function $\exp(i\omega t)$, may give rise to a radial inhomogeneity in the current density. In the case of a strongly inhomogeneous distribution, the current flows only in a thin surface layer of the conductor, which is known as the skin effect [1].

Let us study the radial inhomogeneity arising in a cylindrical conductor upon rapid switching of the current on ($I \sim \exp(\beta t)$) or off ($I \sim \exp(-\beta t)$), where β is the current rise or decay coefficient. The process of diffusion of the longitudinal field E_z and the corresponding current density $j = \sigma E_z$ is conveniently described in the cylindrical coordinates by the equation

$$\frac{\partial^2 j}{\partial r^2} + \frac{1}{r}\frac{\partial j}{\partial r} = \mu\sigma\frac{\partial j}{\partial t}, \qquad (1)$$

where μ is the magnetic permeability and σ is the electric conductivity. The solution to Eq. (1) can be written as

$$j(r, t) = j(0, 0)\left(1 + \sum_{n=1}^{\infty}\frac{(\pm 1)^n}{2^{2n}(n!)^2}\left(\frac{r}{\delta}\right)^{2n}\right)\exp(\pm\beta t). \qquad (2)$$

Here, $\delta = (\mu\sigma\beta)^{-0.5}$; it is assumed that the initial time instant corresponds to $j(0, 0) \neq 0$.

Expression (2) represents two different functions describing the current buildup and decay. At the stage of increase,

$$j(r, t) = j(0, 0)\left(1 + \sum_{n=1}^{\infty}\frac{1}{2^{2n}(n!)^2}\left(\frac{r}{\delta}\right)^{2n}\right)\exp(\beta t). \qquad (3)$$

According to this formula, for $\delta \ll a$, the system features the skin effect. In the case of rapid decay,

$$j(r, t) = j(0, 0)J_0\left(\frac{r}{\delta}\right)\exp(-\beta t), \qquad (4)$$

where $J_0(r/\delta)$ is the Bessel function of the first kind. Thus, during a sharp decay under the conditions $a/\delta < 2.4$ ($a/\delta = 2.4$ is the first root of $J_0(a/\delta)$), the current flows in the whole cross section, while the current density in the surface layer decreases to zero.

The electric current passing in a real conductor leads to heating and expansion of the conductor. In such a case, diffusion of the magnetic field B_φ is described by the equation

$$\frac{\partial}{\partial r}\left(\frac{1}{r}\frac{\partial(rB_\varphi)}{\partial r}\right) = \mu\sigma\left(\frac{\partial B_\varphi}{\partial t} + \frac{\partial(vB_\varphi)}{\partial r}\right), \qquad (5)$$

where v is the radial expansion velocity. An analytical solution to Eq. (5) can be obtained provided that $v = ur$ and the conductor radius varies by the law $a = a_0\exp(ut)$. In this case,

$$B_\varphi(r, t) = B(a, 0)r\sum_{m=1}^{\infty}\left[\frac{(\pm 1)^n}{2^{2n}(n+1)!}\left(\frac{r}{\delta}\right)^{2n} \times\prod_{l=1}^{m}\left(\frac{2(k-1)u}{\beta} + 1\right)\right]\exp(\pm\beta t). \qquad (6)$$

Using formula (6) and taking into account that $j = (\mu r)^{-1}\partial(rB_\varphi)/(\partial r)$, we obtain the following expression

for the radial distribution of the current density:

$$j(r,t) = j(0,0)\left(1 + \sum_{n=1}^{\infty} \frac{(\pm 1)^n}{2^{2n}(n!)^2}\left(\frac{r}{\delta}\right)^{2n} \times \prod_{k=1}^{n}\left(\frac{2(k-1)u}{\beta} + 1\right)\right)\exp(\pm\beta t). \quad (7)$$

As can be seen from this relationship, expansion of the conductor significantly influences the current density distribution. For a real conductor, in which neither the current variation nor the material expansion can be described by exponents, the current density can be determined numerically. Previously [2], we obtained a weakly inhomogeneous distribution of the current density for which the current density in the decay stage ($dI/dt < 0$) exhibits a maximum at the center of the conductor. Apparently, radial distributions of the current density and the electromagnetic field must depend on the sign of the derivative dI/dt for the current $I(t)$ varying by any law.

The system of equations describing heating of a solid cylindrical conductor in a circuit with a capacitance C and inductance L is as follows [3]:

$$\frac{dm}{dt} = 0, \quad \rho\frac{dv}{dt} = -\frac{\partial P}{\partial r} - \frac{1}{2\mu r^2}\frac{\partial(r^2 B_\varphi^2)}{\partial r},$$

$$\rho\frac{d\varepsilon}{dt} = -P\frac{\partial(rv)}{\partial r} + \frac{1}{r}\frac{\partial}{\partial r}\left(\kappa r\frac{\partial T}{\partial r}\right) + \frac{j^2}{\sigma}, \quad (8)$$

$$\frac{d(\mu B_\varphi)}{dt} = \frac{\partial}{\partial r}\left(\frac{1}{\sigma r}\frac{\partial(rB_\varphi)}{\partial r}\right), \quad \frac{d^2(LI)}{dt} + \frac{d(RI)}{dt} + \frac{I}{C} = 0,$$

where m is the mass, P is the pressure, ε is the internal specific energy, T is the temperature, ρ is the density, κ is the thermal conductivity coefficient, and R is the resistance. Let us select the circuit parameters and conductor characteristics such that the current variations would possess an oscillatory character, for example, $U_0 = 80$ kV, $L = 5$ nH, $C = 20$ nF, $a_0 = 0.52$ mm, and $l = 2$ cm (conductor length). The conductor is made of a refractory metal with an initial electric conductivity of 10^5 Sm/m.

Depicted in Fig. 1, the time variation of the current determined by numerically solving the above equations has the shape of a weakly decaying sinusoid. The corresponding time patterns of the voltage and resistance are also shown in Fig. 1.

Figure 2 presents the radial distributions of the current density. As can be seen, the profile corresponding to the time $t = 12$ ns is sharply inhomogeneous, but then the system exhibits redistribution. For $dI/dt \longrightarrow 0$, the distribution at a certain time instant ($t > 15$ ns) becomes almost homogeneous. As expected, when the current decays, the current density is maximum at the center and drops to zero in the surface layer ($t \approx 24$ ns).

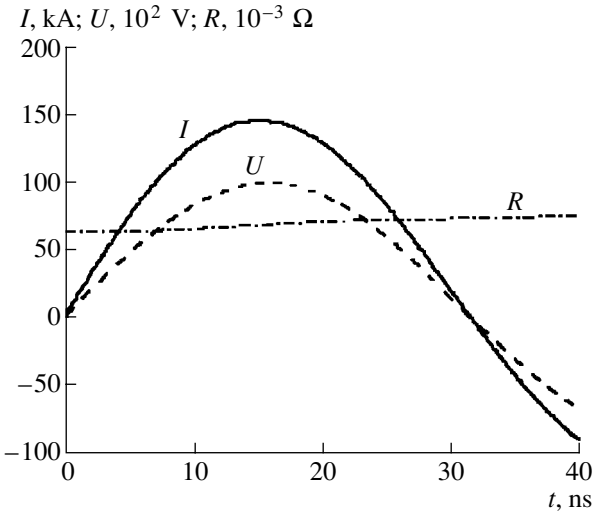

Fig. 1. Time variation of the current, voltage, and resistance in a cylindrical conductor.

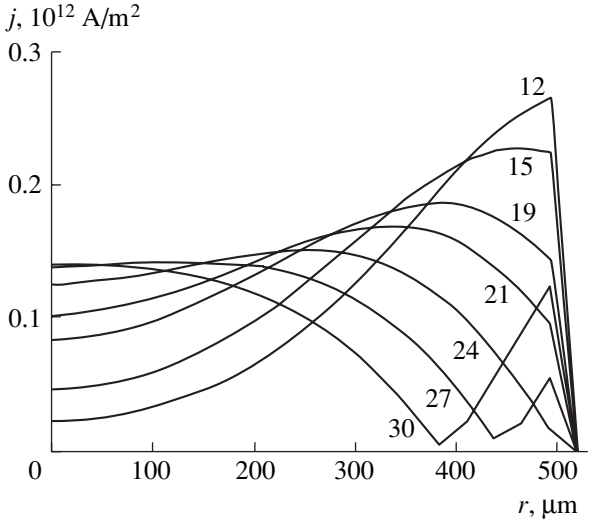

Fig. 2. Time evolution of the radial profiles of the current density in a cylindrical conductor (time instants in nanoseconds are indicated by figures at the curves).

REFERENCES

1. L. D. Landau and E. M. Lifshitz, *Course of Theoretical Physics*, Vol. 8: *Electrodynamics of Continuous Media* (Nauka, Moscow, 1982; Pergamon, New York, 1984).
2. N. I. Kuskova and S. I. Tkachenko, Pis'ma Zh. Tekh. Fiz. **22** (10), 30 (1996) [Tech. Phys. Lett. **22**, 401 (1996)].
3. N. I. Kuskova, S. I. Tkachenko, and S. V. Koval, J. Phys.: Condens. Matter **9**, 1675 (1997).

Translated by P. Pozdeev

Technical Physics Letters, Vol. 28, No. 7, 2002, pp. 606–607. Translated from Pis'ma v Zhurnal Tekhnicheskoĭ Fiziki, Vol. 28, No. 14, 2002, pp. 64–68.

A New Technology of Microporous Polymeric Membranes

V. F. Aristov, É. Yu. Buchin, and A. V. Postnikov

Institute of Microelectronics and Informatics, Russian Academy of Sciences, Yaroslavl, Russia

e-mail: imi.buchin@rambler.ru

Received March 18, 2002

Abstract—It is demonstrated that microporous membranes can be obtained by perforating polymer films with the aid of a needle cliche perforator. *© 2002 MAIK "Nauka/Interperiodica".*

Microporous polymeric membranes find increasing application in various fields of science and technology, such as microelectronics, biotechnology, medicine, ecology, pharmacy, food industry, and perfumery. Such membranes are used as filters or semitransparent spacers separating liquid and gaseous media with different compositions. At present, microporous membranes are obtained by irradiating a polymer film (Mylar, polycarbonate, etc.) with uranium fission products in a reactor or with heavy ions in an accelerator, followed by a special physicochemical treatment. Membranes fabricated by this method, called the track (nuclear) membranes, possess the following characteristics: base polymer film thickness, 10–25 μm; through hole diameter, 0.03–5 μm; porosity, 10–20%.

The existing technology of track membranes is rather complicated, which results in a high cost of the final products. For this reason, we attempted developing a simpler and cheaper technology of microporous polymeric membranes possessing technical characteristics analogous to those of commercial track membranes.

The proposed alterative technology is based on the use of a metal needle cliche perforator with preset parameters, which can be repeatedly used for perforating polymer films. The process of needle cliche preparation includes two steps: (i) the formation of a regular microporous matrix in an appropriate material; (ii) the manufacture of a metal replica of this matrix by an electroforming technique.

We selected silicon as the initial material for manufacturing a microporous matrix. This choice is determined by the fact that the process of pore formation in silicon by anodic etching in electrolytes containing hydrofluoric acid is known in sufficient detail. In particular, it was demonstrated that, using this method, it is possible to obtain regular porous structures on a micron scale [1, 2]. Such structures are usually obtained in a low-doped material with electron conductivity because only *n*-Si substrates allow the micron pores to form in a broad range of parameters of the electrochemical etching process. For the substrates of other types, the interval of parameters favoring the formation of micron pores is much narrower [3].

In order to obtain a regular porous structure, a pattern of seeding pits is formed initially on the surface of a silicon plate by a photolithographic technique in combination with anisotropic etching in potassium hydroxide. Under optimum etching conditions, the initial pores in a silicon plate possessing a crystallographic orientation (100) grow strictly perpendicularly to the semiconductor surface. The *n*-Si plates are etched in strongly diluted aqueous acid electrolytes. The process is enhanced by using a stimulating illumination which ensures the photoproduction of nonequilibrium holes participating in the etching process. The etched plate is illuminated from the rear side, which ensures that the holes drift strictly to the vertices of pores growing inward of the crystal from the seeding pits. The diameter of pores is determined by the anodic current density, while the depth is controlled by the etching time. Depending on the electric regime selected, the shape of pores can be varied so as to obtain a rectangular, conical, spindle, or other longitudinal cross sections.

The matrices were made from single crystal silicon wafers of KEF-20(100) grade. The ordered system of seeding pits was created either by a conventional photolithographic procedure or by laser lithography. The latter process employs a pulsed nitrogen laser with a radiation beam focused into a 3-μm spot scanning over the plate surface at a 6–8 μm step. The laser pulse energy was 1–5 μJ. The samples for anodic etching were cut to 40×40 mm. The etching process was conducted in a vertical electrochemical cell made of Teflon. The dry base anode had the form of a metal ring connected to a dc current source. The front surface of a silicon sample was in contact with an electrolyte (the electrolyte volume was 20 cm^3) so that etching took place within a circular region with an area of about 4 cm^2. The role of a cathode was performed by a platinum grid immersed into an electrolyte. The rear (dry) side of the sample was illuminated with the light of a 300-W tungsten incandescent lamp; the photocurrent was controlled by positioning the lamp. Since the anodic etching of silicon significantly depends on the temperature, a radiation-induced heating of the electrolyte was eliminated by placing a thermoinsulating

1063-7850/02/2807-0606$22.00

screen with an aperture between the lamp and the electrochemical cell. The electrolyte was a 4% aqueous solution of hydrofluoric acid. The anodic current density was maintained within 6–8 mA/cm^2, which provided for an etching rate of about 1.5 μm/min. After the electrochemical treatment, the sample was washed with water, etched for several seconds in a diluted potassium hydroxide solution, washed with water again, and dried in a stream of air. Using the above operations, we obtained a regular porous matrix with micron channels.

At the next stage, the silicon matrix was covered with a 0.6-μm-thick layer of nickel by vacuum deposition. Then the metal layer thickness was increased to 200 μm by an electrochemical deposition technique. In order to separate the metal replica from the porous matrix, silicon was completely dissolved in a concentrated potassium hydroxide solution. As a result, we obtained the required metal needle cliche. Figure 1 shows a micrograph of this structure imaged in a scanning electron microscope. As can be seen, the metal cliche exhibits a regular needle structure reflecting even finest details of the initial porous matrix. The number density of needles on the surface exceeded 10^6 cm^{-2}, the needle diameter and length being 4 and 25 μm, respectively. With the seeding pit patterns formed by laser lithography, the quality of porous matrices and, hence, of the resulting metal needle replicas was somewhat worse as compared to that provided by the initial photolithographic pattern. However, neither the absence of some needles nor a somewhat greater variance of their dimensions are critical for the final purpose.

Employed for perforating polymer films, the metal needle cliches manufactured as described above could withstand multiply repeated application. The embossing regime (temperature and load) depend on the mechanical properties of a polymer film. Figure 2 shows the micrograph of a microporous membrane made of a 15-μm-thick poly(methyl methacrylate) film. As can be seen, the membrane possesses a smooth surface and exhibits a small scatter of pore diameter, smooth pore edges, and a low number of defects. The membrane porosity was above 20% and the through channels had an average diameter on the order of 2 μm. These characteristics can be varied within broad limits by changing the doping level of initial silicon and the regime of anodic etching in the stage of porous matrix formation.

Thus, we demonstrated the possibility of obtaining relatively cheap microporous polymeric membranes possessing technical characteristics close to those of the track membranes.

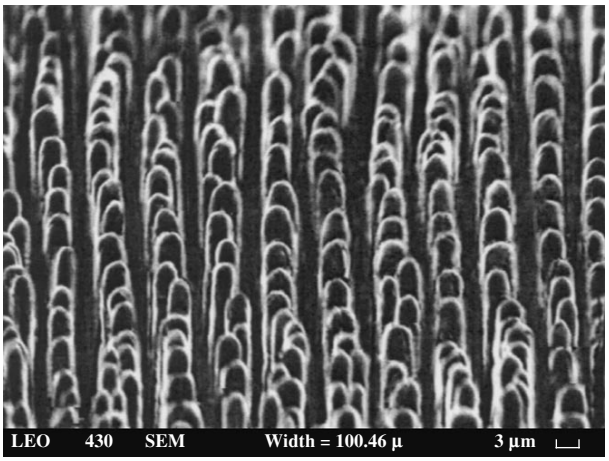

Fig. 1. An electron micrograph of a metal needle cliche studied in a scanning electron microscope.

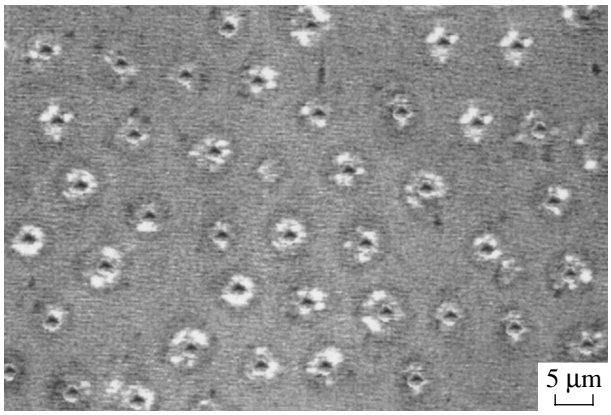

Fig. 2. The microphotograph of a microporous membrane made of a 15-μm-thick poly(methyl methacrylate) film.

REFERENCES

1. V. Lehmann, J. Electrochem. Soc. **140**, 2836 (1993).
2. V. V. Aristov, V. V. Starkov, L. G. Shabel'nikov, *et al.*, Opt. Commun. **161**, 203 (1999).
3. H. Föll, J. Carstensen, M. Christophersen, and G. Hasse, Phys. Status Solidi A **182**, 7 (2000).

Translated by P. Pozdeev

Technical Physics Letters, Vol. 28, No. 7, 2002, pp. 608–611. Translated from Pis'ma v Zhurnal Tekhnicheskoĭ Fiziki, Vol. 28, No. 14, 2002, pp. 69–76.

Superconducting Current in a Thin Film of Poly(phthalidylidene biphenylene)

A. N. Ionov[a], A. N. Lachinov[b], and R. Rench[c]

[a] *Ioffe Physicotechnical Institute, Russian Academy of Sciences, St. Petersburg, 194021 Russia*
[b] *Institute of Molecular and Crystal Physics, Russian Academy of Sciences, Ufa, Bashkortostan, Russia*
[c] *Institut für Experimentalphysik, Freie Universität Berlin, D-14195 Berlin, Germany*

Received March 14, 2002

Abstract—We report on the Josephson oscillations observed in a weak transverse magnetic field applied to a superconductor–poly(phthalidylidene biphenylene)–superconductor structure. The weak coupling is provided by point contacts at the polymer–superconductor interface. It is experimentally established that a characteristic scale of the Josephson oscillations depends on the I/I_c ratio, where I_c is the critical current. © *2002 MAIK "Nauka/Interperiodica".*

Previously [1], it was established that a thin ($d \cong 1\,\mu$m) film of poly(3,3'-phthalidylidene-4,4'-biphenylene) (PPB) (for the structural formula, see [2]) exhibits switching to a high-conductivity state in an electric field of relatively low strength ($E \approx 10^2$ V/cm, which is more than four orders of magnitude smaller than the breakdown voltage), provided that a small ($P < 10^5$ Pa) uniaxial mechanical pressure is applied to the metal electrodes so as to provide for a reliable metal–polymer contact. It was also found that, with metal electrodes in a superconducting state (S), the resistance of the S–PPB–S sandwich structure did not exceed 1 mΩ (which was the lower resolution limit of the equipment employed).

In this brief communication, we present experimental evidence that a superconducting current can flow in an S–PPB–S structure with a PPB film thickness of up to 1.0 μm.

The polymer layers in the sandwich structures represented PPB films with a thickness of about 1 μm, which were prepared by three methods:

1. A PPB layer was applied by spreading a 5–7% polymer solution in cyclohexanone cast immediately onto a polished electrode surface;

2. A PPB layer was applied onto a metal electrode surface by a centrifuging technique;

3. A free-standing PPB film was prepared preliminarily and then pressed between polished surfaces of the metal electrodes.

In the latter case, the free polymer films were obtained by a method traditionally employed in the sample preparation for electron microscopy. According to this, a polymer layer was deposited from a cyclohexanone solution onto a glass plate in a centrifuge. Then the substrate with the deposit was immersed into water where the film separated under the action of capillary forces. The film floating on the surface of water could be transferred either onto a metal electrode or onto a grid.

Irrespective of the method of preparation, the polymer films were kept in a thermal box for 60 min at 100°C in order to remove solvent residues. The polymer thickness d was determined with the aid of a MII-4 interference microscope. The electrodes were made of tin or niobium of ultrahigh purity (99.99%) in the form of disks with a thickness of 2.0 mm and a diameter of 3.0 mm (tin) and 5.0 mm (niobium). The electrodes were inserted into insulating frames having a common surface with the metal. The sample sandwich structures comprised a polymer film confined between two metal electrodes. The second electrode (free from the polymer layer) was pressed to the PPB film with a small load necessary to provide for a reliable electric contact. The condition of the electrode surface was monitored in the interference microscope, while certain selected sites could be studied in an atomic force microscope. The surface roughness height did not exceed 0.1 μm.

The conducting state of the samples was monitored by a method described previously [1], without employing an external source of voltage. The noise voltage across a sandwich structure during monitoring of the conducting state did not exceed 0.5 V/cm, which is almost seven orders of magnitude lower than the breakdown voltage for insulating polymer films. The low-temperature resistance was measured, and the effect of weak magnetic field on the conducting state was studied by a two-point-probe technique in a helium cryostat without special screening of the external magnetic fields. The weak probing magnetic field was generated by a superconducting coil and monitored by an InSb Hall sensor.

Figure 1 shows the temperature dependence of an Sn–PPB–Sn sandwich structure. At $T \le T_c$ (where T_c =

1063-7850/02/2807-0608$22.00 © 2002 MAIK "Nauka/Interperiodica"

3.7 K is the superconducting transition temperature of tin), the contact resistance of the PPB–Sn junction vanishes. As can be seen from Fig. 1, the drop in the sample resistance is not sharp, which is typical of systems with fine conducting channels and point superconducting contacts (S*o*S). At $T \le 3.6$ K, resistance is not detected, in agreement with our previous results [1]. Similar behavior of the resistance $R(T)$ in the structures with superconducting electrodes was observed for polyimide [3, 4] and poly(dimethylsiloxane) (PDMS) [5] films.

Let us consider the current–voltage (*I–U*) characteristics of the structures studied. Figure 2 presents the typical *I–U* curve measured at $T = 3.45$ K. As can be seen, the curve exhibits Josephson's shape, whereby no voltage drop is detected until the current reaches a certain critical value ($I_c = 1.25$ mA), at which the voltage $U = U_c$ appears in a jumplike manner. For $U > U_c$, the *I–U* curve shape is far from ohmic. This is characteristic of the resistive state, whereby both normal and superconducting electrons are present. The excess superconducting current can be estimated by extrapolating the *I–U* curve to $U = 0$ (Fig. 2).

A nonhysteresis behavior of the *I–U* characteristics at $T < T_c$ is characteristic of the cases when elements of the weak coupling between superconductors represent either point contacts or a normal metal featuring induced superconductivity due to the proximity effect (N_s) [6, 7]. In order to identify the type of weak coupling, we studied the temperature dependence of the critical current in the system. As is known, an analysis of the experimental $I_c(T)$ dependence in terms of the formula

$$I_c(T) = \text{const}(1 - T/T_c)^n \qquad (1)$$

allows the type of weak coupling to be identified upon determining the exponent *n*. For example, an SN_sS coupling corresponds to $n = 2$ [8], whereas the point contact between two superconductors corresponds to $n = 1$ [7].

The inset in Fig. 2 shows the experimental plot of $I_c(T)$ versus $1–T/T_c$ for the Sn–PPB–Sn structure studied. As can be seen, these data correspond with good accuracy to $n = 1$ for a parameter of $T_c = 3.72$ K, which is equal to the T_c of pure tin. Thus, an analysis of the *I–U* characteristic of the sandwich structure indicates that a weak coupling between superconductors is provided by a point contact, the role of which is performed by the polymer proper. The same result was obtained from an analysis of the *I–U* curve of a sandwich structure with a PDMS film [3]. For the sake of illustration, our system can be presented as S*o*P^s*o*S, which implies that charge carriers pass via a polymer by thin conducting filaments without energy dissipation. This is possible in two cases:

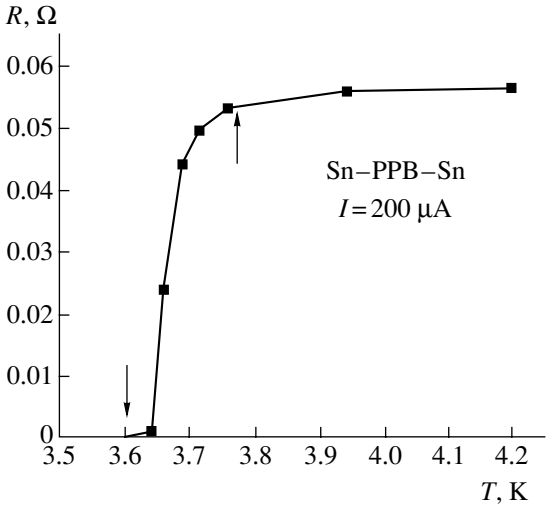

Fig. 1. Temperature dependence of the resistance of a Sn–PPB–Sn sandwich structure. Arrows indicate the interval of the superconducting transition.

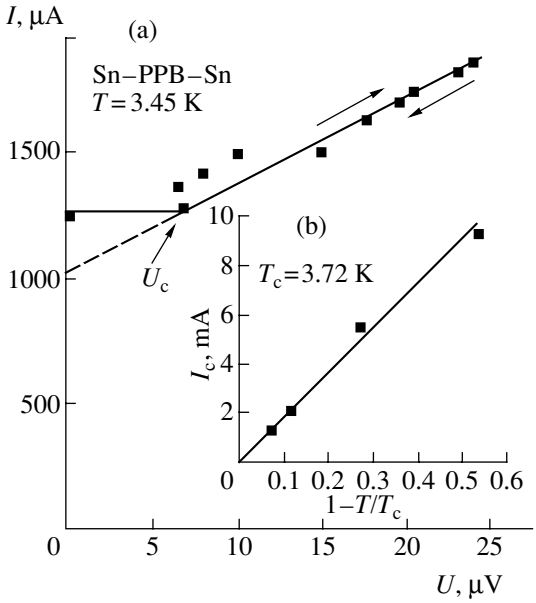

Fig. 2. The typical current–voltage characteristic of a S–PPB–S structure (S denotes superconductor) with PPB films prepared by various methods. The dashed line shows extrapolation to the excess superconducting current. The inset shows the experimental plot of $I_c(T)$ versus $1–T/T_c$ for the Sn–PPB–Sn structure.

1. For a ballistic transport of charge carriers, when the free path of a carrier between two collisions is $l \gg d$ [9–11].

2. For a superconducting polymer channel with $I_c^P > I_c^{SnoP}$, where I_c^P is the critical currents of the polymer channel and I_c^{SnoP} is that of the point contact between bulk superconductor and polymer.

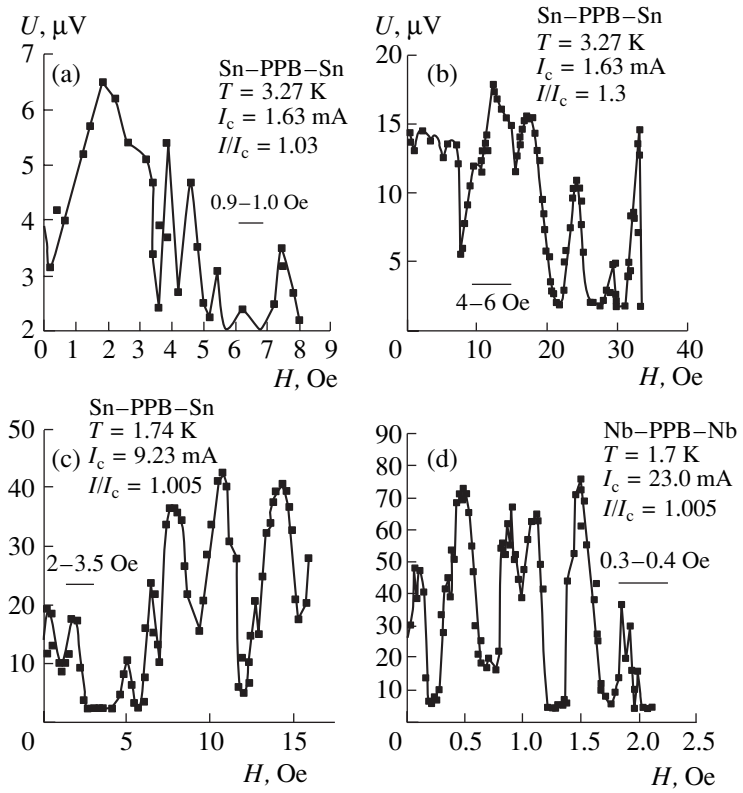

Fig. 3. The Josephson oscillations of voltage for S–PPB–S structures in a weak transverse magnetic field, related to a network of *N* parallel pairs of sequential Josephson contacts.

Evidence of the presence of Cooper pairs and multichannel conductivity in the polymer can be obtained by studying the Josephson effect in Sn–PPB–Sn and Nb–PPB–Nb sandwich structures. Figure 3 shows the Josephson voltage oscillations observed in these structures at $I \geq I_c$, depending on the strength of a weak magnetic field ($H \ll H_c$, where H_c is the critical magnetic field for a bulk superconductor) applied perpendicularly to the current direction. As can be seen from Fig. 3, the Josephson oscillations in the voltage as a function of the magnetic field strength exhibit a more complicated shape as compared to the Fraunhofer diffraction pattern typical of a single Josephson junction. It must be noted that the resistive state does not violate coherency of the wave functions of superconducting electrons at the Josephson contacts in the superconducting circuit. For this reason, when the external magnetic field varies, the voltage on this circuit oscillates with the same period as that of the critical current, although the phases of these oscillations are opposite [12]. The observed pattern of $U(H)$ oscillations is characteristic of *N* parallel Josephson junctions in a SQUID circuit, although it is important that our system does not exhibit a definite period of $U(H)$. A similar pattern of the $U(H)$ oscillations was observed at the grain boundaries in a high-temperature superconductor, where this behavior is due to a large number of parallel Josephson contacts [13].

A comparison of Figs. 3a and 3b shows that a growth in the I/I_c ratio leads to an increase in the characteristic scale of the $U(H)$ oscillations. As is known, the oscillation period for two parallel Josephson contacts is $\Delta H = \Phi_0/S$, where $\Phi_0 = 2.07 \times 10^{-15}$ Tm^2 is the magnetic flux quantum and *S* is the area crossed by the flux between two junctions. Taking into account that the polymer film thickness is about 1 μm, we may estimate the distance *L* between Josephson junctions. In the case presented in Fig. 3a for a Sn–PPB–Sn structure with $I/I_c = 1.03$, we obtain $L \approx 20$ μm, while $I/I_c = 1.3$ (Fig. 3b) yields $L \cong 5$ μm. In addition, the scale of oscillations depends on the superconductor contacting with PPB. For example, the scale of $U(H)$ oscillations in the Nb–PPB–Nb structure is smaller than that in the Sn–PPB–Sn system.

It should be noted that no Josephson oscillations in $U(H)$ are observed when one of the electrodes is in the normal state. This behavior, while not excluding the nondissipative transport of charge carriers, apparently excludes the superconducting state in the polymer due to the Cooper paring within the framework of the classical BCS theory. This conclusion is at variance with that drawn from the study of organic molecular superconductors such as pentazene [14, 15], where the superconducting state is probably due to the phonon mechanism of electron pairing described by the BCS theory.

Thus, the Cooper pair current is observed in the S–PPB–S sandwich structures studied, irrespective of the method used for the polymer film preparation. Elements of weak coupling are the point contacts at the polymer–superconductor interface. The nondissipative transfer of charge carriers through the polymer can be provided, for example, by a ballistic transport mechanism. The shape of the Josephson oscillations in the transverse magnetic field is indicative of a multichannel conductivity in the polymer film.

Acknowledgments. The authors are grateful to V.A. Zakrevskiĭ for discussion of the molecular structure of PPB and to V.M. Sarygina for her help in sample preparation.

This study was supported in part by the Russian Foundation for Basic Research (project no. 00-03-33060) and by the Presidium of the Russian Academy of Sciences (a grant within the framework of the "Low-Dimensional Quantum Structures" program).

REFERENCES

1. V. A. Zakrevskiĭ, A. N. Ionov, and A. N. Lachinov, Pis'ma Zh. Tekh. Fiz. **24** (13), 89 (1998) [Tech. Phys. Lett. **24**, 539 (1998)].
2. A. N. Lachinov, Sens. Actuators A **39**, 1 (1993).
3. A. N. Ionov, V. A. Zakrevskiĭ, and I. M. Lazebnik, Pis'ma Zh. Tekh. Fiz. **25** (17), 36 (1999) [Tech. Phys. Lett. **25**, 691 (1999)].
4. A. N. Ionov, V. A. Zakrevskii, J. M. Lazebnik, *et al.*, cond-mat/0006016 (2000).
5. A. N. Ionov and V. A. Zakrevskiĭ, Pis'ma Zh. Tekh. Fiz. **26** (20), 34 (2000) [Tech. Phys. Lett. **26**, 910 (2000)].
6. L. Solymar, *Superconductive Tunnelling and Applications* (Chapman and Hall, London, 1972; Mir, Moscow, 1974).
7. L. G. Aslamazov and A. I. Larkin, Pis'ma Zh. Éksp. Teor. Fiz. **9** (2), 150 (1969) [JETP Lett. **9**, 87 (1969)].
8. P. G. De Gennes, Rev. Mod. Phys. **36**, 225 (1964).
9. M. Thomas, H. R. Blank, K. C. Wong, *et al.*, Phys. Rev. B **58** (17), 11676 (1998).
10. R. Landauer, Philos. Mag. **21**, 863 (1970).
11. R. De Picciotto, H. L. Syorner, L. N. Pfeiffer, *et al.*, Nature **51**, 411 (2001).
12. M. N. Omar and R. De Bruyn Ouboter, Commun. Leiden **32** (352b), 2044 (1966).
13. E. A. Early, R. L. Steiner, A. F. Clark, *et al.*, Phys. Rev. B **50** (13), 9409 (1994).
14. J. H. Schoen, H. Y. Hwang, Ch. Kloc, *et al.*, Science **292**, 252 (2001).
15. J. H. Schoen, Appl. Phys. Lett. **79** (14), 2208 (2001).

Translated by P. Pozdeev

Technical Physics Letters, Vol. 28, No. 7, 2002, pp. 612–614. Translated from Pis'ma v Zhurnal Tekhnicheskoĭ Fiziki, Vol. 28, No. 14, 2002, pp. 77–82.

Nanodimensional Changes in the Structure of Ion-Irradiated Silicon Crystals at a Depth Exceeding the Ion Range

A. N. Kiselev, V. L. Levshunova, V. A. Perevoshchikov, and V. D. Skupov

Nizhni Novgorod State Technical University, Nizhni Novgorod, Russia

Physicotechnical Research Institute, Nizhni Novgorod State University, Nizhni Novgorod, Russia

e-mail: vap@nifti.unn.ru

Received February 26, 2002

Abstract—Atomic force microscopy reveals changes in the surface micromorphology of ion-irradiated silicon crystals in the course of dynamic chemical polishing and selective etching to a depth significantly exceeding the range of 40-keV Ar^+ ions. *© 2002 MAIK "Nauka/Interperiodica".*

The phenomenon of anomalously deep structural changes in solids implanted with medium-energy ions, called the long-range effect, is still under extensive discussion. The main reason for ambiguity is insufficient volume of direct experimental evidence about structural changes in the ion-irradiated crystals beyond the ion stopping range. Most of the known data concerning the long-range effect were obtained by indirect methods. In this context, we studied the structure of irradiated crystals of nondislocated silicon by method of atomic force microscopy (AFM) in the course of dynamic chemical polishing and selective etching of the samples.

The investigation was performed on 630-μm-thick (111)-oriented single crystal silicon samples cut from wafers of KEF-15 grade. The samples were irradiated to a total fluence of 2.8×10^{16} cm^{-2} with 40-keV Ar^+ ions at a beam current density of less than 3 $\mu A/cm^2$. Prior to irradiation, the surface of samples was partly coated with an 0.7-μm-thick layer of amorphous silicon in order to check for the possibility of stimulated effects analogous to those studied previously [1, 2]. In addition to the ion-irradiated samples, we studied the control samples of initial crystals and the unirradiated crystals coated with amorphous silicon. The latter samples were studied in order to determine the effect of elevated temperature (T = 420 K), developed during deposition of the amorphous layer, on the single crystal substrate structure.

The surface micromorphology of the silicon samples was studied in the course of layer removal by etching in an HNO_3–HF–CH_3COOH (40 : 1 : 1) solution at a rate of 1 μm/min and upon treatment in an HF–CrO_3 (1 : 1) selective etchant. The measurements were performed in a TMX-2100 Accurex scanning probe microscope operated in the noncontact AFM mode. The samples were studied from both the ion-irradiated front (I) and the unexposed rear (II) sides.

The results of experiments showed that the deposition of an amorphous silicon layer and the ion irradiation smoothed the surface by reducing the microroughness height and decreasing the lateral microrelief dimensions by a factor of 1.9–3.2. On the free (uncoated) surface of initial crystals, these parameters were 2.6–3.3 and 100–200 nm, respectively. However, when the irradiated crystals with an amorphous silicon layer were etched to a depth of 1.5–2.0 μm, the AFM examination of both I and II sides revealed a sharp increase in the microroughness height and the lateral microrelief size variance (at a certain decrease in the average size).

Typical AFM topographs of the surface microrelief observed on both sides of silicon crystals etched down to a depth of 15 μm are presented in the figure. The surface of initial (unirradiated) crystals etched to any depth contained microdepressions with a diameter of 40–160 nm, the surface density of which varied from 10^{19} to 10^{12} cm^{-2} (Ia, IIa). These depressions are probably formed as a result of dissolution of the growth microdefects of C or D type in the course of selective etching [3]. The deposition of an amorphous silicon layer and the ion irradiation lead to an increase in the dimensions of etching-induced microdepressions, which is more pronounced on the rear side (cf. topographs Ib–Id and IIb–IId). Note that the presence of an amorphous silicon layer during irradiation results in smaller changes in the crystal micromorphology on side I as compared to those on side II (cf. topographs Id and IId), the latter being comparable to the structural changes observed under the irradiated free surface (cf. topographs Ia and IIc).

In all regions of the crystals upon irradiation, the AFM examination revealed rather large depressions with a depth of up to 50 nm and a lateral size of 0.6–0.8 μm, frequently of irregular shape. This might be evidence that these depressions represent the ion-irradiation-

1063-7850/02/2807-0612$22.00

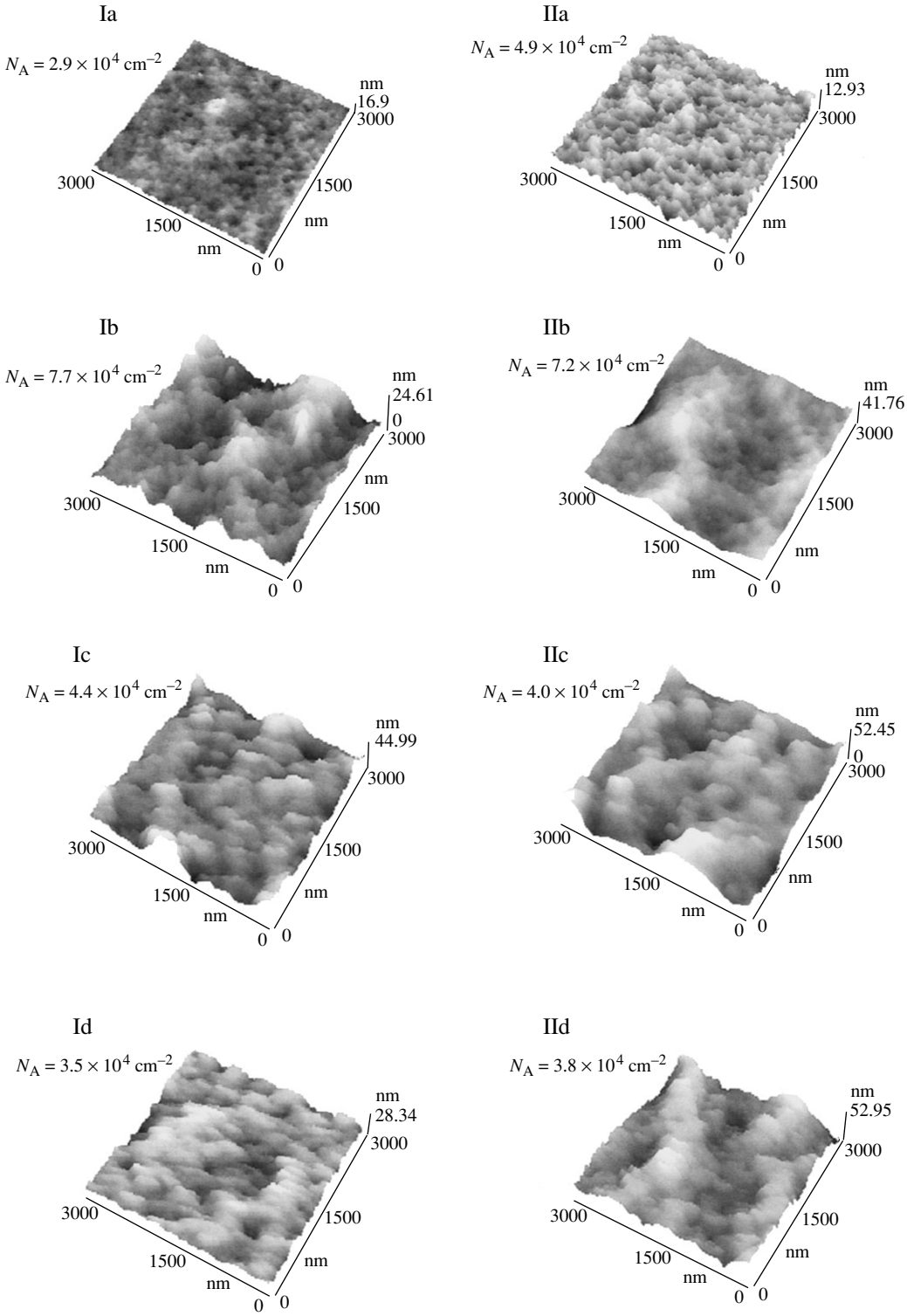

AFM microtopographs of the silicon single crystals etched to a depth of 15 μm from both front (I) and rear (II) sides: (a) in the initial (unirradiated) state; (b) upon amorphous silicon layer deposition; (c) after ion irradiation through the free surface; (d) after ion irradiation through the amorphous silicon layer. N_A is the A type defect density determined by direct metallographic techniques.

modified clusters of A and B types. According to the scanning probe microscopy data, the number density of such defects is on the average 10^6–10^7 cm^{-2} and may vary depending on the crystal treatment similarly to the A type defect density N_A determined by direct metallographic techniques on the etching patterns. The N_A values for the samples etched to a depth of 15 μm are indicated in the figure.

An analysis of variations in the surface micromorphology and microdefect structure of samples in the course of layer-by-layer etching suggests that the substrate heating taking place during the amorphous silicon layer deposition leads to a partial dissolution of the impurity atmospheres shielding the microdefects. This leads to an increase in the rate of dissolution of these defects in the selective etchant, which results in a growth of the surface microroughness. Subsequent irradiation not only enhances this process, but favors dissolution of the microdefects as well (due to the action of noneqiulibrium intrinsic point defects and elastic waves generated in the ion stopping range) [2, 4–6]. In the material ion-bombarded through the amorphous layer, the flux of point defects decreases and the structural changes become less pronounced. On the rear side of the samples, the action of elastic waves accompanied by the point defect production [2, 5] leads to almost the same effects for the samples irradiated through the free surface and the amorphous layer (cf. topographs IIc and IId in the figure).

The above results give us ground to ascertain that anomalously deep structural changes in the crystals upon ion irradiation are related to transformations in the subsystem of crystal microdefects, which are manifested by changes in the defect size and density spectra. A decrease in N_A observed for the samples upon preliminary low-temperature annealing during deposition of the amorphous silicon layer and subsequent irradiation through this layer indicates that this phenomenon can be used for gettering the clusters of defects in crystals.

REFERENCES

1. A. V. Kulikov, V. A. Perevoshchikov, V. D. Skupov, *et al.*, Pis'ma Zh. Tekh. Fiz. **23** (13), 27 (1997) [Tech. Phys. Lett. **23**, 507 (1997)].
2. V. A. Perevoshchikov and V. D. Skupov, Pis'ma Zh. Tekh. Fiz. **25** (8), 50 (1999) [Tech. Phys. Lett. **25**, 315 (1999)].
3. M. G. Mil'vidskiĭ, *Semiconductor Materials in Modern Electronics* (Nauka, Moscow, 1986).
4. A. G. Ital'yantsev and V. N. Mordkovich, Fiz. Tekh. Poluprovodn. (Leningrad) **17** (2), 217 (1983) [Sov. Phys. Semicond. **17**, 140 (1983)].
5. P. V. Pavlov, Yu. A. Semin, V. D. Skupov, *et al.*, Fiz. Tekh. Poluprovodn. (Leningrad) **20** (3), 503 (1986) [Sov. Phys. Semicond. **20**, 315 (1986)].
6. E. S. Demidov, N. D. Latysheva, V. A. Perevoshchikov, *et al.*, Neorg. Mater. **36** (5), 1 (2000).

Translated by P. Pozdeev

Technical Physics Letters, Vol. 28, No. 7, 2002, pp. 615–617. Translated from Pis'ma v Zhurnal Tekhnicheskoĭ Fiziki, Vol. 28, No. 14, 2002, pp. 83–87.

Helium Ion Bombardment Induced Amorphization of Silicon Crystals

V. F. Reutov and A. S. Sokhatskiĭ

Flerov Laboratory of Nuclear Reactions, Joint Institute for Nuclear Research, Dubna, Moscow oblast, 141980 Russia

e-mail: sohatsky@nrsun.jinr.ru

Received February 28, 2002

Abstract—The possibility of amorphization of a silicon crystal bombarded at room temperature with helium ions is studied by monitoring structural changes in the target crystal by means of transmission electron microscopy. Thin free-standing Si(100) plates were irradiated from the plane edge ({011} face) with 17-keV He^+ ions in a dose range from 3×10^{16} to 3×10^{17} cm^{-2}. It was established that amorphization of the silicon crystal takes place for a total fluence exceeding 10^{17} cm^{-2}, provided that the ratio of the point defect production rate to the rate of helium introduction into silicon exceeds 90 displacements per He atom. © *2002 MAIK "Nauka/Interperiodica".*

The phenomenon of amorphous layer formation in a silicon crystal substrate under the action of ion irradiation is well known and widely used in modern silicon technology. It has been established that silicon can be readily amorphized by bombardment with medium-mass ions. According to Morehead and Crowder [1], the lightest particles capable of producing room-temperature silicon amorphization are boron ions.

Such experimental facts determined the principal mechanism of the radiation-induced amorphization of semiconductors, according to which the amorphous regions are formed in the atomic collision cascades. However, experiments on the irradiation of silicon crystals at a temperature below 25 K with 2-MeV electrons to a total dose corresponding to five displacements per atom (dpa) showed that amorphization is also possible for radiation-induced point defect production [2]. Here, the low temperature of irradiation ensured a low rate of the pair recombination of defects, the accumulation of which favored the amorphization of silicon.

A decrease in the rate of recombination of the radiation-induced point defects can be also provided by the trapping (blocking) of defects of a certain type, for example, by the trapping of vacancies at impurity atoms. It was demonstrated [3–5] that the atoms of impurity (helium) effectively interact with the vacancies, thus preventing these defects from recombination with the interstitial defects. In connection with this, there are grounds to believe that conditions favoring the amorphization of silicon can be provided by bombarding a silicon target with helium ions. A necessary condition probably consists in ensuring a certain relationship between the rate of defect production ($\dot{C}_d$) and the rate of helium introduction ($\dot{N}_{\mathrm{He}}$) in silicon, as determined by the ratio $K = \dot{C}_d / \dot{N}_{\mathrm{He}}$ (representing the number of displacements per He atom), naturally provided that the sufficient condition of reaching a certain concentration of helium atoms is also satisfied.

It should be noted that the above conditions can be satisfied in ion-irradiated crystals only within a certain part of the ion range, since the K value will vary in the depth of the ion implantation region because of a mutual spatial shift of the defect and implant profiles. For a low-energy (below 100 keV) ion implantation, K monotonically decreases from ~150 at the bombarded crystal surface to zero at a depth equal to the ion range. At the radiation damage density peak, K amounts to about 70.

According to the published data concerning the radiation defect production in silicon, amorphization was never observed in Si crystals irradiated to a total fluence below 10^{17} cm^{-2} [5]. On the other hand, Siegele *et al.* [6] reported that amorphization took place in a thin buried layer of silicon irradiated with 20-keV He^+ ions to a greater dose of 2.5×10^{17} cm^{-2}. This fact suggests that the K value reached in this layer was sufficient for the formation of defects responsible for the amorphization of silicon, although their accumulation in a necessary amount required implantation of a considerable (up to 10 at. %) concentration of helium.

Thus, assuming that the parameter K really controls the formation of defects responsible for amorphization, meeting the conditions of silicon amorphization at a lower fluence requires modifying the experimental conditions so as to ensure that the relative concentration of the radiation-induced Frenkel pairs would grow relative to the implant concentration. We believe that such conditions can be realized in a thin silicon crystal plate irradiated from the edge face [7]. In this geometry, the

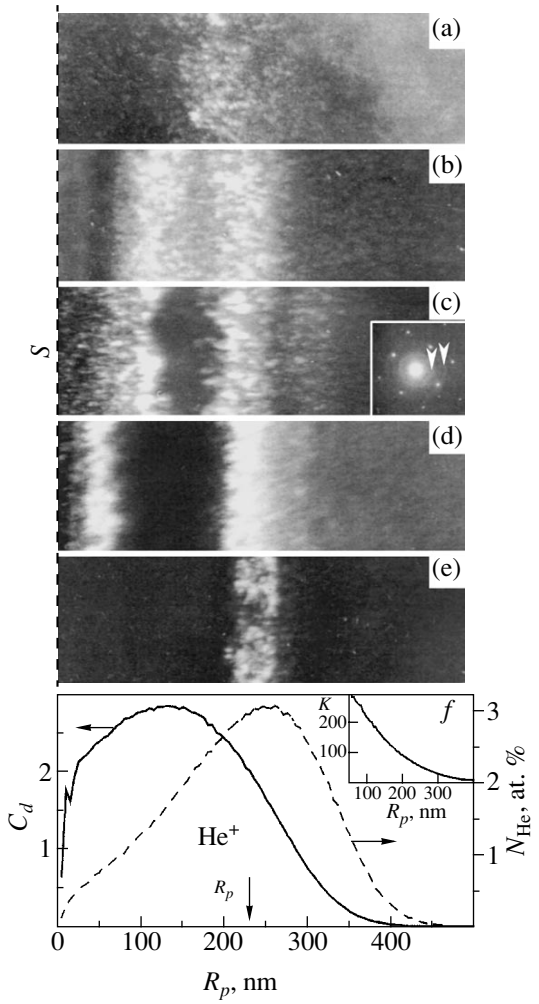

Fig. 1. Dark-field (g = 220) TEM micrographs illustrating the dose dependence of structural changes in a silicon plate with a thickness of t = 150 nm irradiated from the edge face (S) with 17-keV He^+ ions: (a) the appearance of radiation defect pileups at a fluence of 3×10^{16} cm^{-2}; (b) a preamorphization state of Si in the region of defect accumulation at a fluence of 5×10^{16} cm^{-2}; (c, d) the formation and growth of a buried amorphous layer at a fluence of fluence of 10^{17} and 1.5×10^{17} cm^{-2}, respectively (the inset shows an electron microdiffraction pattern of the damaged region, with arrows indicating the rings passing through Si(111) and (220) reflections); (e) expansion of the amorphous layer to the bombarded edge surface at a fluence of 3×10^{17} cm^{-2}; (f) calculated depth–concentration profiles of the radiation defects C_d (in dpa units) and implanted He atoms for a fluence of 10^{17} cm^{-2}, scaled to the above micrographs; the inset shows a plot of $K = \dot{C}_d / \dot{N}_{He}$ (in displacements per He atom) versus He^+ ion projected range R_p.

required increase in K can be reached due to a decrease in the flux of He^+ ions along the projected range as a result of their scattering with escape from the sample.

We studied the role of parameter K in the amorphization of silicon by low-energy He^+ ions using thin free-standing Si(100) plates irradiated from the plane edge ({011} crystal face) [7]. The plate thickness t was selected so as to provide that the sample would be transparent for the electron beam of a transmission electron microscope (TEM) operated at an accelerating voltage of 125 keV (this requires a crystal thickness not exceeding 250 nm). Model calculations using a SRIM-98 routine and a special program developed for determining the effect of the plate thickness on the radiation defect production and the implant accumulation [7] showed that the K value significantly increases in the samples with thicknesses comparable with the mean projected range of bombarding ions ($\langle R_p \rangle$). In particular, for 17-keV He^+ ions at a depth equal to an ion range of 150 nm (corresponding to the maximum rate of the point-defect production in Si), the K value for a bulk silicon crystal (i.e., for $t \gg \langle R_p \rangle$) amounts to 70 displacements per He atom, whereas the same ions irradiating a thin plate from the edge yield K = 120 for t = 200 nm and K = 230 for t = 100 nm.

It should be especially noted that this thin-plate technique not only provides a means of varying K by changing the silicon plate thickness. Using TEM, it is possible to study structural changes in the target crystal along the whole projected ion range immediately after irradiation.

The experiments were performed with a mass-separated beam of He^+ ions with an energy of 17 keV and a flux density of 2×10^{14} cm^{-2} s^{-1} obtained from a DECRIS-14 ion source (JINR, Dubna). The calculated temperature in the ion damage region of a thin silicon plate target was below 40°C.

The pattern of characteristic structural changes taking place within the projected range of He^+ ions in a 150-nm-thick silicon crystal plate irradiated to various doses is illustrated in Fig. 1. The formation of pileups of the radiation defects over the whole damaged layer thickness is observed beginning with a fluence of 3×10^{16} cm^{-2} (Fig. 1a). The region of maximum density of the defect pileups occurs at a depth of about 200 nm, which is greater than the peak depth (140 nm) on the calculated damage density profile (Figs. 1e and 1f). As the total fluence grows (up to 5×10^{16} cm^{-2}), a characteristic "through" is observed at a depth of 170 nm in the radiation defect pileup density profile (Fig. 1b). At this very depth, an amorphous layer is formed at a fluence of 10^{17} cm^{-2} (Fig. 1c). When the total fluence increases to 3×10^{17}, the amorphous layer expands to reach the bombarded surface (Figs. 1d and 1e).

Note that the buried amorphous layer is nucleated between the peaks of the calculated radiation damage density profile and the peak of implanted helium concentration (Fig. 1f). This fact indicates that the amorphization of silicon is not determined separately by the accumulation of point defects or implanted helium. Apparently, a determining factor is accumulation of the implant–vacancy (He_nV_m) complexes, provided that

both necessary (K is not less that 90 displacements per He atom) and sufficient (He concentration is not lower than 1 at. %) conditions are fulfilled.

Thus, the results of TEM investigations showed that low-energy helium ions can produce room-temperature amorphization of silicon, provided that the ratio of the point defect production rate to the rate of helium accumulation in silicon is greater than 90 displacements per He atom and the ion fluence exceeds 10^{17} cm^{-2}.

REFERENCES

1. F. F. Morehead and B. L. Crowder, Radiat. Eff. **6** (1/2), 27 (1970).
2. S. Takeda and J. Yamasaki, Phys. Rev. Lett. **83**, 320 (1999).
3. V. F. Reutov, Zh. Tekh. Fiz. **51**, 2403 (1981) [Sov. Phys. Tech. Phys. **26**, 1418 (1981)].
4. V. F. Reutov, G. T. Zhdan, and Sh. Sh. Ibragimov, Vopr. At. Nauki Tekh., Ser.: Fiz. Radiats. Povrezhdeniĭ Radiats. Materialoved., No. 2 (16), 87 (1981).
5. V. Raineri, S. Coffa, E. Szilágyi, *et al.*, Phys. Rev. B **61**, 937 (2000).
6. R. Siegele, G. C. Weatherly, H. K. Haugen, *et al.*, Appl. Phys. Lett. **66**, 1319 (1995).
7. V. F. Reutov and A. S. Sokhatskiĭ, Materialovedenie **10**, 6 (1998); Preprint No. R14-97-199, OIYaI (Joint Inst. for Nuclear Research, Dubna, 1997).

Translated by P. Pozdeev

Technical Physics Letters, Vol. 28, No. 7, 2002, pp. 618–620. Translated from Pis'ma v Zhurnal Tekhnicheskoĭ Fiziki, Vol. 28, No. 14, 2002, pp. 88–94.

Magnetic Flux Penetration into a Superconducting Double Stripline with an Edge Barrier

N. V. Zhelezina and G. M. Maksimova

Nizhni Novgorod State University, Nizhni Novgorod, Russia

e-mail: galina@mail.nnov.ru

Received February 5, 2002

Abstract—An analytical solution to a problem concerning the behavior of a superconducting contour comprising two parallel thin-film strips in a magnetic field of increasing strength. The entrance of vortices into the films, which are free of bulk inhomogeneities, is controlled by an edge barrier (of the Bean–Livingston or geometric type). It is established for the first time that the Meissner state can be realized in two regimes: the classical Meissner state in the interval of magnetic field strengths $0 \le H \le H_s$ (where H_s is field strength corresponding to the entrance of the first vortex) and the state in the interval $H_s \le H \le H_c$ for which vortices formed on the boundaries of the films penetrate into the gap. For $H \ge H_c$, the magnetic flux penetration is accompanied by the appearance of a mixed state in the films. Expressions describing the inductance of the superconducting circuit in the entire range of magnetic fields are also obtained for the first time. © *2002 MAIK "Nauka/Interperiodica".*

The phenomenon of magnetic flux penetration into superconducting samples of simple geometry (plates, cylinders, films, disks) has been extensively studied both theoretically and experimentally (see, e.g., [1–8]). It was demonstrated, in particular, that the entrance of vortices into thick films ($d \gg \lambda$, where d is the film thickness and λ is the London penetration depth) with rectangular cross sections is controlled by a geometric barrier [5]. For thin films ($d \ll \lambda$) with smooth edges, the structure of the mixed state appearing in the superconductor is determined by the Bean–Livingston barrier [6, 7].

Recently, there arose an interest in the study of superconducting systems of more complicated configuration carrying a transport current. For example, Genenko *et al.* [9, 10] considered the problem of vortex penetration into current-carrying thin films, which were surrounded by magnetic screens possessing a high magnetic permeability. It was demonstrated that, for a certain special geometry, the influence of the magnetic surrounding is manifested by an increase in the critical current of the film. Mawatari and Clem [11] established that the critical current of a thin film with $2N$ longitudinal cuts increases by a factor of $(N + 1)^{1/2}$ as compared to that of a simply connected film of the same width.

One of the most convenient experimental configurations is offered by a system of two strips shunted at a large distance, thus forming a closed loop [12]. It was demonstrated (see, e.g., [13]) that circuits comprising two parallel bridges of type II superconductors may feature the Mersero effect, whereby the total critical current exhibits a periodic dependence on the external magnetic field. Recently, Mikitik and Brandt [14] used a two-strip line model for interpretation of the experiments described in [15, 16].

In this letter, we report the exact solution to the problem of the magnetic flux penetration into a superconducting line comprising two planar strips free of bulk inhomogeneities, exposed to an external magnetic field $\mathbf{H} = (0, 0, H)$ oriented perpendicularly to the surface of strips (Fig. 1). The strips, made of a thin film with the thickness d, possess a rectangular cross section with a width w ($d \ll w$). The ends of strips are shortened at the infinity ($x \longrightarrow \pm\infty$). The distance between central lines of the strips is $2a$.

The distribution of current density $i(y)$ and vortex density $n(y)$ in the films is determined by solving the following equation valid for wide strips ($w \gg \lambda_\perp$, $\lambda_\perp = 2\lambda^2/d$) far from the edges:

$$\int_{-w/2}^{w/2} \frac{i(t)dt}{t-y} + \int_{2a-w/2}^{2a+w/2} \frac{i(t)dt}{t-y} = \frac{c}{2}(H - n\Phi_0), \qquad (1)$$

where Φ_0 is the flux quantum and c is the speed of light. Let us assume that the strips are zero-field-cooled to a superconducting state, after which the external field is switched on. As the field strength H increases, the magnetic flux penetrates into the system. This process can be divided into three stages.

1. $0 \le H \le H_s$. In this interval, the magnetic flux does not penetrate into the superconducting circuit and the films occur in the classical Meissner state. The current density distribution can be determined, with an allowance for the symmetry of the function $i(y) = -i(2a - y)$,

by solving Eq. (1) using the method of inversion of the Cauchy-type integral. For definiteness, considerations below refer to the left-hand strip (Fig. 1). Introducing the new variable $u = (a - y)^2$, we obtain from (1)

$$i(u) = \frac{cH}{2\pi}\frac{\alpha^2(1 - f(t)) - u}{\sqrt{(\alpha^2 - u)(u - \beta^2)}}, \quad \beta^2 + 2\beta\delta \le u \le \alpha^2 - 2\alpha\delta, \tag{2}$$

where $\alpha = (a + w/2)$; $\beta = (a - w/2)$; $\delta = \max(\lambda_\perp, d)$, $t = \beta/\alpha$; and $f(t) = E(t)/K(t)$, $K(t)$ and $E(t)$ being the complete elliptic integrals of the first and second kind, respectively (the current density distribution in the right-hand strip differs from (2) only by the sign). For the two films in contact ($t \approx 0$), expression (2) yields

$$i(y) = \frac{cH}{2\pi}\frac{y - w/2}{\sqrt{(y + w/2)(3w/2 - y)}}, \quad -\frac{w}{2} \le y \le \frac{3w}{2}, \tag{3}$$

which corresponds to the current density distribution in the strip of double width $2w$ exposed to the same transverse field. For films spaced by a large distance $a \gg w/2$ ($t \longrightarrow 1$), the current density distribution is symmetric relative to the strip center:

$$i(y) = \frac{cH}{2\pi}\frac{a}{\ln(w/4a)}\frac{1}{\sqrt{(w^2/4 - y^2)}}, \quad -\frac{w}{2} \le y \le \frac{w}{2}. \tag{4}$$

In this case, the total magnetic flux Φ_1 in the gap is zero: $\Phi_1 = \Phi_H + \Phi_k = 0$, where $\Phi_H = 2\beta H$ is the flux of the external magnetic field and Φ_k is the flux due to the Meissner currents (2) inside the loop. Using Eq. (2), we obtain the total current I_1 and inductance L_1 of the system in the state under consideration:

$$L_1 = \frac{\Phi_k}{I_1} = \frac{8tK(t)}{c}, \quad t = \frac{a - w/2}{a + w/2}. \tag{5}$$

Note that, according to Eq. (2), the absolute value of the current density at the outer edges of the strips exceeds that at the inner edges and increases with the magnetic field strength H. At a certain value of $H = H_s$, the current density modulus at the external edge will become equal to the critical value i_s determined by the surface barrier corresponding to the vortex entrance: for the vortex entrance controlled by the geometric barrier ($d > \lambda$), $i_s = 2\varepsilon_0/\Phi_0$, where $\varepsilon_0 = \Phi_0 H_{c1}$ is the vortex energy per unit length; for the Bean–Livingston barrier ($d \ll \lambda$), the critical current coincides with the depairing current density $i_s = c\Phi_0/(6\sqrt{3}\pi^2\xi\lambda_\perp)$, where ξ is the coherence length. Thus, we obtain

$$H_s = \frac{2\pi i_s}{c}\sqrt{\frac{2\delta(1 - t^2)}{\alpha}}\frac{1}{f(t)}. \tag{6}$$

2. $H_s \le H \le H_c$. In this interval of the field strength, the system features a quasistatic penetration of the magnetic flux into the gap between strips. The corresponding current density distribution is as follows:

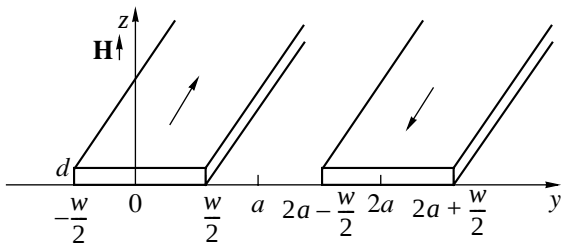

Fig. 1. A schematic diagram of the thin-film strip loop (strips are connected at $x \longrightarrow \pm\infty$) in a perpendicular external magnetic field. Arrows indicate the direction of screening currents.

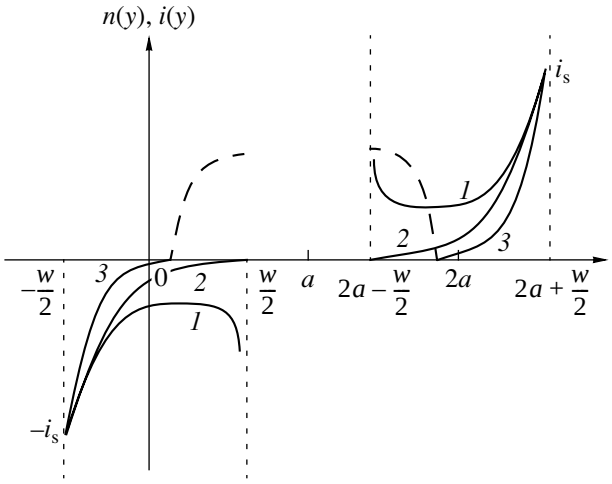

Fig. 2. The current density distribution (solid curves *1–3*) and vortex density (dashed curves) in the double thin-film strip line for various values of the external magnetic field strength: (*1*) $H = H_s$; (*2*) $H = H_c$; (*3*) $H > H_c$.

$$i(u) = \frac{c}{2\pi}\frac{H(\alpha^2 - u) - H_s\alpha^2 f(t)}{\sqrt{(\alpha^2 - u)(u - \beta^2)}}. \tag{7}$$

A mixed state cannot form in this field range because vortices (due to the constant sign of $i(y)$) are not retained in the strips and are carried by the Meissner currents toward the gap, where a magnetic flux is described by the formula

$$\Phi_2 = 2(H - H_s)\alpha E(t). \tag{8}$$

Calculating the total current flowing in the loop, we obtain an expression for the strip line inductance in the given field interval:

$$L_2(H) = \frac{4\pi}{c}\frac{(1 - H_s/H)E(t) - t}{(1 - f(t)H_s/H)K(t') - E(t')}, \tag{9}$$

where $t' = \sqrt{1 - t^2}$.

As the magnetic field strength increases, the current density at the inner edges decreases in absolute value to become zero at $H = H_c$, where

$$H_c = H_s \frac{f(t)}{(1-t^2)}. \quad (10)$$

Beginning with this value, a part of the entering vortices will be retained in the strips, thus forming a mixed state.

3. $H \geq H_c$. In this case, the inner regions of the films ($\beta^2 < u \leq \gamma^2$) are occupied by vortices. The vortex density is

$$n(u) = \frac{H}{\Phi_0}\sqrt{\frac{\gamma^2-u}{\alpha^2-u}}, \quad \beta^2 < u \leq \gamma^2, \quad (11)$$

where $\gamma^2(H)$ determines the boundary of a region occupied by vortices.

The outer regions of the strips ($\gamma^2 \leq u < \alpha^2$) feature Meissner currents with the density distributed as

$$i(u) = -\frac{cH}{2\pi}\sqrt{\frac{u-\gamma^2}{\alpha^2-u}}. \quad (12)$$

Calculating the total current and the corresponding magnetic flux in the gap, we obtain an expression for inductance in the mixed state:

$$L_3(H) = \frac{4\pi}{c}\frac{E(\eta, \gamma/\alpha) - q^2F(\eta, \gamma/\alpha) - t}{\gamma^2/\alpha^2 K(q) - E(q)}, \quad (13)$$

where $q = \sqrt{1-\gamma^2/\alpha^2}$, $\eta = \arcsin\beta/\gamma$, and $F(\varphi, k)$ and $E(\varphi, k)$ are the incomplete elliptic integrals of the first and second kind, respectively. The boundary of a region occupied by vortices, $\gamma^2 = (a-b)^2$, is determined from the condition $i(y = -w/2 + \delta) = i(u = \alpha^2 - 2\alpha\delta) = -i_s$, which yields

$$\gamma^2 = \alpha^2\left(1 - \frac{H_c^2}{H^2}(1-t^2)\right). \quad (14)$$

As the field strength H increases, this boundary moves towards the outer strip edge (reaching this edge as $H \longrightarrow \infty$).

Figure 2 shows the current density distributions and the vortex densities for various values of the magnetic field corresponding to the three cases considered above.

Thus, we have analyzed the behavior of a superconducting double strip line in an external magnetic field of increasing strength. In the case of a quasistationary periodic variation of the field strength H, the system features a hysteresis whereby the magnetic flux Φ inside the loop depends both on the H value and on the system prehistory. The results of a more detailed analysis will be reported in a forthcoming paper. It should be noted that the phenomenon of hysteresis caused by the vortex penetration into a superconducting thin-film structure (based on Nb and YBCO films) was observed in SQUIDs in the interval of field strengths from 0.1 to 10 G [17].

Acknowledgments. The authors are grateful to I.L. Maksimov for his interest in this investigation and helpful remarks and to J.R. Clem and E.H. Brandt for the information on communications [15, 17].

The study was supported by the Russian Foundation for Basic Research (project no. 01-02-16593), the Ministry of Science and Technology (project no. 107-1(00)), and the Ministry of Education of the Russian Federation (project no. E-00-3.4-331).

REFERENCES

1. J. R. Clem and Z. Hao, Phys. Rev. B **48**, 13774 (1993).
2. E. H. Brandt, M. V. Indenbom, and A. Forkl, Europhys. Lett. **22**, 735 (1993).
3. L. M. Fisher, I. F. Voloshin, V. S. Gorbachev, *et al.*, Physica C (Amsterdam) **245**, 231 (1995).
4. P. N. Mikheenko and Yu. E. Kuzovlev, Physica C (Amsterdam) **204**, 229 (1993).
5. E. Zeldov, A. Larkin, V. Geshkenbein, *et al.*, Phys. Rev. Lett. **73**, 1428 (1994).
6. I. L. Maksimov and A. A. Elistratov, Pis'ma Zh. Éksp. Teor. Fiz. **61**, 204 (1995) [JETP Lett. **61**, 208 (1995)].
7. I. L. Maksimov and G. M. Maksimova, Pis'ma Zh. Éksp. Teor. Fiz. **65**, 405 (1997) [JETP Lett. **65**, 423 (1997)].
8. G. M. Maksimova, D. Yu. Vodolazov, and I. L. Maksimov, Physica C (Amsterdam) **356**, 67 (2001).
9. Yu. A. Genenko, A. Usoskin, and H. C. Freyhardt, Phys. Rev. Lett. **83**, 3045 (1999).
10. Yu. A. Genenko, A. Snezhko, and H. C. Freyhardt, Phys. Rev. B **62**, 3453 (2000).
11. Y. Mawatari and J. R. Clem, Phys. Rev. Lett. **86**, 2870 (2001).
12. K. Yokosawa, S. Kuriki, S. Hirano, *et al.*, J. Appl. Phys. **90**, 4049 (2001).
13. A. I. Golovashkin, I. S. Levchenko, A. N. Lykov, *et al.*, Pis'ma Zh. Éksp. Teor. Fiz. **24**, 565 (1976) [JETP Lett. **24**, 521 (1976)].
14. G. P. Mikitik and E. H. Brandt, Phys. Rev. B **64**, 092502 (2001).
15. M. P. Risse, M. G. Aikele, S. G. Doettinger, *et al.*, Phys. Rev. B **55**, 15191 (1997).
16. M. G. Aikele, R. P. Huebener, D. Weischer, *et al.*, Physica C (Amsterdam) **290**, 109 (1997).
17. J. Z. Sun, W. J. Gallagher, and R. H. Koch, Phys. Rev. B **50**, 13664 (1994).

Translated by P. Pozdeev